Hiroshima University Doctoral Thesis

Spin- and Angle-resolved Photoemission Spectroscopy Study of Spin-momentum-layer Locking in Centrosymmetric BiOI

（スピン角度分解光電子分光による中心対称 BiOI におけるスピン・運動量・レイヤーで固定化された電子状態の研究）

2021

Department of Physical Science,

Graduate School of Science,

Hiroshima University

ZHANG KE

Table of Contents

(1) Fermi Velocity Reduction of Dirac Fermions around the Brillouin Zone Center in In_2Se_3–Bilayer Graphene Heterostructures

Zhenyu Wang, Zhanyang Hao, Yayun Yu, Yuan Wang, Shiv Kumar, Xiangnan Xie, Mingyu Tong, Ke Deng, Yu-Jie Hao, Xiao-Ming Ma, Ke Zhang, Cai Liu, Mingxiang Ma, Jiawei Mei, Guang Wang, Eike F Schwier, Kenya Shimada, Fufang Xu, Chang Liu, Wen Huang, Jianfeng Wang, Tian Jiang, Chaoyu Chen

Advanced Materials 33 (17) 2007503 (2021).

(2) Half-Magnetic Topological Insulator with Magnetization-Induced Dirac Gap at a Selected Surface

Ruie Lu, Hongyi Sun, Shiv Kumar, Yuan Wang, Mingqiang Gu, Meng Zeng, Yu-Jie Hao, Jiayu Li, Jifeng Shao, Xiao-Ming Ma, Zhanyang Hao, Ke Zhang, Wumiti Mansuer, Jiawei Mei, Yue Zhao, Cai Liu, Ke Deng, Wen Huang, Bing Shen, Kenya Shimada, Eike F Schwier, Chang Liu, Qihang Liu, Chaoyu Chen

Physical Review X 11(1) 011039 (2021).

(3) Hybridization-induced gapped and gapless states on the surface of magnetic topological insulators

Xiao-Ming Ma, Zhongjia Chen, Eike F Schwier, Yang Zhang, Yu-Jie Hao, Shiv Kumar, Ruie Lu, Jifeng Shao, Yuanjun Jin, Meng Zeng, Xiang-Rui Liu, Zhanyang Hao, Ke Zhang, Wumiti Mansuer, Chunyao Song, Yuan Wang, Boyan Zhao, Cai Liu, Ke Deng, Jiawei Mei, Kenya Shimada, Yue Zhao, Xingjiang Zhou, Bing Shen, Wen Huang, Chang Liu, Hu Xu, Chaoyu Chen

Physical Review B 102(24) 245136 (2020).

(4) Gapless Surface Dirac Cone in Antiferromagnetic Topological Insulator $MnBi_2Te_4$

Yu-Jie Hao, Pengfei Liu, Yue Feng, Xiao-Ming Ma, Eike F Schwier, Masashi Arita, Shiv Kumar, Chaowei Hu, Meng Zeng, Yuan Wang, Zhanyang Hao, Hong-Yi Sun, Ke Zhang, Jiawei Mei, Ni Ni, Liusuo Wu, Kenya Shimada, Chaoyu Chen, Qihang Liu, Chang Liu

Physical Review X 9(4) 041038 (2019).

Main Thesis

HIROSHIMA UNIVERSITY

DOCTORAL THESIS

Spin- and Angle-resolved Photoemission Spectroscopy Study of Spin-momentum-layer Locking in Centrosymmetric BiOI

Author: Ke ZHANG

Supervisor: Prof. Kenya SHIMADA

A thesis submitted in fulfillment of the requirements

for the degree of Doctor of Philosophy

in the

Department of Physical Science

Graduate School of Science

Higashi-Hiroshima

July 08, 2021

Contents

List of Figures

List of Tables

List of Abbreviations

SOC	Spin orbital coupling
HSP	Hidden spin polarization
TRIM	Time-reversal invariant momentum
BZ	Brillouin zoom
PES	Photoelectron spectroscopy
ARPES	Angle resolved photoemission spectroscopy
spin-ARPES	spin and angle resolved photoemission spectroscopy
TB model	Tight-binding model
D-1	Dresselhaus splitting
R-1	Rashba splitting
D-2	Hidden Dresselhaus splitting
R-2	Hidden Rashba splitting
CEC	Constant energy contour
VLEED	Very low energy electron diffraction
BIA	Bulk inversion asymmetry
SIA	Structural inversion asymmetry
UHV	Ultra-high Vacuum

Abstract

The electron spin in nonmagnetic crystal is degenerated under the protection of time-reversal and space inversion symmetries. The spin-orbit coupling (SOC), however, lifts the spin degeneracy if the space inversion symmetry is broken, termed as the Rashba or Dresselhaus spin splitting. Recently novel types of the Rashba spin splitting and/or Dresselhaus spin splitting have been predicted and confirmed in the centrosymmetric crystals, which is fundamentally derived from the asymmetry of the specific atomic site, rather than the asymmetry of the global crystal space group. Given the spin polarization or spin texture exists on a sector (quasi-2D sublattice) as well as its inversion partner sector in the unit cell, it is called the hidden spin polarization (HSP), as there is no net spin polarization for the whole crystal because spin polarization direction on a sector is anti-parallel to that on the inversion partner sector. The HSP on the sector, however, may be reduced via the interaction with its inversion partner, impeding potential applications of this effect.

Due to the compensation of the spin of the opposite sectors, it is not trivial at all to retain highly polarized spin texture of a given local sector. In order to obtain sizable net polarization in each sector, apart from a strong SOC, one should minimize the compensation between the sectors connected to the inversion symmetry point. A trivial strategy is to separate the opposite sectors as far as possible, for example, inserting a thick slab between the opposite sectors. However, even though the two opposite sectors are far away enough, there is still an unavoidable compensation of the opposite sectors, besides the difficulty in the realization of such type materials.

Here, we proof another non-trivial, symmetry-assisted strategy to minimize compensation and achieve a highly spin-polarized spin texture in each local sector protected by nonsymmorphic symmetries in centrosymmetric lattice. Based on the tight-binding model, if two opposing sectors are connected to each other through nonsymmorphic symmetry, the energy bands along the Brillouin zone (BZ) boundary have at least two-fold degeneracy derived from the energy bands on the two adjacent sectors with anti-parallel spin texture. These bands are fourfold degeneracy at the time-reversal invariant momentum (TRIM). The interaction (compensation) between the adjacent sectors disappears along the BZ boundary and hence the HSP with high spin polarization can be realized on two sectors that are closely connected via the centrosymmetry point.

As a promising example, here we examined BiOI single crystal whose space group is P4/nmm in which there exists a centrosymmetric point, glide planes and screw axes, such that the requirements on the symmetry properties are fulfilled and should have the HSP based on the theoretical considerations. In this study, we systematically investigated the electronic states of BiOI by means of spin and angle resolved photoemission spectroscopy (spin-ARPES). We find that the compensation of the spin polarization is substantially suppressed along the Brillouin zone boundary leading to a highly polarized spin state up to about 80% along the M-X direction, while the spin polarization is no more than 30% near the zone center (Γ point) due to the strong compensation by its inversion partners. The observed band structure and spin texture show good agreements with our theoretical calculations, fully confirming the HSP protected by nonsymmorphic symmetry. Our study provides evidence how one can design and realize highly spin-polarized electronic states in nonmagnetic centrosymmetric solids using lattice symmetry, providing the guiding principle to design materials for the future spintronics devices.

Chapter 1 Introduction

The strategy for generating highly spin-polarized electronic states in non-magnetic solids has been explored extensively because it is an important key to realize novel quantum devices [1-6]. It is generally believed that this requires breaking the global space inversion symmetry since a combination of both time-reversal symmetry [$E(\vec{k},\uparrow) = E(-\vec{k},\downarrow)$] and space inversion symmetry [$E(\vec{k},\uparrow) = E(-\vec{k},\uparrow)$] inevitably yields spin degenerated energy levels in solids, which is known as the Kramer's theorem.

A relativistic electron moving in an electric field experiences an effective magnetic field [$\vec{B}_{eff} \propto \nabla V(\vec{r}) \times \vec{p}$] [7,8], where $\nabla V(\vec{r})$ denotes the gradient of the crystal potential and $\vec{p}$ is the crystal momentum. The $\vec{B}_{eff}$ interacts on an electron spin $\vec{s} = \frac{\hbar}{2}\vec{\sigma}$, giving rise to the spin-orbit coupling (SOC) [$H_{SOC} \propto \vec{\sigma} \cdot (\nabla V(\vec{r}) \times \vec{p})$] [9], where σ denotes Pauli matrices. The spin splittings induced by the SOC have been classified as the Dresselhaus splitting (D-1) [10] and Rashba splitting (R-1) [11-14]. Previously it was widely believed that the spin splitting was unlikely in the centrosymmetric crystals. However, the Rashba-type spin splitting has been found experimentally in centrosymmetric crystals recently [15,16]. Zhang and Liu et al. first explained that the observed spin polarization is a local spin polarization on specific atomic sites with point group asymmetries [C_n C_{nv}, D_n S_4, D_{2d}, C_{3h}, D_{3h}, T, T_d, O, $(n = 1,2,3,4,6)$], rather than the spin polarization from the global symmetry of the crystal [17]. While there exist the local spin textures around the specific atomic sites, these spin textures cancel each other if added within the centrosymmetric cell, leading to a nonmagnetic state. It is called, therefore, hidden spin polarization (HSP) [17-19]. The local gradient of the electric potential characterized by the point group is reflected in the SOC term in each sector. If the whole crystal structure has a specific space group symmetry having centrosymmetric point, glide plane, screw axes, the high spin polarization on each sector does not have to cancel each other even though they are closely contacted in the real space.

Based on this theory, these hidden Rashba- and Dresselhaus-type splitting (Denominated R-2 and D-2 respectively [18]) have been experimentally confirmed in the bulk inversion symmetric crystals, such as WSe_2 [20], MoS_2 [21], $BaNiS_2$ [22], $PtSe_2$ [23], and Bi2212 [24]. The prediction and successful confirmations of the "hidden spin polarization" (HSP) in nonmagnetic centrosymmetric crystals have prompted further studies, such as spin-orbit torque

in antiferromagnet (AFM) [25-27], atomic orbital [28], optical activity [29], circular polarization [30], current-induced spin polarization [31,32] in various centrosymmetric systems.

Due to the compensation of the spin of the opposite sectors, however, it is not trivial at all to retain highly polarized spin texture on a given local sector. In order to obtain sizable net polarization in each sector, apart from a strong SOC, one should minimize the compensation between the sectors connected to the inversion symmetry point. A trivial strategy is to separate the opposite sectors as far as possible, for example, inserting a thick slab between the opposite sectors. However, even though the two opposite sectors are far away enough, there is still an unavoidable compensation of the opposite sectors, besides the difficulty in the realization of such type materials [19].

Nonsymmorphic symmetry (such as the glide plane and screw axes) has recently attracted widespread attention, because it has been well established that the nonsymmmorphic crystals should have degenerated bands on the Brillouin zone surface or Brillouin zone boundaries, hosting new types of quasiparticle such as Dirac node [33-36], nodal-chain [37,38] and nodal-surface [39] etc. Nonetheless, its impact on the HSP as well as Bloch states of different sublattices (or sectors) has not been experimentally explored yet.

Here, we explore a nontrivial, symmetry-assisted strategy to minimize the compensation and realize highly spin polarized spin texture in each local sector protected by the centrosymmetric and nonsymmmorphic lattice properties. Based on our tight-binding (TB) model, if the two opposite sectors are connected each other by nonsymmorphic symmetry, the time-reversal invariant momentum (TRIM) holds four-fold degeneracy, and the inter-sector interaction vanishes along the BZ boundary while it is strong around the BZ center (Γ point) [19]. Nearly perfect HSP can exist on two quasi-2D lattice even closely contacted via the centrosymmetric point. This strategy offers a general method to realize the HSP for future applications, especially for all-electron manipulation of novel less-dissipative spintronic devices.

In this study, to reveal the spin texture and energy band dispersions, we use synchrotron radiation-based spin- and angle-resolved photoemission spectroscopy. Synchrotron radiation is the electromagnetic radiation emitted when high-energy electrons or positrons make accelerated motion. The application of synchrotron radiation source provides a new experimental platform and a new way for the development of science and technology. Photoelectron spectroscopy (PES) technology with tunable synchrotron radiation as the light source is the most direct and powerful experimental tool to study the microscopic electronic structure of the advanced materials.

In order to experimentally reveal the HSP protected by the nonsymmorphic symmetries in centrosymmetric systems, we have examined the electronic structure of BiOI by means of spin- and angle-resolved photoemission spectroscopy (spin-ARPES) at Hiroshima synchrotron radiation center (HiSOR). BiOI is a quasi 2D layered material belonging to a space group of P4/nmm. It contains two opposites sectors per unit cell which are contacted by the centrosymmetric point. The degeneracy of the energy bands at the Brillouin zone boundaries are protected by the nonsymmorphic symmetry, namely glide mirror reflection and screw axis operation. BiOI has been extensively studied so far because it is one of the most studied catalyst in the visible light photocatalysis [40-42]. However, its HSP effect has not yet been explicitly argued theoretically, and has never been experimentally confirmed, to the best of our knowledge.

Chapter 2 Spin- and Angle-Resolved Photoelectron Spectroscopy: Basic Principles

2.1 Introduction

Advanced materials, including strong correlation electronic systems, magnetic materials, and spintronic materials, etc., are the frontier topics in the field of modern condensed matter physics. These new materials and new physical phenomena provide infinite possibilities for next scientific breakthroughs. In strongly correlated electronic systems, for example, the interactions between charges, spins, orbits, and lattices, have been found to lead to various novel quantum phenomena [43-51].

Photoelectron spectroscopy (PES) technique is the most direct and powerful experimental tool to study the microscopic electronic structure of these advanced materials. Since the macroscopic properties of any material are dominated by its microscopic electronic movement, to understand, control and utilize the novel physical properties, we must first study their electronic structure. As known, to completely describe the state of an electron, three basic parameters need to be obtained: energy (E_k), momentum ($\hbar\vec{k}$), and spin ($\vec{s}$). Therefore, photoelectron spectroscopy technology plays an indispensable role in the frontier research of condensed matter.

Historically, the phenomenon of photoelectron emission was discovered by H. Hertz in 1887 [52] and consequently the relationship between photon energy and photoelectron kinetic energy was quickly clarified by A. Einstein in 1905 [53]. The use of PES in materials science has been widely recognized until Kai M. Siegbahn published a paper entitled "*Precision Method for Obtaining Absolute Values of Atomic Binding Energies*" in 1957 [54]. After 1975, due to the tunability of photon energy, the use of synchrotron radiation has promoted the development of photoelectron spectrum. In the past three decades, the development of light sources makes it possible to realize photoelectron spectroscopy with high energy resolution even in soft X-ray and hard X-ray regions. Several advanced third-generation synchrotron radiation light sources have been commissioned [55-58], thus, the intensity and resolution of the light sources have been significantly improved. Now, by using a good monochromator, the synchrotron radiation can provide energy for photons with a resolution of less than a few meV below 100 eV.

On the other hand, modern photoelectron spectrometers not only provide very high energy and momentum resolution with a multi-channel detection, but automatic angle scanning technology also facilitates the hemispherical mapping of the topology of Fermi surfaces in momentum space [59,60]. Therefore, ARPES has now become a powerful imaging technique that can provide very direct *k*-space images that contain the dispersion of the energy band and the constant energy contours (CECs). Especially, combined with synchrotron radiation as a tunable photon source, the full *k*-space is accessible by ARPES, and it is the only powerful experimental tool to study three-dimensional electronic structures over the wide energy range of the valence bands.

In addition, spin polarization measurement is widely used to study spin states. Modern, sophisticated ARPES setups are also equipped with spin detectors. For spin analyses, a spin detector (either a VLEED detector or a Mott detector) is connected to the conventional hemispherical ARPES analyzer. These detectors utilize asymmetries in scattering cross sections of electrons with specific targets: electrons with spin-up experience different scattering compared to electrons with spin-down [61].

This chapter will briefly explain the basic principles of (spin) angle-resolved photoelectron spectroscopy techniques. The first part briefly describes the principles of angle-resolved photoelectron spectroscopy, including one-step model, three-step model, sudden approximation, and Green's function of single-particle spectral function; second part introduces the basic principles of spin-ARPES; the third part introduces the experimental components, including light source, electronic energy analyzer, sample rotation system, spin detectors, ultra-high vacuum system and cryogenic system.

2.2 Basic Principles of Angle-Resolved Photoelectron Spectroscopy

2.2.1 General description of angle-resolved photoelectron spectroscopy

The basic principle of photoelectron spectroscopy technology is based on the photoelectric effect [52-54]. When a beam of monochromatic light with energy $h\nu$ higher than the work function irradiates the sample, electrons at different energy levels (such as core levels and valence band) are emitted. And then analyze and count of the energy, angle, and quantity of these emitted photoelectrons, one can deduce the information of the internal electronic structure of the material. According to the different physical quantities measured, PES can be divided into angle-

integrated photoelectron spectroscopy where only energy is measured, and angle-resolved photoelectron spectroscopy (ARPES) where energy and momentum are measured, as well as spin- and angle-resolved photoelectron spectroscopy (spin-ARPES), in which energy, momentum and spin are measured simultaneously.

Figure 2.1 is the schematic drawing of a modern ARPES experiment. When a beam of monochromatic light (hv) illuminates the sample, due to the photoelectric effect, electrons are excited and can escape into the vacuum in all directions. An electron energy detector collects these photoelectrons at different angles in real space, and measures the distribution of the number of these photoelectrons with the kinetic energy (E_k). The magnitude of the photoelectron momentum ($\vec{p}$) can be determined by the following formula:

$$|\vec{p}| = \sqrt{2mE_k} \tag{2.1}$$

where the components of the momentum $\vec{p}$ parallel and perpendicular to the sample surface are determined by the polar angle (θ) and the azimuth angle (φ).

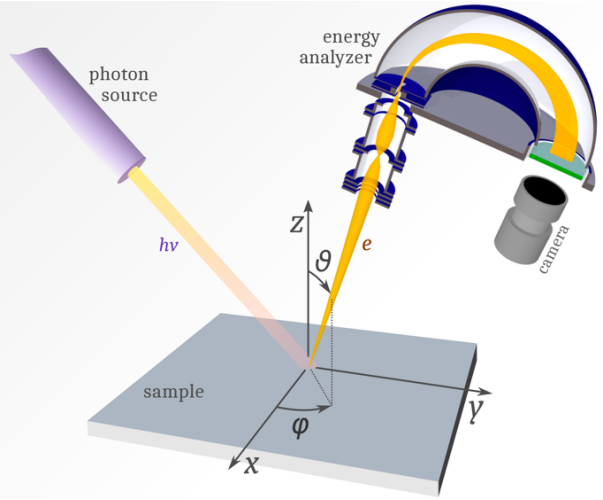

Figure 2.1 Schematic drawing of a modern ARPES experiment. hv is the incident photon energy, e is the emitted photoelectrons, the emission direction is determined by the polar angle (θ) and the azimuth angle (φ). The figure is publicly available on Wiki [62].

In the process of photoelectron emission, the emitted photoelectrons are approximately regarded as free electrons with momentum $\hbar\vec{K} = \hbar(\vec{K}_{\parallel} + \vec{K}_{\perp})$ consisting of parallel and vertical components. The parallel component is conserved (Actually, the parallel component should consist of photoelectrons momentum and photons momentum, considering that the photon

energy used in the ARPES experiment is relatively low, the momentum of the photon itself can be ignored, for example, if the energy of a photon is $h\nu = 100eV$, the momentum of the photon is $k = 2\pi/\lambda = 2\pi\nu/c \approx 0.05\text{Å}^{-1}$) while the vertical component is non-conservation since the vertical translation symmetry of the surface is broken on the sample surface. Therefore, the energy and the parallel component of the momentum of the photoelectron ($h\vec{K}_{\parallel}$), the binding energy (E_B) inside the solid, and the momentum of the crystal ($h\vec{k}_{\parallel}$) can be connected by the following conservation relationships:

$$E_k = h\nu - E_B - \varphi \tag{2.2}$$

$$K_{\parallel} = k_{\parallel} = \begin{bmatrix} k_x \\ k_y \end{bmatrix} = \frac{1}{\hbar}\sqrt{2mE_k} \cdot sin\theta \cdot \begin{bmatrix} cos\varphi \\ sin\varphi \end{bmatrix} \tag{2.3}$$

In the formula, $h\vec{k}_{\parallel}$ is the component of the electron crystal momentum parallel to the surface in the extended Brillouin zone. For larger angles (θ), the actual measured electron momentum can reach the high-order Brillouin zone. By subtracting the reciprocal lattice vector $\vec{G}$, the simple electron crystal momentum in the first Brillouin zone can be obtained.

As for vertical momentum, if we regard the final states in vacuum, i.e. photoelectrons, as free electrons [63], thus, we can rewrite kinetic energy (E_k) as:

$$E_k = \frac{\hbar^2 K^2}{2m} = \frac{\hbar^2 (k_{\parallel}^2 + k_{\perp}^2)}{2m} - V_0 \tag{2.4}$$

and V_0 is the defined inner potential $V_0 = E_0 + \varphi$, shown in Figure 2.2. Putting (2.3) into (2.4), thus, we get the vertical momentum as:

$$k_{\perp} = \frac{1}{\hbar}\sqrt{2m(E_k cos^2\theta + V_0)} \approx 0.512\sqrt{E_k cos^2\theta + V_0} \neq K_{\perp} \tag{2.5}$$

The inner potential V_0 can be obtained by matching the measured energy band with the theoretical calculation. A common and convenient method is to use a series of photons of different energies to measure the photoelectron spectrum of the sample along the normal direction. At this time, the $\vec{k}_{\parallel}$ is equal to zero; thus, by observing the periodic symmetry of these $\vec{k}_z$ ($\vec{k}_{\perp}$) dispersion with the photon energy change, the internal potential V_0 can be obtained easily.

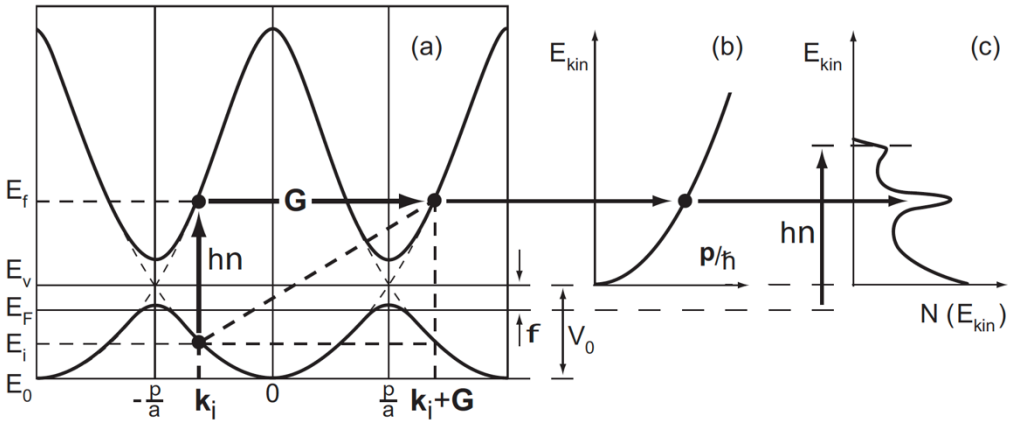

Figure 2.2 Schematic drawing of energy levels and electron transition. (a) an electron absorbs the photon energy (hv) and then vertically transitions from initial state (E_i) to final state (E_f) which is approximatively regarded as free photoelectron in (b). E_0 is the bottom of the valence band, E_f is the Fermi level of the solid, E_v is the vacuum level, $\vec{G}$ is reciprocal lattice vector, φ is the work function of the solid, and V_0 is the so defined inner potential $V_0 = E_0 + \varphi$. (b) The energy dispersion of the free electron approximation of emitted photoelectrons, whose reference energy level is the vacuum level (E_v). (c) Intensity of emitted photoelectrons counted by electron energy analyzer. The peaks of the spectrum and the energy levels in solid are related by the formulas (2.2), (2,3) and (2.5). This figure is referenced from [64].

2.2.2 Quantum view of angle-resolved photoelectron spectroscopy

From a quantum point of view, photoelectron emission is an extremely complex process. Under the interaction of electromagnetic field (incident light), the electrons in the solid excited from the occupied state, and then escape to the vacuum, and finally are captured by the detector. The process is a whole interrelated process. This is the so-called one-step model. This means that a very large Hamiltonian is required to describe the quantum event, including the bulk state, surface state, evanescent state, and surface resonance state, etc., which greatly increases the complexity of quantitative analysis of the photoelectron energy spectrum. Since the one-step model is very complicated, in fact, a simpler three-step model is usually used to approximate the photoelectron emission process. Within the three-step model, photoelectron emission can be divided into three continuous processes: (1). Photoexcitation of an electron inside the solid (creation of a photoelectron represented by $P(E_k, hv)$); (2). Travel of the photoelectron to the

sample surface represented by $T(E_k, h\nu)$; (3). Emission of the photoelectron into the vacuum represented by $E(E_k)$ [65].

Based on the above assumption, the photoemission intensity is proportional to the product of these probabilities corresponding to each step, which should be a function of the photoelectron kinetic energy in vacuum (E_k) and the excitation photon energy ($h\nu$).

$$I(E_k, h\nu) \propto P(E_k, h\nu)T(E_k, h\nu)E(E_k) \tag{2.6}$$

(1) Step one: sudden approximation and single electron spectral function

In the first step, the external field, i.e., the electromagnetic field of light describe by a vector potential ($\vec{A}(\vec{r}, t)$) of a classical electromagnetic plane wave (2.7) is regarded as weak perturbation compared with the internal crystal periodical field.

$$\vec{A}(\vec{r}, t) = \vec{A}_0 e^{i(\vec{q}\cdot\vec{r}-\omega t)} \tag{2.7}$$

Thus, the electric field reads:

$$\vec{E}(\vec{r}, t) = -\frac{\partial}{\partial t}\vec{A}(\vec{r}, t) \tag{2.8}$$

and magnetic field:

$$\vec{B}(\vec{r}, t) = \nabla \times \vec{A}(\vec{r}, t) \tag{2.9}$$

By canonical transformation, the Hamiltonian of electrons in electromagnetic field is:

$$\vec{H} = \frac{1}{2m}(\vec{P} - e\vec{A})^2 + V(\vec{r}) = \frac{P^2}{2m} + V(\vec{r}) - \frac{e}{2m}\vec{P}\cdot\vec{A} - \frac{e}{2m}\vec{A}\cdot\vec{P} + \frac{e^2A^2}{2m} \tag{2.10}$$

Considering the commutation of mechanical momentum and vector potential,

$$\left[\vec{P}, \vec{A}\right] = -i\hbar\nabla\cdot\vec{A} \tag{2.11}$$

If we approximately regard the vector potential $\vec{A}(\vec{r}, t)$ as a constant in the region of ultraviolet and atomic scale, (2.11) is commutative, i.e.

$$\vec{A} \cdot \vec{P} = \vec{P} \cdot \vec{A} \tag{2.12}$$

The last term in (2.10) means the interaction of two photons, since the electromagnetic is regarded as weak perturbation, thus, the quadratic of vector potential is negligible. Therefore, the Hamiltonian further reads:

$$\vec{H} = \frac{P^2}{2m} + V(\vec{r}) - \frac{e}{m}\vec{P} \cdot \vec{A} = \vec{H}_0 - \frac{e}{m} e^{i\vec{q}\cdot\vec{r}} \vec{A}_0 e^{-i\omega t} = \vec{H}_0 + \vec{H}_{int} \tag{2.13}$$

where $\vec{H}_0$ unperturbed system, $\vec{H}_{int}$ operator of time-dependent perturbation. The eigen states and eigen energies in unperturbed system (i.e., electrons in solid without electromagnetic field) is given by Bloch equation. According to the Fermi gold rule, the transition rate from initial state $|i\rangle$ to final state $|f\rangle$ of the unperturbed system due to perturbation $\vec{H}_{int}$ is:

$$w_{if} = \frac{2\pi}{\hbar} |\langle f|H_{int}|i\rangle|^2 \delta\left(E_f - E_i - \hbar\omega\right)$$

$$= \frac{2\pi}{\hbar} \frac{e^2}{m^2} \left|\left\langle f\left|e^{i\vec{q}\cdot\vec{r}} \vec{A}_0 \cdot \vec{P}\right|i\right\rangle\right|^2 \delta\left(E_f - E_i - \hbar\omega\right) \tag{2.14}$$

where the $\langle f|H_{int}|i\rangle = \left\langle f\left|e^{i\vec{q}\cdot\vec{r}} \vec{A}_0 \cdot \vec{P}\right|i\right\rangle$ is called matrix element. The order of the length scale of the plane wave $e^{i\vec{q}\cdot\vec{r}}$ (electromagnetic field of light) is $\vec{q} = 2\pi/\lambda$, which means that in VUV radiation it is very large compared to atomic dimensions, e.g., if the $h\nu = 21.2eV$, the wave length is $\lambda = 584$Å, i.e., the $\vec{q} = 0.0107\text{Å}^{-1}$. Therefore, expand the plane wave, the plane wave is approximately equal to 1 ($e^{i\vec{q}\cdot\vec{r}} = 1 + i\vec{q} \cdot \vec{r} + \cdots \approx 1$). Thus, we obtain a simplified matrix element in the region of ultraviolet even $h\nu < 100eV$. So, the simplified transition rate is:

$$w_{if} = \frac{2\pi}{\hbar} \frac{e^2}{m^2} \left|\left\langle f\left|\vec{A}_0 \cdot \vec{P}\right|i\right\rangle\right|^2 \delta\left(E_f - E_i - \hbar\omega\right) \tag{2.15}$$

In terms of the transition rate, the next issue is how to describe the initial state $|i\rangle$ and final state $|f\rangle$. In the process of photoelectric excitation, the electron system, and the photoelectron itself will relax, which means that photoexcitation produces a final state that is lacking one electron with respect to the initial state. In solids, the relaxation mainly consists of three nonnegligible contributions. One results from the relaxation of the orbitals, spin, and electrons

on the same atom (intra-atomic relaxation, including electron-orbital, electron-spin, and electron-electron interactions). Another one is due to a charge flow from the crystal onto the photoexcited atom that carries the positive holes (extra-atomic relaxation, i.e., the electron-charge interaction). The third one is the relaxation of crystal lattice (i.e., the electron-lattice interaction). These interactions are schematically shown in Figure 2.3. Therefore, PES always measures final-state energies, which can be related to initial-state energies only after some theoretical considerations [63]. Here we ignored the impurity and lattice defect scattering in solids. If the concentration of the impurities and defects is low enough as in the present ARPES works, they only contribute to the constant linewidth broadening.

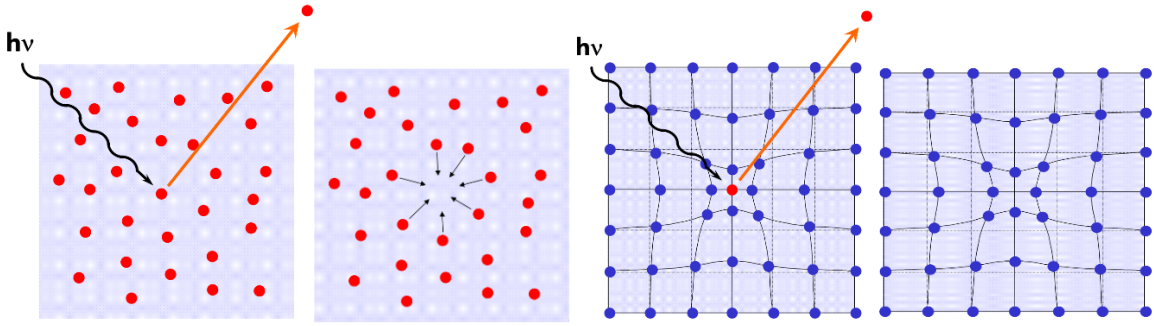

Figure 2.3 Excitations and relaxations during photoexcitation process. An electron after absorbing the energy of photons and emitted from the initial state will left a positive hole in the remaining system, which will result the remaining system relax to new balance state (excitation state). This relaxation process including electron-electron, electron-orbital, electron-spin, electron-charge, and electron-lattice interactions. The red dots represent electrons and blue dots represents crystal lattice. The figures are open accessed from [66].

Due to the many body interactions in solids, the electronic states with a photohole will relax in order to minimize the energy, which is reflected to the signals in the PE spectrum, such as linewidth broadening as well as energy shifts from the ground state of the system. The PE spectrum has finite linewidth, and may have the "main" line (representing the ground state) associated with several "satellite" lines representing the excited states.

To simplify this phenomenon, if high-energy photoelectrons are excited, it is reasonable to consider that the photoelectron is suddenly taken away, and the time taken is much shorter than the system relaxation time, which is called the “sudden approximation” [67]. However, if the photoelectron energy is low, when the time it takes to escape from the surface is comparable to the relaxation time of the system, this is the other extreme, also called “adiabatic approximation”,

at which time the wave function cannot be simply decomposed [68]. When the energy of the photoelectron from the valence band is low, to what extent the "sudden approximation" starts to fail has not been clearly clarified. However, studies of core energy levels show that it depends not only on the types of atom but also on the chemical environment in which it is located [69-74]. The study of valence band photoelectron spectroscopy of high-temperature superconductors found that when the photon energy is 20eV, the "sudden approximation" is also valid [75]. More recent studies suggest that the "sudden approximation" is valid even when the energy is as low as 6.05eV [76,77].

The "sudden approximation" is the key to interpreting the ARPES data. It directly connects the ARPES spectrum with the single-particle spectrum function $A(\vec{k},\omega)$ containing all the electronic information in the solid. By the sudden approximation, the final states $|f\rangle$ can be simply decomposed as:

$$|f\rangle = \mathcal{A}|N-1,m;\ k,f\rangle \text{ or } \Psi_{f,m}^{N} = \mathcal{A}\psi_{f,m}^{N-1}\psi_{f}^{k} \tag{2.16a}$$

where $\mathcal{A}$ is antisymmetry operator (completely anti-symmetry N electron wave functions, thus satisfying the Pauli exclusion principle). $|k,f\rangle$ or ψ_f^k is state or wave function of photoelectrons whose momentum is $\hbar k$. $|N-1,m\rangle$ or $\psi_{f,m}^{N-1}$ is the final state or wave function of the remaining $N-1$ system, which can be regarded as a excitation state whose eigen state is $|N-1,m\rangle$ and eigen value is E_m^{N-1}, where m is the index of the possible excitation states of the remaining system.

As for the initial state, for simplify, we assume it is a Slater determinant (like Hartree-Fock form), thus it can be decomposed in the form of a single-electron orbital function $|k,i\rangle$ and $(N-1)$ particles. Therefore, the initial state reads:

$$|i\rangle = \mathcal{A}|N-1,i;\ k,i\rangle \text{ or } \Psi_{i}^{N} = \mathcal{A}\psi_{i}^{N-1}\psi_{i}^{k} \tag{2.16b}$$

And the eigen value corresponding to the initial state denoted as E_i^N. Therefore, the matrix element in (2.14) and (2.15) of the transition rate is:

$$\langle f|H_{int}|i\rangle = \left\langle f\middle|e^{i\vec{q}\cdot\vec{r}}\vec{A}_0\cdot\vec{P}\middle|i\right\rangle = \left\langle\psi_f^k\middle|\vec{A}_0\cdot\vec{P}\middle|\psi_i^k\right\rangle\left\langle\psi_{f,m}^{N-1}\middle|\psi_i^{N-1}\right\rangle \tag{2.17}$$

here $\left\langle\psi_f^k\middle|\vec{A}_0\cdot\vec{P}\middle|\psi_i^k\right\rangle \equiv M_{fi}$ is the single particle matrix element, and $\left\langle\psi_{f,m}^{N-1}\middle|\psi_i^{N-1}\right\rangle \equiv c_{mi}$ is the $(N-1)$ system overlap integral. Supposing the remaining $(N-1)$ system has m excited states,

thus, the total spectrum intensity ($I(E_k, \vec{k})$) is proportional to the photoexcitation process (Step one):

$$I(E_k, \vec{k}) \propto P(E_k, \vec{k}) \propto \sum_m |M_{fi}|^2 |c_{mi}|^2 \delta(E_k + E_m^{N-1} - E_i^N - h\nu) \tag{2.18}$$

Here $|c_{mi}|^2$ is the probability of $(N-1)$ electrons locating at an excited state m after removing one electron from initial states. For a simplest example, assuming only a specific excited state $m = m_0$ is created, and the excitation state equal to the initial state after removing one electron ($\psi_{m_0}^{N-1} = \psi_i^{N-1}$), where we neglected the relaxation energies. (i.e., we adopted the Koopmans' approximation [78] which states that the binding energy equals the negative energy of the orbital from which the photoelectron is emitted.). Consequently, the probably $|c_{mi}|^2 = 1$, and since other excitation states are assumed not exist, therefore, the ARPES is the δ function [79].

As a matter of fact, all the solids are many-body system with different extend exchange-correlation interaction. A remove of one electron will lead to a non-negligible change of potential for the remaining system, thus, many excited states ($|N-1, m\rangle$ or $\psi_{f,m}^{N-1}$) of the $(N-1)$ system will result in the overlap integral c_{mi} not equal to zero, i.e. the probably $\sum_m |c_{mi}|^2 \neq 0$, this is to say the ARPES spectrum is not like a sharp delta function for independent electrons but broadened "peaks" presenting a "main peak" and some "satellite peaks", referring Figure 2.4 and related refences for more details.

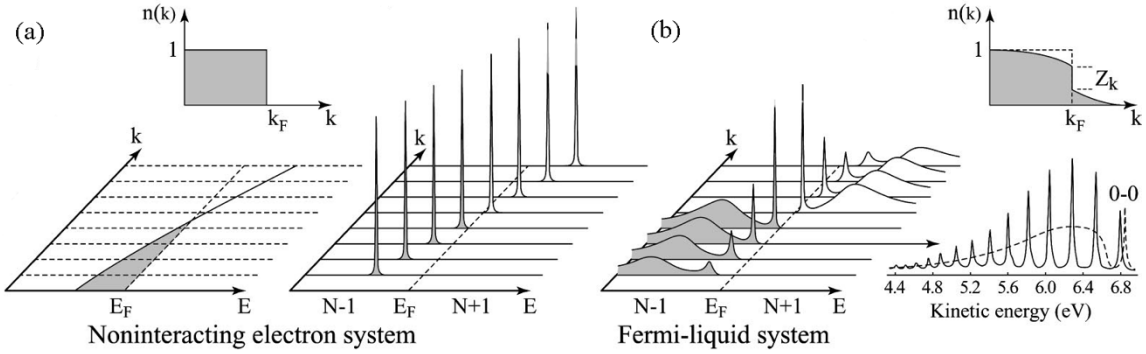

Figure 2.4 ARPES spectrum for noninteraction system and strongly correlated system. (a) momentum-resolved one-electron removal and addition spectra for a noninteracting electron system with a single energy band dispersing across E_F; (b) the same spectra for an interacting Fermi-liquid system (Sawatzky,

1989 [79]; Meinders, 1994 [80]). For both noninteracting and interacting systems the corresponding ground state (50 K) momentum distribution function $n(k)$ is also shown. (b) Lower right, photoelectron spectrum of gaseous hydrogen and the ARPES spectrum of solid hydrogen developed from the gaseous one. Figure accessed form ref. [81].

It is almost impossible to directly calculate the overlapping integrals in the remaining $(N-1)$ system. So, when discussing the photoelectron emission process of solids, especially when many overlapping integrals in the correlation system are not zero ($|c_{mi}|^2 \neq 0$), the most powerful and commonly used one is based on Green's function [82-86]. The propagation of a single electron in a many-body system is described by a time series single electron Green's function $G(t-t')$. Its physical meaning is: the probability amplitude of adding an electron to a Bloch state system with momentum k at the initial moment (t), and after the time $|t-t'|$, the system is still in the same state [80,82-84]. This Green's function $G(t-t')$ can be written in the form of (2.19) under the energy and momentum representation, where the $G^+(\vec{k},\omega)$ and $G^-(\vec{k},\omega)$ represent the addition and removal of single electron Green's function, respectively.

$$G(\vec{k},\omega) \equiv G^+(\vec{k},\omega) + G^-(\vec{k},\omega) \tag{2.19}$$

When the temperature is 0 K, the single electron Green's functions are [85,86]:

$$G^{\pm}(\vec{k},\omega) = \sum_m \frac{\left|\langle \psi_m^{N\pm1}|c_k^{\pm}|\psi_i^N\rangle\right|^2}{\omega - E_m^{N\pm1} + E_i^N \pm i\eta} \tag{2.20}$$

where operator $c_k^+ = c_{k\sigma}^+$ $(c_k^- = c_{k\sigma})$ represents the creation (annihilation) of an electron with energy $\hbar\omega$, momentum $\hbar k$, and spin σ from the N particles system whose initial state is denoted as ψ_i^N. The summation needs to be performed for all the possible excited states (indexed as m) of the $(N \pm 1)$ particles. η is a positive infinitesimal quantity.

From Dirac identify (2.21), where x represents a real quantity, η represents positive infinitesimal quantity, and P denotes the Cauchy principal value integral (i.e., any integration involving the product of $(1/x)$ by a function of x must be intended in principal part), we can rewrite the delta function $\delta(x)$ as (2.22).

$$\lim_{\eta\to 0^+}\frac{1}{x+i\eta}=P\left(\frac{1}{x}\right)-i\pi\delta(x) \tag{2.21}$$

$$\delta(x)=\lim_{\eta\to 0^+}\frac{i}{\pi}\frac{1}{x+i\eta}-\frac{i}{\pi}\frac{1}{x}=\lim_{\eta\to 0^+}-\frac{1}{\pi}\frac{\eta}{x^2+\eta^2} \tag{2.22}$$

By using the Dirac identity (exactly its transformation form (2.22)) we can obtain another new function $A(k,\omega)$ (which we will later term it as single particle spectral function) related to the single electron Green's function $G(\vec{k},\omega)$.

$$A(\vec{k},\omega)\equiv A^{+}(\vec{k},\omega)+A^{-}(\vec{k},\omega) \tag{2.23}$$

$$A(\vec{k},\omega)=-\frac{1}{\pi}ImG(\vec{k},\omega)=-\frac{1}{\pi}Im\left\{G^{+}(\vec{k},\omega)+\left[G^{-}(\vec{k},\omega)\right]^{*}\right\} \tag{2.24}$$

$$A^{\pm}(\vec{k},\omega)=\sum_{m}\left|\langle\psi_m^{N\pm1}|c_k^{\pm}|\psi_i^{N}\rangle\right|^2\delta(\omega-E_m^{N\pm1}+E_i^{N}) \tag{2.25}$$

where $G(\vec{k},\omega)=G^{+}(\vec{k},\omega)+\left[G^{-}(\vec{k},\omega)\right]^{*}$ is defined as retarded Green's function, and $A^{+}(k,\omega)$ and $A^{-}(k,\omega)$ are defined as addition and removal single electron spectral function, because by substituting the overlapping integral in formula (2.18) (please note the $\psi_i^{N-1}=c_k\psi_i^{N}$), it is straightforward that the total spectrum intensity ($I(E_k,k)$) is proportional to the single particle spectral function:

$$I(E_k,\vec{k})\propto P(E_k,\vec{k})\propto\sum_{f,i}\left|M_{fi}\right|^2A^{-}(\vec{k},\omega) \tag{2.26}$$

When the temperature is not equal to zero, since the electron is spin ½ particle (fermion), thus we just need to adopt the Fermi-Dirac distribution function to correct the intensity. Finally, the total spectrum intensity ($I(E_k,k)$) is proportional to the sum of the square of the matrix elements and the single electron spectral function and Fermi-Dirac function, i.e.,

$$I(E_k,\vec{k})\propto P(E_k,\vec{k})\propto I_0A(\vec{k},\omega)f(\omega) \tag{2.27}$$

where $I_0 \propto \sum_{f,i}\left|M_{fi}\right|^2$, $f(\omega) = 1/(e^{\omega/k_B T} + 1)$. Photoelectron spectroscopy can only measure the occupied state of electrons, and the PES spectrum can directly measure the spectral function, which connects the single particle Green's function.

(2) A Short discussion on matrix element effect and self-energy analysis

It can be seen from Equation (2.27) that the photoelectron spectrum is not only directly modulated by the spectrum function $A(\vec{k}, \omega)$, and its "main peaks" are also controlled by the intensity of $I_0 \propto \sum_{f,i}\left|M_{fi}\right|^2$. That is to say, the intensity of the photoelectron spectrum strongly depends on the electron momentum ($\hbar\vec{k}$) in the solid and the energy ($h\nu$) and polarization of the incident photon $\vec{A}(\vec{r}, t)$, even completely controls the intensity of the spectrum. This is the so-called (single electron) matrix element effect.

Using the quantum mechanical identity: $\langle f|\vec{P}|i\rangle = i\frac{m(E_f - E_i)}{\hbar}\langle f|\vec{r}|i\rangle$, let us consider the matrix element $M_{fi} = \langle\psi_f^k|\vec{A}\cdot\vec{P}|\psi_i^k\rangle$. The matrix element is then can be written as:

$$M_{fi} = \langle\psi_f^k|\vec{A}\cdot\vec{P}|\psi_i^k\rangle \propto \langle\psi_f^k|\vec{\varepsilon}\cdot\vec{r}|\psi_i^k\rangle \tag{2.28}$$

where $\vec{\varepsilon}$ is a unit vector along the polarization direction of the vector potential $\vec{A}(\vec{r}, t)$, i.e., $\vec{\varepsilon} = -\frac{\partial\vec{E}}{\partial t}/|\frac{\partial\vec{E}}{\partial t}|$. $\vec{r}$ is a Cartesian position vector. Thus the $\vec{\varepsilon}\cdot\vec{r}$ is the electrical dipole operator. The electrical dipole vector is decided by light electric field $\vec{E}_p(\varepsilon_x, 0, \varepsilon_z)$ for p-polarized light $p$aralleling to the mirror plane (in the same horizontal plane as the mirror plane) and by $\vec{E}_s = (0, \varepsilon_y, 0)$ for s-polarized light $s$enkrecht (vertical) to the mirror plane as shown in Figure 2.5. It is straightforward that to have nonvanishing photoemission intensity, the whole integrand in the overlap integral must be an even function under reflection with respect to the mirror plane (i.e., $M_{fi} \neq 0$) [81,87]. Since at the detector the photoelectron is described by an even-parity plane-wave state $e^{i\vec{k}\cdot\vec{r}}$ [88]. In turn, this implies that $\vec{\varepsilon}\cdot\vec{r}|\psi_i^k\rangle$ or $\vec{A}\cdot\vec{P}|\psi_i^k\rangle$ must be even, restricting that the initial state and dipole operator must present the same symmetry with respect to the mirror plane, as summarized as follow:

$$\begin{cases} \vec{A}\cdot\vec{P}: even \rightarrow |\psi_i^k\rangle: even \iff \langle\psi_f^k|\vec{\varepsilon}\cdot\vec{r}|\psi_i^k\rangle: \langle +|+|+\rangle \\ \vec{A}\cdot\vec{P}: odd \rightarrow |\psi_i^k\rangle: odd \iff \langle\psi_f^k|\vec{\varepsilon}\cdot\vec{r}|\psi_i^k\rangle: \langle +|-|-\rangle \end{cases} \tag{2.29}$$

where $+(-)$ stands for the even (odd) function with respect to the mirror plane. The symmetry of the dipole operator $\vec{A} \cdot \vec{P}$, obviously, depends on the polarization direction of the vector potential $\vec{A}$. Since the p-polarized light (horizontal polarization) has even symmetry with respect to mirror plane ($x - z$ plane), while, the s-polarized light, which has odd symmetry with respect to mirror plane, therefore, if the vector potential $\vec{A}$ is parallel (perpendicular) to the mirror plane, then the $\vec{A} \cdot \vec{P}$ must be even (odd) symmetry. Consequently, the detectable initial state is limited to even (odd) symmetry with respect to mirror plane, indicating that one can selectively observe the even or odd initial electronic states by changing the polarization geometry [89].

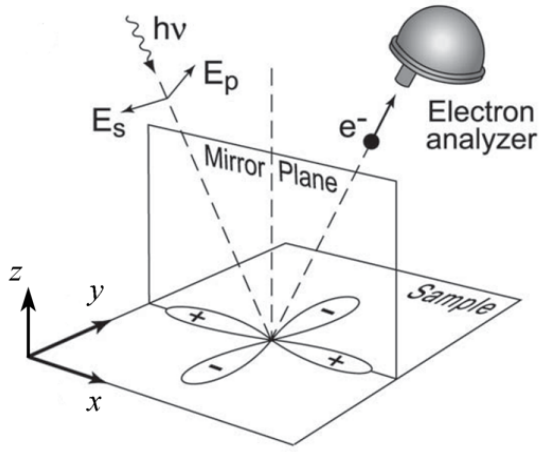

Figure 2.5 Schematic representation of the matrix element effect in the photoemission process: A mirror plane ($x - z$ plane) perpendicular to the sample surface ($x - y$ plane). The electron analyzer and incident light are in the mirror plane (if they are out of the mirror plane, the situation become complicated because of the lack of an overall well-defined even/odd symmetry with respect to the mirror plane, for example, the orbital $d_{x^2-y^2}$ is even symmetry to the mirror plane.). The $\vec{E}_p$ ($\vec{E}_s$) represents p (s) -polarized light paralleling (vertical) to the mirror plane. Figure accessed from ref. [81].

As illustrated above, the spectral function is directly related to the Green's function, while the corrections to the Green's function due to the electron-electron and the like correlations can be conveniently expressed in terms of the electron *proper self-energy* function: $\Sigma(\vec{k}, \omega) = \Sigma'(\vec{k}, \omega) + i\Sigma''(\vec{k}, \omega)$. The self-energy function descripts quasiparticles with bare-band energy (ε_k) and momentum ($\vec{k}$) propagating in a many-body system. Its real (Σ') and imaginary (Σ'')

parts contain all the information on the energy renormalization and finite lifetime, respectively. The Green's and spectral functions expressed in terms of the self-energy are then given by [81]:

$$G(\vec{k},\omega) = \frac{1}{\omega - \varepsilon_k - \Sigma(\vec{k},\omega)} \tag{2.30}$$

$$A(\vec{k},\omega) = -\frac{1}{\pi} ImG(\vec{k},\omega) = -\frac{1}{\pi} \frac{\Sigma''(\vec{k},\omega)}{\left[\omega - \varepsilon_k - \Sigma'(\vec{k},\omega)\right]^2 + \left[\Sigma''(\vec{k},\omega)\right]^2} \tag{2.31}$$

This many-body correlations corrected Green's function (2.30) (also called the Dyson equation [90,91]) and spectral function (2.31), of course, still fulfil the formula (2.27), because here we just modified the form of the Green's function, but it still satisfies the Dirac identity (2.21) and (2.22). Since the Green's function $G(t,t')$ is a linear response function of external perturbation, the real part and imaginary part of its Fourier transform form $G(\vec{k},\omega)$ must satisfy the causal relationship, which are connected by the Kramers-Kronig transformation ($K-K$ transformation) [92,93]. This means that if we have measured the spectrum function $A(\vec{k},\omega)$ by the PES spectrum or the inverse PES spectrum, then the real part and imaginary part of the self-energy function can be calculated by (2.31) and $K-K$ transformation, consequently the complete self-energy function $\Sigma(\vec{k},\omega)$ can be obtained (i.e., $Im\Sigma(k,\omega) = ImG(k,\omega)/[ReG(k,\omega)^2 + ImG(k,\omega)^2]$ and $Re\Sigma(k,\omega) = \omega - \varepsilon_k^0 - ReG(k,\omega)/[ReG(k,\omega)^2 + ImG(k,\omega)^2]$. In fact, the real and imaginary parts of the self-energy are usually obtained through the ARPES spectrum.

In principle, the self-energy can be estimated accurately from energy distribution curves (EDCs) and/or momentum distribution curves (MDCs) of ARPES spectra. If the self-energy is independent of $\vec{k}$ (i.e., the matrix elements are a slowly varying function of $\vec{k}$), then the corresponding MDCs are simple Lorentzians centered at $\vec{k} = \vec{k}_F + [\omega - \Sigma'(\omega)]/\vec{v}_F^0$ with full width at half maximum (FWHM) given by $2\Sigma''(\omega)/\vec{v}_F^0$, where $\vec{v}_F^0$ is the bare Fermi velocity normal to the Fermi surface [81]. However, it must be noted that, although the results of MDC and EDC analyses should coincide, differences in both dispersions and peak widths can be observed at high energies, due to the ω dependence of $\Sigma(\vec{k},\omega)$ or near the band maxima and minima [81]. Please note, so far, we do not consider any extrinsic background and the finite

energy and momentum resolution, which should lead to different extent broadening of the ARPES spectra.

The self-energy $\Sigma(\vec{k}, \omega)$ is a powerful tool to analyze many-body correlations in solids. In the self-energy analysis, all the electron interactions besides the electro-electron interactions are considered, hiding in the spectral function within respective energy scales (kinks in the MDCs or EDCs). Generally, the electron-electron interactions, electron-phonon interactions, and electron-impurity interactions causing the electron scattering are typical in the photo-excitation process (step one), whose energy scales are of the order of several eV, 100 meV and a few tens meV, respectively [94]. Specially, the electron-impurity interactions (impurity scattering) are invariant to energy and momentum which just results in a finite broadening of the quasiparticle peak. In addition, the self-energy analysis of electron-magnon interactions in magnetic materials have been reported through ARPES spectra [95].

(3) Step two: inelastic scattering and mean free path

The second step refers to the process in which the excited photoelectrons move to the surface. This process includes elastic scattering and inelastic scattering of photoelectrons. The inelastically scattered secondary electrons will form a continuous background other than discrete "satellite peaks" on the ARPES spectrum, because these electrons will lose the intrinsic energy and momentum information when continuously inelastically scattered with other particles. Although it is not easy to pick some low intensity peaks from the background, there are still some powerful systematic approaches to realize background correction, such as linear, horizontal, Shirley's and Tougaard's backgrounds [96-98].

As for the elastic scattering, it conserves the "intrinsic" energy information (actually, it is the final states of the exited photoelectrons, while the momentum information mainly comes from the non-scattered photoelectrons). The probability of the photoelectron moving to the surface without serious inelastic scattering is represented by the term of $T(E_k, h\omega)$ being expressed by using the absorption coefficient $\alpha(h\nu)$ for the incident photon and the photoelectron inelastic mean free path $\lambda(E_k)$ approximatively [65].

$$T(E_k, h\omega) = \frac{\alpha(h\nu)\lambda(E_k)}{1 + \alpha(h\nu)\lambda(E_k)} \cong \alpha(h\nu)\lambda(E_k) \tag{2.32}$$

$1/\alpha(h\nu)$ is of the order of 100~1000Å or more for $h\nu$ in the range of 6~10,000 eV, which is much longer than $\lambda(E_k) < 100$Å for most elemental solids as shown in Figure 2.6. In the limit $\alpha(h\nu)\lambda(E_k) \ll 1$ ($\lambda \approx 10-20$Å), the mean free path of the photoelectrons λ is much smaller than the penetration depth of the light $1/\alpha$, one obtains $T(E_k, h\omega) \cong \alpha(h\nu)\lambda(E_k)$.

In principle, the mean free path $\lambda(E_k)$ is a characteristic property of each specific material. But the mean free path, as a function of energy E_k, is a roughly "universal curve" for all materials. Because for the energies of interest in solids, the electrons can be approximately described as free electron gas, in this case, the inverse of the mean free path λ^{-1} is then described by the mean electron-electron distance r_s in solids which is roughly equal for all materials, and one obtains [63,99]:

$$\lambda^{-1} \cong \sqrt{3}\frac{a_0 E_h}{E_k} r_s^{3/2} ln\left[\left(\frac{4}{9\pi}\right)^{2/3}\frac{E_k}{E_h} r_s^2\right] \tag{2.33}$$

where a_0 is Bohr radius, E_h =13.6eV, and the electron-electron mean path r_s is in units of the Bohr radius. Therefore, as expected, almost all materials experimentally show a similar energy dependence of the mean free path $\lambda(E_k)$.

The mean free path curve takes a minimum value of ~3-6Å at the energy E_k range of ~10-100eV in many cases (Figure 2.6), which roughly corresponding to lattice constants of most solids. Thus, within this energy range the photoelectron spectroscopy manly reflect the surface electronic states of solids. If we want to obtain the bulk electronic states is to use higher $h\nu$ than 500eV or more. Therefore, the ARPES is a highly surface sensitive probe technique.

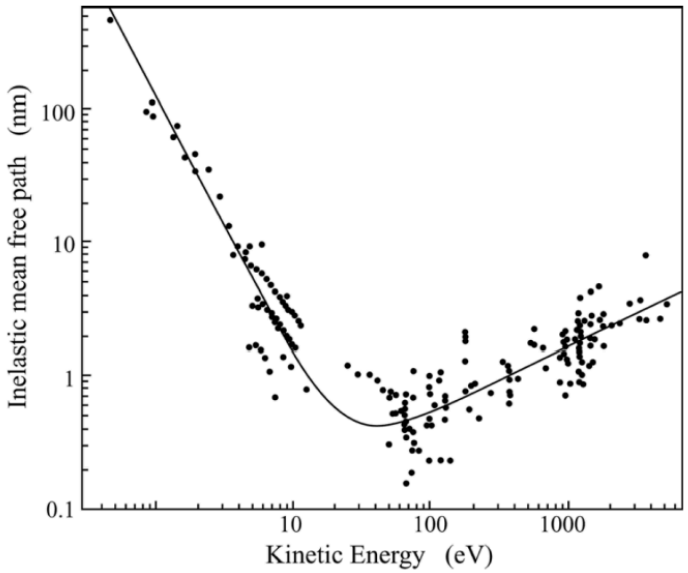

Figure 2.6 The dependence of the mean free path λ on the kinetic energy (black dots). Its slope can be simulated by a *universal curve* shown as a solid line. Figure originated from M. P. Seah and W. A. Dench, 1979. ref. [100].

(4) Step three: escape cone and free electron approximation

Step three represents the process of escape of the photoexcited electrons into vacuum. The escaping electrons are those for which the component of the kinetic energy normal to the surface is sufficient to overcome the surface potential barrier, while the other electrons that are insufficient to overcome the barrier are reflected to the bulk. The escaped electrons must satisfy the energy condition:

$$\left(\frac{\hbar^2}{2m}\right) K_\perp^2 \geq E_v - E_0 \equiv V_0 \tag{2.34}$$

Here $E_0 < 0$ is the energy of the bottom of the valence band and E_v is the vacuum level energy. This potential depth is defined as inner potential V_0. $\vec{K}_\perp$ is the component of the wave vector of the excited electron $\vec{K}$ normal to the surface. The transmission of the electron through the surface leaves the parallel component of the wave vector conserved such that $\vec{p}_\parallel/\hbar = \vec{K}_\parallel = \vec{k}_\parallel + \vec{G}_\parallel$, which can be described by the Snell's law:

$$k_{f_{\parallel}} = sin\theta \sqrt{\frac{2m}{\hbar^2} E_k} = sin\theta' \sqrt{\frac{2m}{\hbar^2} (E_f - E_0)} \tag{2.35}$$

where θ is the angle of refraction, and θ' is the angle of incidence. From this statement, it straightforward that there is a maximum angle of incidence corresponding to the maximum refraction angle $\theta = \pi/2$, i.e.,

$$sin\theta'_{max} = \sqrt{E_k/E_f - E_0} \tag{2.36}$$

The angular region $\theta' \leq \theta'_{max} < \pi/2$ is called the escape cone, responding to the maximum internal parallel wave vector that can be detected.

The state of the escaped electrons in not exact free electron like (described by plane wave) but Bloch wave like $\psi_f(\vec{k})$ containing plane wave contributions with a number of reciprocal lattice vectors G [63]:

$$\psi_f(\vec{k}) = \sum_{\vec{G}} u_f(\vec{k}, \vec{G}) e^{i(\vec{k}+\vec{G})\cdot\vec{r}} \tag{2.37}$$

The total escaping probability of the photoexcited electrons escaping into vacuum is proportional to the square of the Bloch wave [63]:

$$E(E_f, \vec{k}_{\parallel}) \propto \left|t\left(E_f, \vec{K}_{\parallel}\right)\right|^2 \left|\psi_f(\vec{k})\right|^2 \tag{2.38}$$

where the $t\left(E_f, K_{\parallel}\right)$ is the transmission factor. According to the energy condition (2.34), the transmission factor can be expressed as:

$$\left|t\left(E_f, \vec{K}_{\parallel}\right)\right|^2 = \begin{cases} 1 & if\ E_f(\vec{k}) - E_v > \hbar^2\left(\vec{k}_{\parallel} + \vec{G}_{\parallel}\right)^2/2m \\ 0 & if\ E_f(\vec{k}) - E_v \leq \hbar^2\left(\vec{k}_{\parallel} + \vec{G}_{\parallel}\right)^2/2m \end{cases} \tag{2.39}$$

This is of course a rough approximation, because it almost impossible to evaluate the exact $\vec{k}_{\perp}$ component. Therefore, someone starting from the inner potential, write the escaping probability as [65]:

$$E(E_k) \propto \frac{1}{2}\left(1 - \sqrt{\frac{V_0}{E_k + V_0}}\right) \tag{2.40}$$

This function depends gently on E_k, and can be regarded as a constant when the recorded kinetic energy range is narrow enough compared with E_k also true in step two. Therefore, it is hereafter assumed that the E_k dependence of the terms of step two $T(E_k, \hbar\omega)$ and step three $E(E_k)$ is negligible within the discussed kinetic energy range of one spectrum.

(5) A Short discussion on three step model

The three-step model is simple, effective, and practical approximation, which has been proved by many experiments, especially for understanding and using photoelectron spectroscopy to determine the electronic energy band structure of a solid [81,101]. Although the three-step model has achieved great success, it still has many shortcomings. The three-step model is based on the independent electronic model, so it does not completely consider the many-body correlations effect, which cannot be ignored in materials with strong correlation systems such as high-temperature superconductors. The three-step model neither contains the surface photoelectric effect, nor does it contain any surface characteristic effects. For example, the surface state can appear on an ideal cut-off surface, or it can appear on a relaxed or reconstructed surface [102].

The fundamental problem of the three-step model is the conceptual difficulty caused by the very small sampling depth of the photoelectron spectrum, because the transport process on the surface and the escape process from the surface are inseparable. In fact, when the electron is excited, the wave function of the final state is a wave packet, the center of which is within a "classic" escape depth under the surface [103]. When the transition occurs, the final state already has a large amplitude on the surface. So, in data analysis, we still need to be vigilant and give sufficient attention and simultaneously compare with the theoretical calculations.

2.3 Basic Principles of Spin- And Angle-Resolved Photoelectron Spectroscopy

Spin degree of freedom play a significant role in shaping the properties in quantum materials. Spin- and angle-resolved photoelectron spectroscopy (spin-ARPES) is one of such approach that has the capability of not only resolving the energy and the momentum of electrons, but also,

resolving the spin degree of freedom of electrons in solids, by coupling a spin detector to the hemispheres of a conventional ARPES analyzer.

Especially, new class of materials, which has a peculiar surface state spin texture caused by spin–orbit coupling (SOC), has attracted intensive attention recently. For examples, (1) Topological materials with strong SOC host topologically nontrivial surface states where the spin-momentum locking features are characteristic by spin texture. (2) Noncentrosymmetric materials with strong SOC, can give rise to spin-splitting effects, like Rashba spin-splitting. Rashba spin-splitting is closely related to a wide variety of novel physical phenomena, such as anisotropic magnetoresistance, Majorana fermions, Fulde-Ferrell-Larkin-Ovchinnikov (FFLO) states in superconductors, and even spintronics applications in the absence of magnetic field. (3) In strongly correlated materials, the spin can interact with charge, orbital, and lattice degrees of freedom to give rise to a variety of phenomena that cannot be well understood without a complete picture of the spin degree of freedom. Thus, the study of the spin textures in these materials is crucial, leading spin-ARPES measurement to be an indispensable tool in the investigation of the spin states of these materials.

Basically, there are two approaches to revealing the spin degree of freedom of electrons. One is using the spin-orbit interaction (SOI) of the electrons (such as, Mott, Diffuse scattering spin detectors) and the other one is using the spin-exchange interaction of ferromagnetic materials (VLEED spin detector) [104]. In the following subsection, principles of the representative Mott detector and the VLEED detector will be introduced respectively.

2.3.1 Mott scattering and Mott detector

Mott scattering, also called spin-coupled inelastic Coulomb scattering, refers to the separation of the two spin states of the electrons by scattering the electrons in the Coulomb field of heavy atoms. Figure 2.7 shows the double Mott scattering experiment in which a beam of unpolarized incident electrons is initially scattered from high-Z nuclei target. A large angle scattering from the first target produces electrons with a significant spin polarization transverse to the scattering plane. Scattering of these polarized electrons from the second target results in a left-right scattering asymmetry, that is proportional to the polarization induced by the first scattering [105].

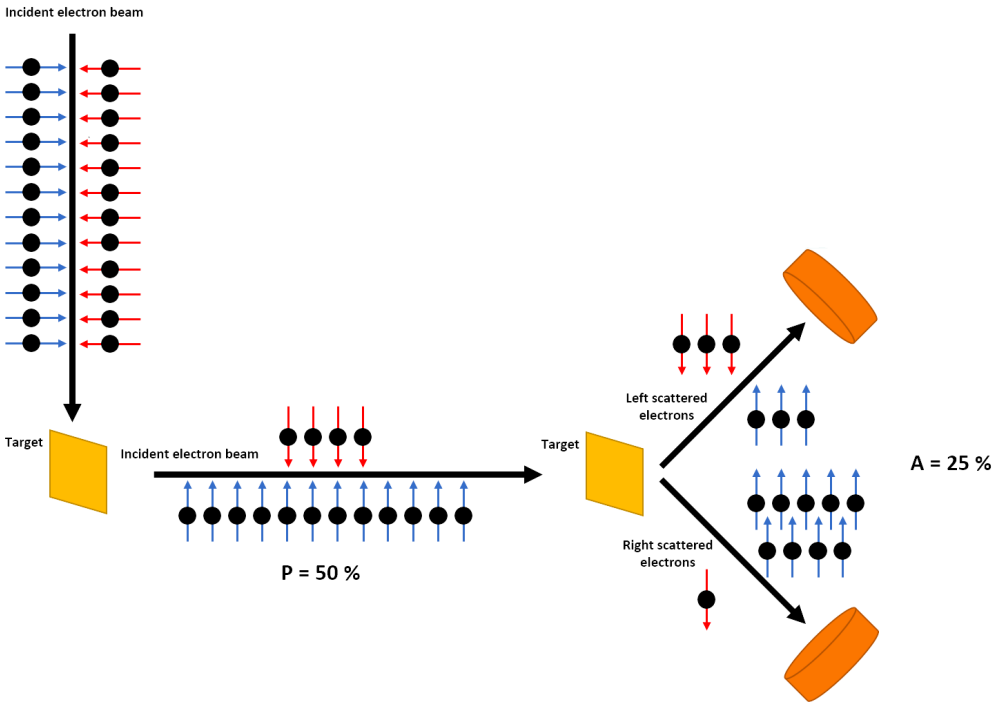

Figure 2.7 Schematic drawing of the double-scattering experiment. A unpolarized electron beam collide the first target, resulting in a beam of polarized electrons. And then collides to the second target, resulting in left-right asymmetric scattered electrons. In this figure case, supposing a value of $S(\theta) = 0.5$ is already known, and a polarized electron beam with unknown ratio of spin-up over spin-down electrons collide with the target, if the left-right asymmetry is a ratio of 3:5 (i.e., with a scattering asymmetry of 25%.), according to equation (2.4), we can derive the spin polarization of the incident electron beam is $P = 50\%$. Figure modified from ref. [106].

The classical picture of Mott scattering can be illustrated by a scattering of the electron in Coulomb field of stationary bare nucleus of charge Ze. The motion of electrons in Coulomb field $\vec{E} = -\nabla V(\vec{r}) = (Ze/r^3)\vec{r}$ of the nucleus will lead to a magnetic field $\vec{B}$ in the electron rest frame, as shown in Figure 2.8:

$$\vec{B} = -\frac{1}{c}\vec{v} \times \vec{E} = \frac{Ze}{mcr^3}\vec{L} \tag{2.41}$$

where $\vec{L} = m\vec{r} \times \vec{v}$ is the electron orbital angular momentum. The interaction of the magnetic field $\vec{B}$ with the electron magnetic momentum $\vec{\mu}_s = -\left(\frac{ge}{2mc}\right)\vec{S}$ will result in an additional scattering potential.

$$V_{so} = -\vec{\mu}_s \cdot \vec{B} = \frac{Ze^2}{2m^2c^2r^3}\vec{L} \cdot \vec{S} \tag{2.42}$$

here, $\vec{S}$ is the spin angular momentum, this term is called the spin-orbital coupling (interaction).

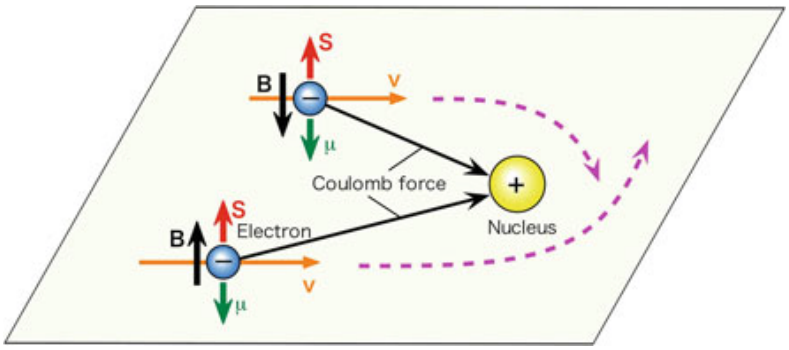

Figure 2.8 Electron experiences electric and magnetic fields in Coulomb field creating by a large Ze nucleus. Figure accessed from ref. [107].

The presence of this V_{so} term introduces a spin related term in the scattering cross section ($\sigma(\theta)$) which can be written as [108]:

$$\sigma(\theta) = \int \frac{Z^2e^4(1-\beta^2\sin^2\frac{\theta}{2})}{64\pi^2\varepsilon_0^2c^2m^2v^2\beta^2\sin^2\frac{\theta}{2}} d\Omega \propto 1 + S(\theta)\vec{\mathrm{P}}_{\mathrm{pol}}(\vec{\mathrm{r}}) \cdot \hat{\mathrm{n}} \tag{2.43}$$

where Ω represents the solid angle, $S(\theta)$ is the asymmetry function, $\vec{\mathrm{P}}_{\mathrm{pol}}(\vec{r})$ is the incident electron polarization along $\vec{r}$ direction, and $\hat{\mathrm{n}}$ is the identity vector defined incident ($\vec{k}$) and scattered ($\vec{k}'$) wave vectors $\hat{\mathrm{n}} = \vec{k} \times \vec{k}' / |\vec{k} \times \vec{k}'|$.

Back to the double-scattering experiment, the unpolarized incident electron beam can be regarded as composing equal numbers of electrons with spin angular momentum parallels and antiparallel to $\hat{\mathrm{n}}_1$. After the first scattering, we get a net polarization $\vec{\mathrm{P}}_{\mathrm{pol}}(\vec{\mathrm{r}}(\theta_1))$ given by:

$$\vec{\mathrm{P}}_{\mathrm{pol}}(\vec{\mathrm{r}}(\theta_1)) = \frac{N_\uparrow - N_\downarrow}{N_\uparrow + N_\downarrow} = S(\theta_1) \tag{2.44}$$

where $N_\uparrow$ ($N_\downarrow$) is proportional to $[1 + S(\theta_1)]$ ($[1 - S(\theta_1)]$) accroding to (2.43), which represents the number of spin-up (spin-down) electrons scattered to the left along the beam direction. In the followed, the second scattering of these polarized electron by target 2 will result in a left-right scattering asymmetry ($A(\theta_2)$) defined as:

$$\mathrm{A}(\theta_2) = \frac{N_L - N_R}{N_L + N_R} = \vec{\mathrm{P}}_{\mathrm{pol}}\left(\vec{\mathrm{r}}(\theta_1)\right) S(\theta_2) \tag{2.45}$$

where N_L (N_R) is proportional to $N_\uparrow[1 + S(\theta_2)] + N_\downarrow[1 - S(\theta_2)]$ ($N_\uparrow[1 - S(\theta_2)] + N_\downarrow[1 + S(\theta_2)]$]) accroding to (2.43), representing the number of left (right) scattered electrons if the first and second scattering events are coplanar.

Therefore, if we want to measure the spin polarization of an electron beam $\vec{\mathrm{P}}_{\mathrm{pol}}\left(\vec{\mathrm{r}}(\theta_1)\right)$, we only need to accelarete the electron beam on a target with known asymmetry function $S(\theta_2)$, and measure the scattering asymmetry ($A(\theta_2)$), then we can get the polarization of the incident beam $\vec{\mathrm{P}}_{\mathrm{pol}}\left(\vec{\mathrm{r}}(\theta_1)\right) = \mathrm{A}(\theta_2)/S(\theta_2)$. The scattering asymmetry ($S(\theta_2)$) was first proposed and calculated by Mott, and later, Sherman made a complicated calculation of electron scattering in Coulomb field from the viewpoint of relativity. For this reason, the asymmetric function is also called Sherman effective function [109], shown in (2.46).

$$S_{eff}(\theta) = \frac{i[f(\theta)g(\theta)^* - f(\theta)^* g(\theta)]}{|f(\theta)|^2 + |g(\theta)|^2} \tag{2.46}$$

here $f(\theta)$ and $g(\theta)$ represent the complex amplitude obtained by the quantum mechanical partial wave method.

Considering the error propagation of equation (2.45), we can get the expected error of the observed spin polarization (ΔP) [104]:

$$\Delta P = \frac{\sqrt{1 - A^2}}{S_{eff}\sqrt{I_L + I_R}} \cong \frac{1}{S_{eff}\sqrt{I}} = \frac{1}{\sqrt{I_0 \epsilon}} \tag{2.47}$$

where I represents the total intensity of incident electrons, I_0 is the scattered electrons, and $\epsilon = S_{eff}^2 I/I_0$ is named the figure of merit (FOM) and is used as an index of the efficiency of spin dectection. Generally, the efficiency of a Mott detector is very low, since the FOM is about 10^{-4}

orders, which means that the intensity after Mott detector is about 10^4 orders lower than that of the single-channel spin-integrated PES.

2.3.2 Very low energy electron diffraction spin detector

One feasible approach to improve the FOM, which is a fatal weakness for Mott detector for a long term, is the "Very-Low-Energy-Electron-Diffraction" (VLEED) spin detector. The VLEED from a $\mathrm{Fe}(001)-p(1\times1)-O$ surface [110,111] magnetized parallel to the surface (denoted as ↑ temporarily) can be sued as a method to measure the spin polarization derived from the reflection of the incident electrons is spin-dependent: The reflected current of incident electron whose polarization parallel to the sample magnetization ($I_\uparrow$) is not equal to the one that antiparallel to the sample magnetization ($I_\downarrow$), due to the spin exchange splitting of the unoccupied state of the band structure of this ferromagnetic materials [112-114].

Analog to the scattering asymmetry equation (2.45) in Mott scattering, the nonequal reflection current of the incident polarized electrons whose polarization is parallel and antiparallel to the magnetization of the $\mathrm{Fe}(001)-p(1\times1)-O$ surface is conveniently characterized by the reflection asymmetry current $A(I)$:

$$A(I)=\frac{I_\uparrow-I_\downarrow}{I_\uparrow+I_\downarrow} \tag{2.48}$$

So that, in VLEED experiment one just need to measure the refection asymmetry current and then the spin polarization (P) of the incident electron beam that one wants to measure is similarly given by:

$$P=A(I)/A_0 \tag{2.49}$$

where A_0 is consequently analog to the effective Sherman function charactering the VLEED detector.

Figure 2.10 schematically shows a very simple apparatus of a photoemission spectrometer equipped with a VLEED spin detector. The system mainly consists of a commercial high-energy-resolution hemispherical electron energy analyzer and the VLEED spin polarimeter. The electrons after analyzer are decelerated or accelerated to very low energy of 6 eV in the multi-stage lenses and then collide on the surface of the target. The reflected electrons are counted by the channeltron near to the exit window. The efficiency of the VLEED spin polarimeter is also

characterized by the figure of merit (FOM) $\epsilon = A_0^2 I/I_0$, where I is the intensity of incident electron beam and I_0 is the primary intensity. The FOM of a typical VLEED spin detector is about 100 times better than that of Mott detector, but the surface of the magnetic target used in this detector will be rapidly degraded, so there was almost no commercial use. However, by pre-coating a very thin oxide film on the target, like $\mathrm{Fe}(001) - p(1 \times 1) - O$, it is enabled to perform stable spin detection for several months or longer, which is basically meet the experimental requirements.

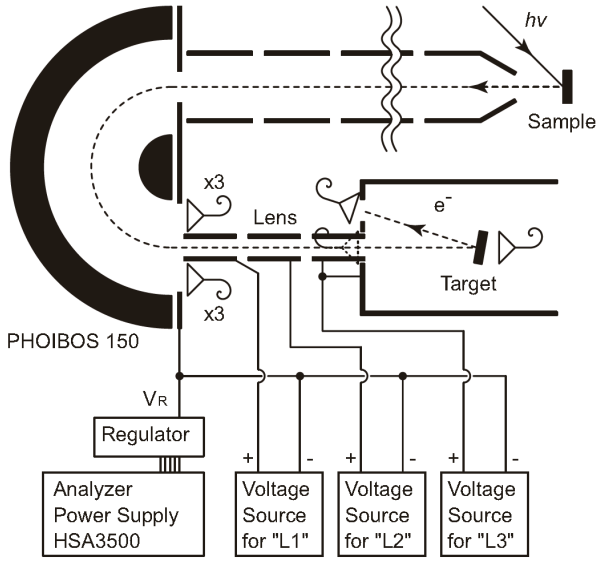

Figure 2.9 Photoemission spectrometer with VLEED spin polarimeter by specular reflection of low-energy electrons from a magnetized $\mathrm{Fe}(001) - p(1 \times 1) - O$ target. Figure accessed from ref. [114].

2.4 Facilities in A Spin- And Angle-Resolved Photoelectron Spectroscopy Apparatus

An (spin-) ARPES system generally consists of four basic parts: light source, electronic energy analyzer (for Spin-ARPES, a spin detector should be equipped), ultra-high vacuum (UHV) system and temperature-controlled sample rotation system (cryogenic manipulator system). In the following sections, details of these parts will be explained respectively.

2.4.1 The light source

Currently, there are three types of light sources suitable for APRES that are widely used: (1) synchrotron radiation light sources, (2) gas discharge light sources and (3) laser light sources.

(1) synchrotron radiation light sources

Synchrotron radiation (also known as magnetobremsstrahlung radiation) is the electromagnetic radiation emitted in the tangential direction after being deflected by a static magnetic field by high-energy charged particles accelerated to relativistic speed. Synchrotron radiation can be achieved artificially in a synchrotron or storage ring, or it can be achieved naturally by fast electrons moving in a magnetic field. The radiation generated in this way has a characteristic polarization, and the generated frequency can vary throughout the electromagnetic spectrum, which is a great merit accountable to tunable photon energy.

Under the action of the accelerating field, a high-speed point charge of mass m and charge q moving along a certain orbital plane will produce an electromagnetic field called the Liénard–Wiechert field [115].

$$\vec{B}(\vec{r},t) = -\frac{\mu_0 q}{4\pi}\left[\frac{c\hat{n}\times\vec{\beta}}{\gamma^2 R^2\left(1-\vec{\beta}\cdot\hat{n}\right)^3} + \frac{\hat{n}\times\left[\dot{\vec{\beta}}+\hat{n}\times\left(\vec{\beta}\times\dot{\vec{\beta}}\right)\right]}{R\left(1-\vec{\beta}\cdot\hat{n}\right)^3}\right]_{retarded} \tag{2.50}$$

$$\vec{E}(\vec{r},t) = \frac{q}{4\pi\varepsilon_0}\left[\frac{\hat{n}-\vec{\beta}}{\gamma^2 R^2\left(1-\vec{\beta}\cdot\hat{n}\right)^3} + \frac{\hat{n}\times\left[\left(\hat{n}-\vec{\beta}\right)\times\dot{\vec{\beta}}\right]}{cR\left(1-\vec{\beta}\cdot\hat{n}\right)^3}\right]_{retarded} \tag{2.51}$$

where $\vec{R}(t') = \vec{r} - \vec{r}_0(t')$, $R(t') = \left|\vec{R}(t')\right|$ and $\hat{n}(t') = \vec{R}(t')/R(t')$ which is the unit vector between the observation point and the position of the charge at the retarded time, and t' is the retarded time, $\vec{\beta} = \vec{v}/c$ is the velocity of the source point, $\dot{\vec{\beta}}$ thus is the acceleration of the source point. The first terms in (2.50) and (2.51) are called the generalized Coulomb field, which represents the particle static field effect, and the second terms for $\vec{B}(\vec{r},t)$ and $\vec{E}(\vec{r},t)$ is called acceleration field or radiation field, which represent the components of the radiation field due to the charged particle's motion. Thus, by ignoring the first terms, the power of the emitted radiation can be calculated as following procedures [115]:

$$\left[\vec{S}\cdot\hat{n}\right]=\frac{q^2}{16\pi^2\varepsilon_0 c}\left\{\frac{1}{R^2}\left|\frac{\hat{n}\times\left[\left(\hat{n}-\vec{\beta}\right)\times\dot{\vec{\beta}}\right]}{\left(1-\vec{\beta}\cdot\hat{n}\right)^3}\right|^2\right\}_{retarded} \tag{2.52}$$

where $\left[\vec{S}\cdot\hat{n}\right]$ is the radial component of the Poynting's vector representing the directional energy flux (the energy transfer per unit area per unit time) of an electromagnetic field. Next, the energy radiated per solid angle is:

$$\frac{dP}{d\Omega}=R(t')^2\left[\vec{S}\cdot\hat{n}\right]\frac{dt}{dt'} \tag{2.53}$$

Integrating equation (2.53), the total power is:

$$P=\frac{q^4}{6\pi\varepsilon_0 m^4c^5}B^2(E^2-m^2c^4) \tag{2.54}$$

where E is the particle's total (kinetic plus rest) energy. Further, by using $B=E\beta/qrsin(\alpha)$, here α is the angle between the velocity and the magnetic field, and r is the radius of the circular acceleration, the total power can be rewritten as:

$$P=\frac{q^2}{6\pi\varepsilon_0 m^4c^5r^2\sin^2(\alpha)}(E^2-m^2c^4)^2 \tag{2.55}$$

which shows that the power (P) emitted proportional to the e fourth power of energy (E) and decreases with the square of the radius (r) and the fourth power of the mass (m).

Undulators consisting of a periodic structure of dipole magnets can provide several orders of magnitude higher flux than that of a simple bending magnet. Considering a undulator with N periods, because of the sine like static magnetic field created by the dipole magnets, electrons moving in the periodic magnet field are forced to undergo oscillations and thus to emit radiation. By constructive interference, the brightness of the emitted radiation can be up to N^2. Simutenously, by controlling the trajectories of the moving electrons in the periodic magnetic field, the polarization of the emitted radiation can be realized. If the oscillations are confined to a plane the radiation will be linearly polarized. If the oscillation trajectory is helical, the radiation will be circularly polarized [116].

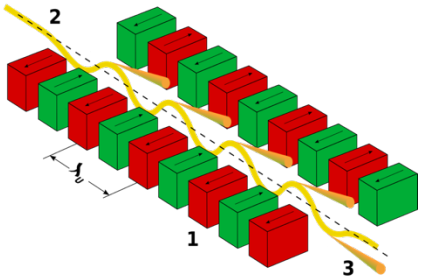

Figure 2.10 Schematic drawing of a linear undulator. 1: Alternant periodic magnet structure, 2: electron beam entering from the upper left, 3: Constructive interference synchrotron radiation exiting to the lower right. Figure is open accessed from [116].

Figure 2.12 shows the early design of a storage ring at Hiroshima synchrotron radiation center (HiSOR). It is a 700 MeV storage ring. A 150 MeV electron beam from the microtron is injected and stored in the ring, and accelerated to 700 MeV to generate synchrotron radiation [117]. Key parameters of current HiSOR accelerator system are summarized in Table 2.1.

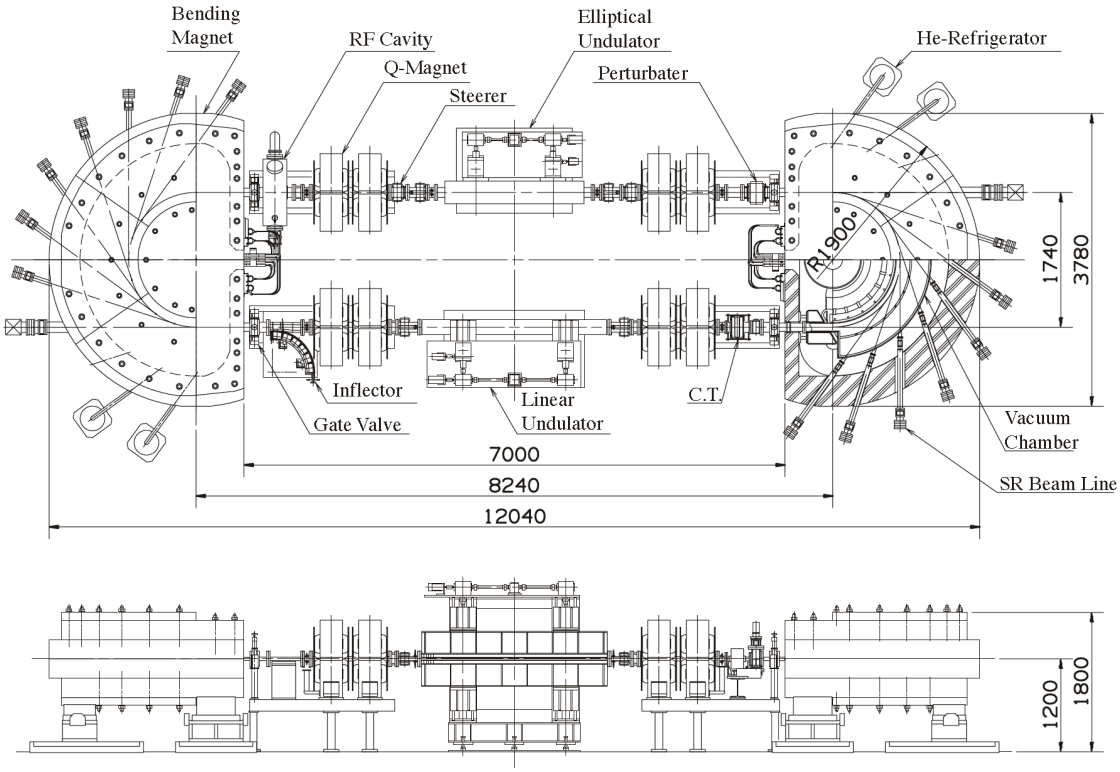

Figure 2.11 Design of HiSOR storage ring. Ref. [117].

Table 2.1 Parameters of HiSOR accelerator system, summarized form ref. [118,119]

Storage Ring	
Injector	Pulsed racetrack Microtron
Circumference of storage ring [m]	21.95
Beam energy [MeV]: Injection/Storage	150/700
Magnetic field of bending magnet [T]: Injection/Storage	0.6/2.7
Bending radius [m]	0.87
RF frequency [MHz]	191.244
RF voltage [kV]	200
Maximum stored current [mA]	350
Natural emittance [π nmrad]	400
Linear undulator (BL-1)	
Total length [m]	2.3542
Periodic length [mm]	57
Periodic number	41
Pole gap [mm]	30-200
Maximum magnetic field [T]	0.41
Variably polarizing undulator (BL-9B)	
Total length [m]	1.845
Periodic length [mm]	78
Periodic umber	23

Pole gap [mm]	22-200
Maximum magnetic field [T]: horizontal/vertical/helical	0.86/0.59/0.5

(2) Gas discharge light sources

The gas discharge light source is a commonly used light source in ARPES laboratories. The most frequently used is the He as the discharge gas, which is commonly called helium lamp. The ultraviolet spectrum generated by the de-excitation of He atoms or ions in an excited state is mainly derived from the 2p→1s transition, marked as He I, with an energy of 21.218 eV, accounting for 85% to 90% of the total intensity. The relatively weak line is the de-excitation of He^+, labeled He II, with an energy of 40.814 eV, which accounts for about 5% of the total intensity. As for other much more weaker satellite spectral lines, after passing through the monochromator, it can be filtered out, leaving only He I and He II with applicable intensity and monochromaticity.

The main advantages of the helium lamp are: low in cost, small volume, easy to move, narrow line width (about 1.25 meV for He I main line), acceptable flux even can be comparable to synchrotron radiation. However, its shortcomings are also obvious: the photon energy is discontinuous, and there are only two main spectral lines to choose (21.218eV and 40.814eV), so it cannot achieve tunable spectrum like synchrotron radiation. During the operation, it is necessary to maintain a helium pressure of about 10^{-4} mbar, and use a quartz capillary to guide the beam, so it will affect the vacuum of the main chamber. In addition, its light spot is relatively large, generally about 2mm. Moreover, its polarization is generally not adjustable, unless the helium lamp is rotated, which is quite troublesome.

It is worth noting that the use of other gas discharge light sources has also been greatly developed. For example, the use of Xe discharge light sources (xenon lamps) can obtain high-flux photons of 8.4 to 10.7 eV [120].

(3) Laser light sources

In recent years, the application of ultraviolet lasers in spin and angle-resolved photoelectron spectroscopy has also been greatly developed. In particular, the use of $KBe_2BO_3F_2$ (KBBF), a novel nonlinear optical frequency doubling crystal, realizes the frequency doubling of the 355nm

laser, thereby obtaining a 177nm (6.994eV) ultraviolet laser, which is successfully applied to a vacuum ultraviolet laser-based Angle-resolved photoelectron spectrometer with ultra-high energy resolution [76,121,122].

For many characteristics of materials, such as superconducting energy gaps of a few meV, and the detection of coupling modes in strong correlation systems, ultra-high energy resolution is strongly required. However, the photon energy used by synchrotron radiation and helium lamps is generally 20-100 eV, and the escape depth of photoelectrons is about 5-10 angstroms. If one wants to obtain the bulk signal of the sample and keep high resolution at the same time, bulk electrons must be emitted. As mentioned in section 2.3, an improved method is to use a low energy laser to probe the bulk band information.

However, not all lasers can be adopted in ARPES. Because ARPES has several constraints on the laser that can be applied: (1) In the photoelectric emission process, the energy of the photon must be greater than the work function of the material. Considering that the work function of the material is generally about 4.5 eV, plus a certain measurement energy window must be retained, the energy of the laser must be at least 5eV or more; (2) The intensity of the laser must be able to meet the requirement of ARPES, such as photon beam intensity should at least be 10^{12} photons/sec or more; (3) Since the line width of the laser directly determines the energy resolution of ARPES, in order to obtain high energy resolution, the line width of the laser must be narrow enough (for example, at least less than 10 meV for high resolution); (4) Due to the photoelectric emission process involving space charge effects, in order to achieve high energy resolution, continuous or quasi-continuous lasers should be used to reduce the number of photons in a single pulse; (5) Since the range of momentum space is directly related to the energy of laser photons, high-energy lasers are conducive to covering a larger range of momentum space. From this point of view, it is advantageous to consider a higher energy of the laser. The 6.994eV vacuum ultraviolet laser fully meets all the above conditions and is also the highest energy that can be achieved by current solid-state lasers owing to the development of KBBF crystal.

Apparently, the advantages of vacuum ultraviolet laser based ARPES are: ultra-high energy resolution, high momentum resolution, ultra-high photon flux, and greater escape depth. Table 2.2 makes a brief comparison of the main characteristics of the above three commonly used light sources.

Table 2.2 A brief comparison of synchrotron radiation, He lamp and laser light source

Light source	Synchrotron Radiation	He lamp	Laser
Energy resolution [meV]	10~20	15~40	2~8
Momentum resolution [$Å^{-1}$]	~0.001 (50eV)	~0.002 (21.1eV)	~0.0036 (6.994eV)
Photo beam intensity [Photons/sec]	10^{12}~10^{13}	10^{10}~10^{12}	10^{13}~10^{14}
Probe depth [$Å^{-1}$]	5~10	5~8	30~100

2.4.2 Hemispherical electron energy analyzer

The electron energy analyzer is one of the core components of the ARPES spectrometer. Most widely used spectrometer for ARPES is a hemispherical electrostatic electron energy analyzer, which is composed of two concentric hemispheres with a high-precision electrostatic voltage applied to the hemispheres. There are usually several stages of electrostatic lenses at the entrance of the hemisphere, which play the role of acceleration, deceleration, focusing and angle separation. There is an "electronic detection system" at the exit of the hemispherical analyzer to detect the energy and position of the photoelectrons.

The two most prominent features of the electronic energy analyzer are the realization of ultra-high energy resolution and simultaneous detection of electronic energy and angle. The electrostatic lens and hemispherical electron energy analyzer convert the energy and angle of the electrons moving in the vacuum to the position-sensitive detector. The CCD camera reads the relevant information on the detector to complete the analysis of the electron energy and momentum. In this section, we describe the VG-Scienta R4000 hemispherical electron energy analyzer, which we used in this study.

(1) Multi-element electrostatic lens

The well-designed multi-element lens is a key component to realize the simultaneous detection of electron energy and angle. The electrostatic lens collects the electrons emitted from sample and transfers them to the entrance of the energy analyzer. The lens has two important functions. One is to act as a focusing lens, producing a magnified image of the sample on the entrance plane of the analyzer. As illustrated in Figure 2.13, the trajectories are shown for two

branches of electrons being transported through a lens with a magnification of ten times. The central branch of trajectories starts on the lens axis with incident angles of 0°, ±1°, and ±2° relative to the axis along the lens, while the second set of trajectories start at the same angles, but 0.5 mm above the lens axis. After passing through this lens, the two sets of parallel trajectories focus at two different positions with ten times distance to the one at the entrance of this lens. Simultaneously, the electrons have been retarded or accelerated to a specific final energy, which is the second function of the lens.

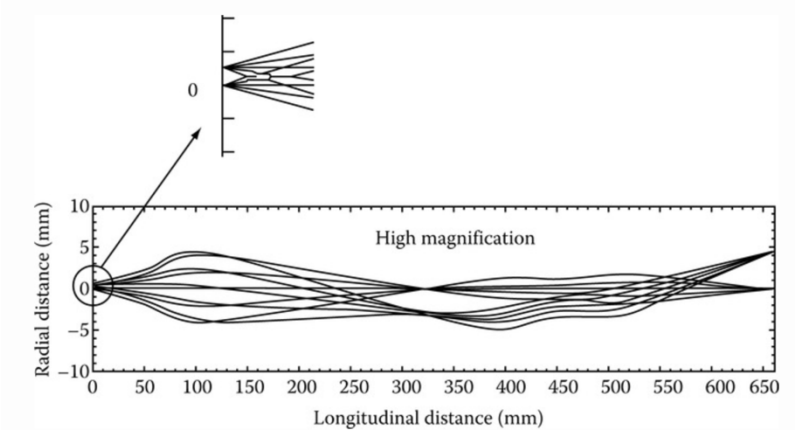

Figure 2.12 A schematic illustration of the trajectories of electrons as they move through the multi-element electron lens, each line represents the trajectory of a photoelectron at a particular angle from the sample. Figure adopted from [123].

(2) Entrance slit and hemispherical energy analyzer

Due to the spherical symmetry, a straight line at the entrance silt will be imaged onto a curved line at the exit slit. Therefore, photoelectrons entering different positions of the entrance slit (the same position can pass photoelectrons of different energies) will pass through the hemisphere analyzer in the manner shown in Figure 2.14. So that the direction of the detector from top to bottom corresponds to the angular direction, from left to right corresponds to the energy direction (see below hemispherical analyzer). Obviously, the smaller the size of the entrance slit is, the higher the energy resolution will be, but the electron counting rate will be greatly reduced. Therefore, a tunable entrance slit is designed to switch the width of the slit for balancing the energy resolution and counting rate. In addition, curved entrance silts are designed with the appropriate radius to produce straight lines at the detector.

The electrostatic hemisphere analyzer is the core component to complete the energy resolution of photoelectrons. As shown in Figure 2.14, the photoelectrons entering the radial electrostatic field generated by the two concentric hemispherical electrodes are deflected by 180°. The deflection radius depends on the initial kinetic energy of the photoelectrons, since the same position can pass photoelectrons of different energies, and thus the energy dispersion is achieved.

The energy resolution ΔE of the analyzer is determined by the pass energy, silt width, and the analyzer radius, shown as below:

$$\Delta E = E_p d_s/(R_o + R_i) \tag{2.56}$$

where E_p is the pass energy, d_s is the width of the entrance slit, and $R_o(R_i)$ is the radius of the outer (inner) hemisphere. To achieve a better energy resolution, it is wise to choose low pass energy and switch narrow silt.

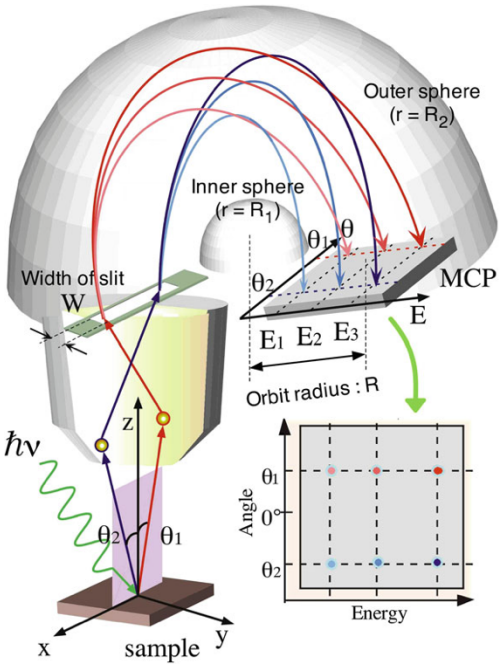

Figure 2.13 Schematic view of the electrostatic hemispherical electron energy analyzer. Electron trajectory depends on the kinetic energy and position passing through the entrance slit. Figure accessed from ref. [107].

(3) Electron detection system

The detector system is responsible for the detection of the electrons and draw a 2D (energy and angle) image, which is usually composed of micro-channel plates (MCP) and a charge-coupled device (CCD) camera.

The MCP pair consisting of two MCP plates in "Chevron" configuration multiplies each incoming electron about 10^8 times and this electron pulse is accelerated to the phosphor screen, where they produce a light flash and be detected by the CCD camera. The position of the light flash corresponds exactly to the position of the incoming electron.

The Scienta R4000 analyzer has three angular resolution modes, which can measure 30°, 14° and 7° respectively. It is easy to get that a small light spot is conducive to obtaining a better angular resolution.

2.4.3 Ultra-high vacuum (UHV) system

Since the valence electrons of impurities on the crystal surface will contribute to the photoelectron spectrum, moreover, if these impurities form chemical bond with the crystal, it will also affect the original valence electron spectrum of the crystal. Additionally, since the APRES is extremely sensitive to the surface, therefore, the sample need to be kept clean during the experiment.

The usual ARPES experiment is carried out in an ultra-high vacuum. And the vacuum level should be generally better than 10^{-9} Pa, which can be achieved by an ultra-high vacuum system composed of mechanical pumps, molecular pumps, ion pumps, titanium sublimation pumps, and vacuum valves.

In order to transfer samples quickly and not destroy the vacuum of the main chamber, the vacuum system is usually designed as a multi-stage chamber, such as load-lock chamber, transfer chamber, sample preparation chamber, and test chamber (main chamber).

For single crystal samples, in order not to break the vacuum, in-situ cleavage is generally selected in the main chamber. Usually, a thin layer of silver epoxy glue is used to mount the sample on a metal pillar, and then silver epoxy glue is used to dip a ceramic rod on the upper surface of the sample. At low temperatures, hit the ceramic rod and then a smooth and clean cleavage surface will be obtained.

2.4.4 Temperature controlled sample rotation system

For the ARPES spectrometer, on the one hand, the sample is required to be able to rotate freely to measure momentum in any direction; on the other hand, the sample must reach a sufficiently low temperature to avoid the broadening of the spectrum caused by temperature. The two aspects are often incompatible with each other, because the energy generated by the rotation of the sample will make it difficult for the sample to reach an ideal low temperature.

The manipulation of the sample is generally completed by a combination of a sample holder with three translational degrees of freedom (x, y, z) and a goniometer with three rotational degrees of freedom (polar, tilt, azimuth), which can realize the translation and rotation of the sample in the whole space. This can be accurately achieved by computer-controlled stepping motors.

In order to cool the sample on the manipulator, a continuous flow of liquid helium is used. There is a heater near the sample holder, so that the sample temperature can be changed from low temperature to high temperature to meet various experiments.

In addition, when measuring insulating materials, the accumulation of electrons on the sample surface will affect the energy and emission angle of the photoelectrons. Therefore, graphite spray can be used to increase the electrical conductivity of the sample surface.

Chapter 3 Hidden Spin Polarization in Centrosymmetric BiOI

3.1 Introduction of Hidden Spin Polarization

Numerous physical effects, such as the Dresselhaus effect [10], Rashba effect [13], optical activity in non-chiral molecules [124], valley polarization and its derivative effects [125], and valley Hall effect in two-dimensional (2D) layered structures [126] etc., are conditional on the absence of inversion symmetry (i.e., noncentrosymmetric systems) [18]. For a long time, one believes that it is unwise to seek such effects in centrosymmetric systems, however, there is a large class of special centrosymmetric systems containing a pair of noncentrosymmetric local sectors which are connected to the centrosymmetric point. For this special centrosymmetric system, the abovementioned effects do exist, but they exist in each individual sector. For the global centrosymmetric system, because of the constraint of centrosymmetry, these effects are completely compensated as a whole seemingly no difference to the trivial centrosymmetric systems.

The term "hidden effect" is thus designated to describe these effects that exists in local sectors of centrosymmetric systems which has not been realized so far. For example, the "hidden Dresselhaus effect" does exist in the diamond-type structure of Silicon, in which each atom possesses a noncentrosymmetry in each individual local sector (i.e., the tetrahedral T_d point group) but the crystal as a whole has a global centrosymmetry (i.e., the octahedral O_h group) [17,18].

Chronologically, the "hidden effect" was first explained from a theoretical predication [17] and subsequent experimental observations of "hidden Dresselhaus effect" and "hidden Rashba effect" in various nonmagnetic centrosymmetric crystals, such as bulk and monolayer transition metal dichalcogenides [20,23,127,128], $BaNiS_2$ [22], $LaO_{0.55}F_{0.45}BiS_2$ superconductor [129] and Bi2212 cuprate superconductor [24] etc. Consequently, this "hidden effect" triggered the study of a wider range of other physical effects, such as optical activity [29], intrinsic circular polarization [30], current-induced spin polarization [31,32], superconductor [130], piezoelectric polarization [17], and orbital polarization [28] in various centrosymmetric systems [18].

The spin polarization, including Rashba splitting and Dresselhaus splitting in nonmagnetic centrosymmetric materials, is thus termed as “hidden spin polarization” (HSP). The index “1” and “2” are assigned to distinguish the conventional Rashba splitting (R-1) and Dresselhaus splitting (D-1) from the hidden Rashba splitting (R-2) and Dresselhaus splitting (R-2) in centrosymmetric systems where global inversion symmetry is absent.

In this chapter, we will describe the HSP in centrosymmetric crystal BiOI. The spin-orbital coupling (which plays a key role in lowing band degeneracy) and its relative spin splitting, such as Rashba splitting and Dresselhaus splitting will be introduced in this section; and then the crystal structure and symmetries in BiOI will be analyzed in section 3.2; the electronic band structure and spin textures will be presented in section 3.3 and 3.4.

3.1.1 Origin of spin-orbital coupling effect

The spin-orbital coupling (SOC) effect enters a Hamiltonian essentially from a nonrelativistic approximation to the Dirac equation. Assuming a time dependent problem, the Dirac equation is [131]:

$$(c\boldsymbol{\alpha}\cdot\boldsymbol{p}+\boldsymbol{\beta}m_0c^2+V)\psi=E\psi \tag{3.1}$$

where $\boldsymbol{\alpha}=\begin{pmatrix}0 & \sigma\\ \sigma & 0\end{pmatrix}$ and $\boldsymbol{\sigma}=(\sigma_x,\sigma_y,\sigma_z)$ is the Pauli matrices, $\boldsymbol{\beta}=\begin{pmatrix}\mathbf{1} & 0\\ 0 & -\mathbf{1}\end{pmatrix}$ and $\mathbf{1}$ is a 2×2 identity matrix, and ψ is a four-component spinor. Rewriting this equation as a form of the upper and lower pairs of the components, ψ_A and ψ_B, it follows:

$$\boldsymbol{\sigma}\cdot\boldsymbol{p}\psi_A=\frac{1}{c}(E+m_0c^2-V)\psi_B \tag{3.2a}$$

$$\boldsymbol{\sigma}\cdot\boldsymbol{p}\psi_B=\frac{1}{c}(E-m_0c^2-V)\psi_A \tag{3.2b}$$

Eliminating the ψ_B, one obtains:

$$\boldsymbol{\sigma}\cdot\boldsymbol{p}\left[\frac{c^2}{E+m_0c^2-V}\right]\boldsymbol{\sigma}\cdot\boldsymbol{p}\psi_A=(E-m_0c^2-V)\psi_A \tag{3.3}$$

For nonrelativistic approximation, on can make a power expansion in the small quantity $(E - m_0c^2 - V)/(2m_0c^2) \approx (v/c)^2$, where the lowest order term is kept. Thus, the left-hand side of (3.3) is approximatively equal to:

$$\frac{c^2}{E + m_0c^2 - V} \approx \frac{1}{2m_0}\left[1 - \frac{E - m_0c^2 - V}{2m_0c^2} + \cdots\right] \tag{3.4}$$

where the zeroth and first order terms in $(v/c)^2$ are kept. The normalized component ψ_A (denoted $\tilde{\psi}$) derives form $\int d^3r\psi^\dagger\psi = \int d^3r\psi_A^\dagger\psi_A = 1$ and it reads [9]:

$$\tilde{\psi} = \left(1 + \frac{p^2 + e\hbar\boldsymbol{\sigma}\cdot\vec{B}}{8m_0^2c^2}\right)\psi_A \tag{3.5}$$

Substituting into (3.3), finally, the nonrelativistic approximation Dirac equation, also called Pauli equation is obtained [9]:

$$\begin{aligned}\left[\frac{p^2}{2m_0} + V + \frac{e\hbar}{2m_0}\boldsymbol{\sigma}\cdot\vec{B} - \frac{\hbar\boldsymbol{\sigma}\cdot\boldsymbol{p}\times\nabla V}{4m_0^2c^2} - \frac{\hbar^2}{8m_0^2c^2}\nabla^2 V\right.\\ \left. - \frac{p^2}{8m_0^2c^2} - \frac{e\hbar p^2}{4m_0^3c^2}\boldsymbol{\sigma}\cdot\vec{B} - \frac{(e\hbar B)^2}{8m_0^2c^2}\right]\tilde{\psi} = \tilde{E}\tilde{\psi}\end{aligned} \tag{3.6}$$

The third term on the left-hand side is the Zeeman term, the fourth term is the well-known Pauli SOC term, the fifth term is the Darwin term, the sixth term is a higher order correction to the kinetic energy $p^2/(2m_0)$ and the last two terms are also a higher order correction to the Zeeman term.

According to the Pauli SOC term, one can have a physical picture explaining the origin of the SOC that the motion of an electron in a strong Coulomb potential (V) of an atomic core regions will simultaneously generate an effective magnetic field $\vec{B}_{eff} \propto (\boldsymbol{p}\times\nabla V)$ [8]. Since the orbital magnetic moment and the spin magnetic moment of the electron are coupled into a total magnetic moment ($\mu_{total} \propto \vec{S} \propto \boldsymbol{\sigma}$) whose orientation is quantized, and the additional energy under the action of the effective magnetic field is different, which behaves as the Zeeman splitting, thus, it leads to spin splitting and spin polarization even in nonmagnetic materials.

3.1.2 Inversion asymmetry induced spin splitting

Strategies for generating highly spin-polarized electronic states in non-magnetic solids have been explored extensively because it is an important key to realize novel quantum devices [132,133]. Since a combination of both time-reversal symmetry $[E(\vec{k},\uparrow) = E(-\vec{k},\downarrow)]$ and space inversion symmetry $[E(\vec{k},\uparrow) = E(-\vec{k},\uparrow)]$ inevitably yields spin-degenerated energy levels in nonmagnetic solids. So, only when the inversion symmetry is broken can lift this degeneracy.

In nonmagnetic solids with inversion asymmetry, electrons moving through the lattice experience an asymmetric crystal potential, which results in an intrinsic SOC. This type of SOC was first described by Dresselhaus in 1955 for zinc-blende structures [10], but is generally present in crystals with bulk inversion asymmetry (BIA) [134], therefore, this kind of spin splitting is also called Dresselhaus splitting. Another type of spin splitting is the Rashba splitting originating from the structural inversion asymmetry (SIA) discussed in 1960 by Rashba [11], which states that an external electric field can also be the source for SOC, i.e., the inversion asymmetry introduced, e.g., by an external electric field applied perpendicular to a two dimensional electronic systems, or a gradient of the electrostatic potential in the interface of a heterostructure, etc.

In the following, the details on Rashba splitting and Dresselhaus splitting will be explained respectively.

(1) Rashba splitting

Considering a two dimensional free-electron like (or 2D electrons gas, 2DEG) system with a potential gradient perpendicular to the system to simulate the solid surface or interface, according to the Pauli SOC term (3.6), the Hamiltonian of this 2DEG reads:

$$\boldsymbol{H} = \frac{p^2}{2m_0}\boldsymbol{I} - \frac{\hbar}{4m_0^2c^2}\boldsymbol{\sigma}\cdot\boldsymbol{p}\times\nabla V = \frac{p^2}{2m_0}\boldsymbol{I} + \lambda_R\boldsymbol{\sigma}\cdot(\vec{\alpha}\times\boldsymbol{p}) \tag{3.7}$$

where $\boldsymbol{I} = \begin{pmatrix}1 & 0\\ 0 & 1\end{pmatrix}$, $\boldsymbol{\sigma} = (\sigma_x,\sigma_y,\sigma_z) = \left(\begin{pmatrix}0 & 1\\ 1 & 0\end{pmatrix},\begin{pmatrix}0 & -i\\ i & 0\end{pmatrix},\begin{pmatrix}1 & 0\\ 0 & -1\end{pmatrix}\right)$ are unit and Pauli matrices, $\vec{\alpha} = (0,0,\alpha_z)$, $\alpha_z \propto \nabla V$ defines the electric field given by the potential gradient, and λ_R is a fixed parameter, for simplicity, here we assume $\lambda_R = 1$. Hence, the SOC term reads:

$$\boldsymbol{\sigma}\cdot(\vec{\alpha}\times\boldsymbol{p}) = i\hbar\alpha_z(\sigma_x\partial_y - \sigma_y\partial_x) \tag{3.8}$$

Then the Hamiltonian is described by the matrix:

$$\boldsymbol{H} = \frac{p^2}{2m_0}\boldsymbol{I} + \lambda_R \boldsymbol{\sigma} \cdot (\vec{\alpha} \times \boldsymbol{p}) = \begin{pmatrix} -\frac{\hbar^2}{2m_0}\nabla^2 & i\hbar\alpha_z(\partial_y + i\partial_x) \\ i\hbar\alpha_z(\partial_y - i\partial_x) & -\frac{\hbar^2}{2m_0}\nabla^2 \end{pmatrix} \tag{3.9}$$

Choosing wave functions as $\varphi_{k\uparrow} = \frac{1}{\sqrt{\Omega}} e^{i\vec{k}\cdot\vec{r}} \begin{pmatrix} 1 \\ 0 \end{pmatrix}$ and $\varphi_{k\downarrow} = \frac{1}{\sqrt{\Omega}} e^{i\vec{k}\cdot\vec{r}} \begin{pmatrix} 0 \\ 1 \end{pmatrix}$, then the matrix elements of this Hamiltonian can be calculated as:

$$\boldsymbol{H} = \begin{pmatrix} \frac{\hbar^2 k^2}{2m_0} & -\hbar\alpha_z(ik_x + k_y) \\ \hbar\alpha_z(ik_x - k_y) & \frac{\hbar^2 k^2}{2m_0} \end{pmatrix} \tag{3.10}$$

The off-diagonal terms induce the Rashba splitting away from the $\bar{\Gamma}$ point. The Rashba term is also written as $\vec{\sigma} \cdot (\vec{\alpha} \times \vec{k})$ or $\vec{\alpha} \cdot (\vec{k} \times \vec{\sigma})$ or $\alpha(\sigma_x k_y - \sigma_y k_x)$. Subsequently, the eigen value of the secular equation $\boldsymbol{H}\psi = \varepsilon\psi$ is:

$$\varepsilon_{\pm} = \frac{\hbar^2 k^2}{2m_0} \pm \hbar\alpha_z|k| = \frac{\hbar^2}{2m_0}\left(|k| \pm \frac{m\alpha_z}{\hbar}\right)^2 - \frac{m\alpha_z^2}{2} \tag{3.11}$$

At $k = 0$ (time-reversal invariant momentum), the energy is degenerated. For the momentum region $|k| \ll 1$, the energy is given by $\varepsilon_{\pm} \approx \pm\hbar\alpha_z|k|$, forming the so called "Dirac cone". For the energy dispersion, it looks like two parabolas shifted along k direction by $|k| = \pm\frac{m\alpha_z}{\hbar}$.

Next, assuming the eigen functions corresponding to $\varepsilon_{\pm}$ are $\varphi_k^{\pm} = \mu\varphi_{k\uparrow} + \nu\varphi_{k\downarrow}$, due to $|\mu|^2 + |\nu|^2 = 1$, the eigen functions can be written as:

$$\varphi_k^{\pm} = \frac{1}{\sqrt{2\Omega}} \begin{pmatrix} \mp e^{\pm i\theta} \\ 1 \end{pmatrix} e^{i\vec{k}\cdot\vec{r}} \tag{3.12}$$

where $\tan\theta = \frac{k_x}{k_y}$. Within this eigen functions, the expectation values of the spin direction can be calculated easily by $\boldsymbol{s}_{\pm} = \langle\varphi_k^{\pm}|\boldsymbol{s}|\varphi_k^{\pm}\rangle$, here $\boldsymbol{s} = \hbar\boldsymbol{\sigma}/2$, which are shown below:

$$\boldsymbol{s}_{\pm} = \frac{\hbar}{2k}\left(\mp k_y, \pm k_x, 0\right) \tag{3.13}$$

which states that the spin angular momenta are within the xy plane and orthogonal to the momentum direction ($\boldsymbol{s}_{\pm} \cdot \vec{k} = 0$) with the same length of $\left|\boldsymbol{s}_{\pm}\right| = \hbar/2$ but antiparallel to each other. As for the spin magnetic momenta, they are given by $\boldsymbol{\mu}_s^{\pm} = -g\mu_B \boldsymbol{s}_{\pm}$, here μ_B is the Bohr magneton, and g is the Landé g-factor (in the case of electron spin, g=2), as illustrated in the Figure 3.1.

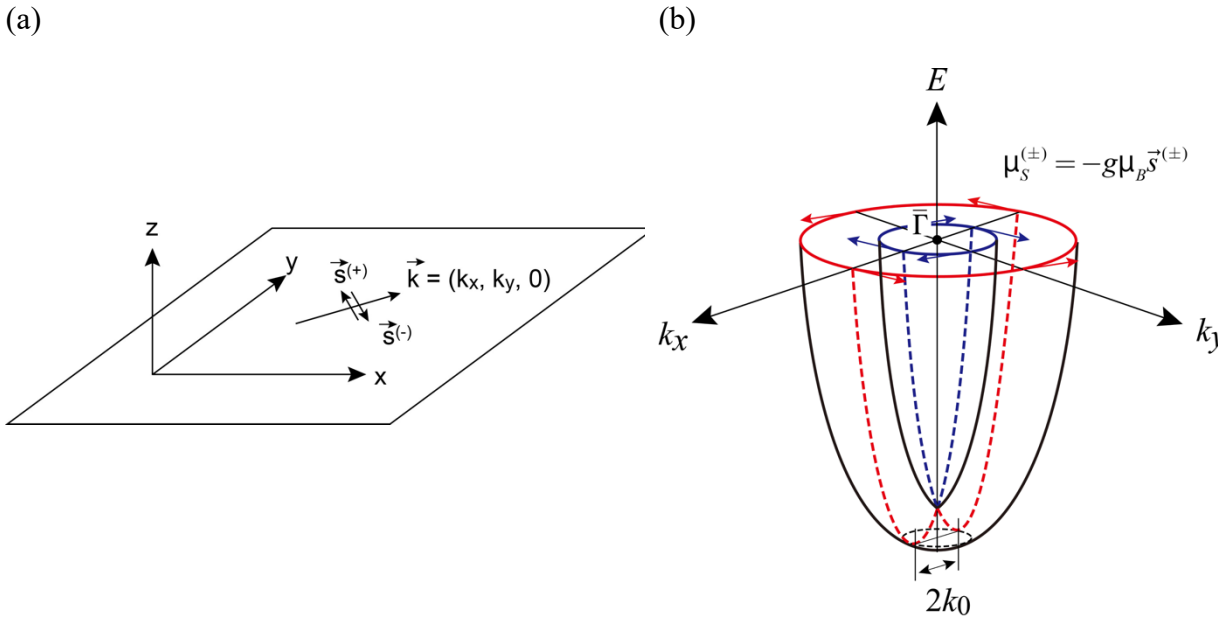

Figure 3.1 Schematic drawing of the spin angular momenta and spin magnetic momenta in Rashba splitting. (a) the spin angular momenta $\boldsymbol{s}_{\pm}$ are orthogonal to the momentum direction $\vec{k} = (k_x, k_y, 0)$ and the two components are antiparallel to each other. (b) the spin magnetic momenta $\boldsymbol{\mu}_s^{\pm}$ show the same physics to $\boldsymbol{s}_{\pm}$, but for opposite direction and magnitude due to $\boldsymbol{\mu}_s^{\pm} = -g\mu_B \boldsymbol{s}_{\pm}$. Figures accessed from my supervisor's lecture.

(2) Dresselhaus splitting

The Dresselhaus splitting was originally discussed in a BIA zinc blende structure by G. Dresselhaus in 1955 [10]. Dresselhaus started from one electron Schrodinger equation with SOC term:

$$\left[\frac{p^2}{2m} + V + \frac{\hbar}{4m_0^2c^2}\boldsymbol{\sigma}\cdot(\nabla V \times \boldsymbol{p})\right]\Psi_k = E_k\Psi_k \tag{3.14}$$

The translational symmetry of the zinc blende lattice requires that the wave function (Ψ_k) should be of the form of Bloch function $\left[\Psi_k = u_k(\vec{r})e^{i\vec{k}\cdot\vec{r}}\right]$, here the periodic part ($u_k(\vec{r})$) should satisfy the equation:

$$\begin{aligned}\left[\frac{p^2}{2m} + V + \frac{\hbar}{4m_0^2c^2}\boldsymbol{\sigma}\cdot(\nabla V \times \boldsymbol{p})\right]u_k + \hbar k\cdot\left(\frac{\boldsymbol{p}}{m} + \frac{\hbar}{4m_0^2c^2}\boldsymbol{\sigma}\times\nabla V\right)u_k \\ = \left(E_k - \frac{\hbar^2k^2}{2m}\right)u_k\end{aligned} \tag{3.15}$$

For the extended $k + K$, one just replaces the k by $k + K$ in (3.15), then treats the term $\hbar k \cdot \left(\frac{\boldsymbol{p}}{m} + \frac{\hbar}{4m_0^2c^2}\boldsymbol{\sigma}\times\nabla V\right) = \mathcal{H}'$ as a perturbation, thus, the energy at $k + K$ for a nongenerated level is:

$$E_{k+K} = E_k + \frac{\hbar^2k^2}{2m} + (\Psi_k|\mathcal{H}'|\Psi_k) + \cdots \tag{3.16}$$

Dresselhaus discussed the secular determinant with the first order perturbation in k at Γ_8:

$$\begin{vmatrix} -\lambda & \left(\frac{i}{2}\right)Ck_+ & -Ck_z & -\left(\frac{i\sqrt{3}}{2}\right)Ck_- \\ \left(-\frac{i}{2}\right)Ck_- & -\lambda & -\left(\frac{i\sqrt{3}}{2}\right)Ck_+ & Ck_z \\ -Ck_z & \left(\frac{i\sqrt{3}}{2}\right)Ck_- & -\lambda & \left(\frac{i}{2}\right)Ck_+ \\ \left(\frac{i\sqrt{3}}{2}\right)Ck_+ & Ck_z & \left(-\frac{i}{2}\right)Ck_- & -\lambda \end{vmatrix} = 0 \tag{3.17}$$

where $\lambda = \pm C\left\{k^2 \pm \left[3\left(k_x^2k_y^2 + k_y^2k_z^2 + k_z^2k_x^2\right)\right]^{1/2}\right\}^{1/2}$ with $C = -\frac{1}{2\sqrt{3}}\frac{\hbar^2}{m^2c^2}\left(\delta_1\left|\frac{\partial V}{\partial y}\right|\delta_3\right)$ here δ is the bases for the irreducible representations of T_d^2 at Γ that can be selected from any group theory textbook, and $k_\pm = k_x \pm ik_y$, this invariant is often called the Dresselhaus matrix element.

Now, when we deal with 2D structures or the [001] direction is infinite, the Dresselhaus Hamiltonian can be simplified as:

$$\boldsymbol{H}_D = \begin{vmatrix} \mathcal{O}(\lambda) & \left(\frac{i}{2}\right) C_k k_+ \\ \left(\frac{i}{2}\right) C_k k_+ & \mathcal{O}(\lambda) \end{vmatrix} = \beta \begin{vmatrix} 0 & k_+ \\ k_- & 0 \end{vmatrix} \tag{3.18}$$

where the $\mathcal{O}(\lambda)$ is an infinitesimal, $C_k = -\frac{1}{2\sqrt{3}} \frac{\hbar^2}{m^2 c^2} \left(x \left| \frac{\partial V}{\partial y} \right| z \right)$, and $\beta = iC_k/2$ is a coupling constant describing the BIA SOC strength. The Dresselhaus Hamiltonian can be also conveniently denoted as:

$$\boldsymbol{H}_D = \beta(\sigma_x k_x - \sigma_y k_y) \tag{3.18}$$

Analog to Rashba splitting, considering a 2DEG system with Dresselhaus SOC term, the Hamiltonian can be written as:

$$\boldsymbol{H} = \begin{pmatrix} \frac{\hbar^2 k^2}{2m_0} & \beta(k_x + ik_y) \\ \beta(k_x - ik_y) & \frac{\hbar^2 k^2}{2m_0} \end{pmatrix} \tag{3.19}$$

The Dresselhaus off-diagonal terms $\beta(k_x \pm ik_y)$ play a key role in the degenerated levels splitting. The eigen value of this secular equation $\boldsymbol{H}\psi = \varepsilon\psi$ is:

$$\varepsilon_\pm = \frac{\hbar^2 k^2}{2m_0} \pm \beta|k| = \frac{\hbar^2}{2m_0} \left(|k| \pm \frac{m\beta}{\hbar^2} \right)^2 - \frac{m\beta^2}{2\hbar^2} \tag{3.11}$$

The energy dispersion looks like two parabolas shifted along k direction by $|k| = \pm\frac{m\beta}{\hbar^2}$, showing a very similar behavior as Rashba splitting.

The eigen functions can be written as:

$$\varphi_k^\pm = \frac{1}{\sqrt{2\Omega}} \begin{pmatrix} \mp e^{\pm i\theta} \\ 1 \end{pmatrix} e^{i\vec{k}\cdot\vec{r}} \tag{3.12}$$

Consequently, the expectation values of the spin direction are:

$$\boldsymbol{s}_\pm = \frac{\hbar}{2k} (\mp k_x, \pm k_y, 0) \tag{3.13}$$

Figure 3.2 shows a schematic summary of the band structures and spin textures of the degenerated bands, nonmagnetic Zeeman splitting, Rashba splitting and Dresselhaus splitting in 3D (a) and 2D (b) and (c) space. The arrows represent the spin magnetic momentum ($\boldsymbol{\mu}_S^{\pm}$) orientations (by $\boldsymbol{\mu}_S^{\pm} = -g\mu_B \boldsymbol{s}_{\pm}$). The calculated results of the spin texture in panel (c) were obtained from the Zeeman term ($\lambda_Z \boldsymbol{\sigma} \cdot \boldsymbol{B}$), Rashba term [$\alpha(\sigma_x k_y - \sigma_y k_x)$], Dresselhaus term [$\beta(\sigma_x k_x - \sigma_y k_y)$]. It shows that the Zeeman splitting is shifted along $E(k)$ axis, while the Rashba and Dresselhaus splitting are shifted along the k axis. The characteristic parameters (α and β) quantifying the strength of the splitting, which are of great difficulty to calculate from theory, however, can be easily determined from an ARPES band dispersion. If one obtains a sharp Rashba or Dresselhaus band dispersion, then just to measure either the momentum shift (k_R or k_D) or the energy shif (Δ_R or Δ_D) with respect to the Dirac point, shown in panel (c), finally, the characteristic parameters (α and β) can be estimated:

$$\alpha(\beta) = \frac{\hbar^2}{m} k_{R(D)} \text{ or } \sqrt{\frac{2\hbar^2}{m} \Delta_{R(D)}} \tag{3.14}$$

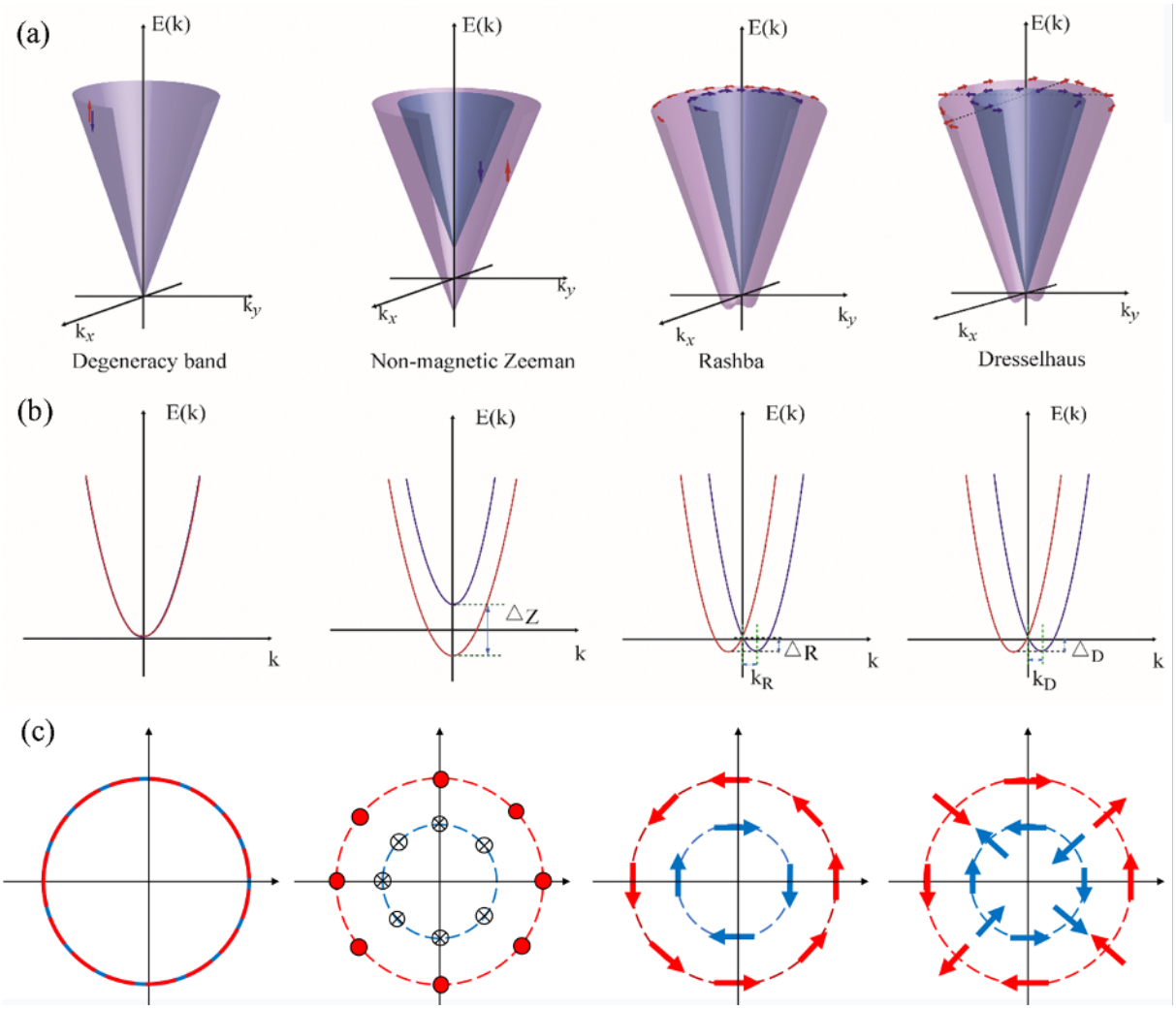

Figure 3.2 Schematic drawing of band structures and spin textures of the degenerated band, nonmagnetic Zeeman, Rashba and Dresselhaus effects. Figure modified from ref. [135].

3.1.3 Hidden spin polarizations in centrosymmetric systems

The previous section 3.1.2 mainly introduced the conventional Rashba splitting (R-1) and Dresselhaus splitting (D-1) originated from inversion asymmetry in noncentrosymmetric crystals. In this section we will continue to introduce the recently discovered hidden Rashba splitting (R-2) and Dresselhaus splitting (D-2) in centrosymmetric crystals.

The starting point to describe the SOC-induced spin polarization effects of R-2 and D-2 is that the SOC is a relativistic effect anchored on particular nuclear sites in the solid. The inversion

asymmetry of such individual atomic sites (or local sectors) may result in the non-zero total spin polarization of a local sector [17].

In more detail, the atomic site can be either nonpolar (an inversion asymmetric local environment: Bulk Inversion Asymmetry (BIA)) or polar (a local environment with a dipole field: Structural Inversion Asymmetry (SIA)). In the former case, the SOC on the atomic site will lead to a local Dresselhaus splitting, whereas in the latter case it will lead to a local Rashba splitting, as explained in section 3.1.2. For a layered crystal with each of its individual layers (sectors) having a local inversion asymmetry produces a local Rashba splitting or local Dresselhaus splitting. The Rashba splitting or Dresselhaus splitting on each local sector is compensated by the other sector (its inversion partner), because of the centrosymmetric properties of the whole crystal. This local Rashba splitting or local Dresselhaus splitting is concealed by the compensation of its inversion partner, in spite that it is not intrinsically absent. These concealed spin splitting is thus called hidden spin polarization (HSP).

Table 3.1 shows a summary on the classification of spin polarization in nonmagnetic materials based on the bulk space group and site point group, which forms the basis of the HSP. The point group is given in Schoenflies notation. Site point group refers to the operations that transform the atomic site to itself, which is a subset of symmetry operations of the bulk space group. Polar point group is the subset of point group, which contains a unique anisotropic axis producing a nonzero dipole field. When the site point group is noncentrosymmetric with at least one site has a non-centrosymmetry and all the sites are nonpolar (D_2, D_3, D_4, S_4, D_{2d}, C_{3h}, D_{3h}, T, T_d, O), thus there is a D-1 spin polarization for the bulk space group with noncentrosymmetry and D-2 spin polarization for centrosymmetric system. If some of the site point groups are polar (C_1, C_2, C_3, C_4, C_6, C_{1v}, C_{2v}, C_{3v}, C_{4v}, C_{6v}) and the induced dipole fields add up to an infinitesimal amount, there is a D-1 spin polarization for the bulk space group with noncentrosymmetry, while when the dipoles add up to nonzero, there are both D-1 & R-1 spin polarizations in this noncentrosymmetric system. When the site point group contains polar point groups (C_1, C_2, C_3, C_4, C_6, C_{1v}, C_{2v}, C_{3v}, C_{4v}, C_{6v}), in this case there are R-2 accompanied by D-2 compensated spin polarizations for the space group with centrosymmetric system. When the site point group is centrosymmetric, the space group can be noncentrosymmetric, in which case the spin polarization is not possible to exist, or the space group can be centrosymmetric, in which case the spin polarization is absent.

Table 3.1 Classification of spin polarization in nonmagnetic bulk materials on the basis of bulk space group and site point group [17].

Site point group / Bulk space group	Noncentrosymmetric (at least one site)			Centrosymmetric (all sites) $(C_i, C_{2h}, C_{4h}, D_{4h}, S_6, D_{3d}, D_{6h}, C_{6h}\ T_h, O_h)$
	Nonpolar (all sites) $(D_2, D_3, D_4, S_4, D_{2d}, C_{3h}, D_{3h}, T, T_d, O)$	Polar (at least one site) $(C_1, C_2, C_3, C_4, C_6, C_{1v}, C_{2v}, C_{3v}, C_{4v}, C_{6v})$		
		Dipoles add up to zero	Dipoles add up to nonzero	
Noncentrosymmetric	D-1	D-1	D-1 & R-1	Impossible (Site point group cannot be centrosymmetric if space group is noncentrosymmetric)
Centrosymmetric	D-2	D-2 & R-2		Absence of spin polarization

We should also note that the Rashba splitting (R-1 and R-2) is always accompanied by the Dresselhaus splitting (D-1 and D-2). This is because the site polar point group contains simultaneously site inversion asymmetry that shows the same effect as BIA for Dresselhaus splitting, thus, the Rashba splitting in bulk crystals is always accompanied by the Dresselhaus splitting (in noncentrosymmetric system, the individual dipole field should add up to a nonzero value).

The spin polarization of the energetically degenerate bands is spatially segregated into a dominant spin texture which is associated with its inversion partner. This feature originates essentially from the wavefunction segregation. To explicitly quantify the degree of wavefunction segregation (DWS) of the wavefunction, an index $D(\psi_k)$ for state ψ_k should be introduced, which is formulated as:

$$D(\psi_k) = \left| \frac{P_{\psi_k}(S_\alpha) - P_{\psi_k}(S_\beta)}{P_{\psi_k}(S_\alpha) + P_{\psi_k}(S_\beta)} \right| \tag{3.15}$$

where $P_{\psi_k}(S_{\alpha,\beta}) = \int_{\Omega \in S_{\alpha,\beta}} |\psi_k(\vec{r})|^2 d^3\vec{r}$ is the component of the wavefunction ψ_k localized on the sector α and sector β ($S_{\alpha,\beta}$). Note that the implicit meaning of the index is the integral of the

local spin density restricted on a given sector. It is evident that $D(\psi_k) = 100\%$ indicates that the wavefunction is entirely confined either on sector α or sector β. For example, L. Yuan et al. had shown the segregation of wavefunction in $BaNiS_2$ monolayer to be 88% ($D(\psi_k) = 88\%$) at k =(0.025, 0.5, 0) ($2\pi/a$), here a is the lattice constant, for both spin components of doubly degenerate branches along Brillouin zoom (BZ) boundary. The segregation of wavefunctions on a single sector with $D(\psi_k) = 88\%$ for the states along BZ direction indicates that this band experiences a net effective field of the internal dipole fields within a single sector and free from a full compensation from the opposite dipole fields within its inversion partner sector [17]. Spin-momentum-sector locking is, thus, an observable consequence of the feature of wavefunction segregation.

In brief, the key point of R-2 and D-2 is that these spin splitting originate fundamentally from specific atomic site asymmetries (local site symmetries), rather than, as general view described in section 3.1.2, from the structural and bulk inversion asymmetry (SIA and BIA) of the crystal space group (global crystal symmetries) [17]. This insight reveals that these Rashba as well as Dresselhaus splittings should exist in centrosymmetric crystals but on each local sector. Although all energy bands must be doubly degenerate in centrosymmetric crystals as a whole, in fact, the two components of such doubly degenerate bands could have opposite polarizations, each spatially localized on one of the two separate sectors forming the inversion partners [17], in other words, forming the spin-momentum-sector locking.

3.2 Crystal Structure of Bismuth Oxyiodide (BiOI)

The view of R-2 and D-2 has greatly enlarged the playing field of spintronic materials to centrosymmetric materials with the significant SOC. To find materials that have a significant R-2 or D-2 spin polarization, there are two important filter conditions: (1) look for compounds that have centrosymmetric space groups but with at least one of the Wyckoff positions lacking inversion symmetry and belonging to either polar (R-2) or nonpolar (D-2) point groups. Here, out of the 230 space groups, 92 are centrosymmetric, and out of the 32 point groups, 21 are noncentrosymmetric. This condition is needed to introduce SOC, i.e., designing individual sectors with maximal asymmetry of the local potential within the sector [18]. (2) Spatially minimize the mixing and entanglement of the wavefunction on the different inversion partners (sectors), i.e., enhance the segregation of the wavefunction on each sector. For example, the layered materials may have a small interaction between the opposite sectors due to the barrier

layer separating the two opposite sectors. Another nontrivial way to minimize the interaction of the two opposite sectors is the symmetry-enforced wavefunction segregation, where due to the restriction of symmetries, the doubly degenerated states on the opposite sectors are fully free from mixing, such as the nonsymmorphic symmetry in $BaNiS_2$ [18]. Other symmetry operations enforcing wavefunction segregation may exist, but they have not been discovered yet.

3.2.1 Symmorphic and nonsymmorphic symmetry

In this section, we will introduce a case of bismuth oxyiodide (BiOI) that is filtered according to above mentioned restrictions. To well understand the crystal structure of BiOI, first, the symmorphic and nonsymmorphic symmetries will be explained in section 3.2.1, and then all the symmetries in BiOI will be discussed in section 3.2.2.

The space group G consists of all operations $\{\boldsymbol{\alpha}|\vec{\tau}\}$ which leave a given lattice invariant ($\{\boldsymbol{\alpha}|\vec{\tau}\}\vec{r} = \boldsymbol{\alpha}\cdot\vec{r} + \vec{\tau} = \vec{r}'$). The elements in a space group can be written as the form of:

$$\{\alpha|\tau\} = \{\alpha|R_n + \tau_\alpha\} = \{\varepsilon|R_n\}\{\alpha|\tau_\alpha\} \tag{3.16}$$

where α is the point group operators, R_n is a general vector of the Bravais lattice and τ_α is either zero or a nonintegral translation vector of the Bravais lattice. According to this notation, the classification of symmorphic and nonsymmorphic symmetries in space group is: if all the elements of space group G are in the form of $\{\alpha|\tau\} = \{\alpha|R_n\} = \{\varepsilon|R_n\}\{\alpha|0\}$ ($\tau_\alpha = 0$), then the space group G is called a simple or symmorphic group and all of the elements $\{\alpha|R_n\}$ are called symmorphic operations, while, if at least one element $\{\alpha|\tau_\alpha\}$ in space group G with $\tau_\alpha \neq 0$, then the space group G is classified as nonsymmorphic group and the element $\{\alpha|\tau_\alpha\}$ is called nonsymmorphic operation [136].

In order to represent the space group elements, the basis $\begin{pmatrix}1\\ \vec{r}\end{pmatrix} = (1, x, y, z)^T$ should be introduced. Then the matrix representation for the space group operator is defined as:

$$\{\alpha|\tau\} = \begin{pmatrix}1 & 0\\ \curlyvee & M_\alpha\end{pmatrix} \tag{3.17}$$

where 1 is a number, 0 denotes a row of three zeros, $\curlyvee$ is a 3×1 column vector, and M_α is a (3×3) matrix. Therefore, the action of the space group operation on the coordinate system is consequently written as:

$$\{\alpha|\tau\}\begin{pmatrix}1\\ \vec{r}\end{pmatrix}=\begin{pmatrix}1 & 0\\ r & M_\alpha\end{pmatrix}\begin{pmatrix}1\\ \vec{r}\end{pmatrix}=\begin{pmatrix}1\\ M_\alpha\cdot\vec{r}+r\end{pmatrix}=\begin{pmatrix}1\\ \vec{r'}\end{pmatrix} \tag{3.18}$$

Out of the 230 space groups, there are 73 symmorphic space groups and 157 nonsymmorphic space groups, which can be found in the "*International tables for crystallography*" [137]. When expressing a space group, the international notation (Hermann-Mauguin or HM) is the most used. This notation consists of two parts: the first part is the type of Bravais lattice, where P, I, F (A, B or C) and R, respectively, denote primitive, body centered, face centered, base centered (along the a, b or c crystallographic axis) and rhombohedral Bravais lattices; the latter part describes the most prominent symmetry operation visible when projected along one of the high symmetry directions of the crystal, which is basically the same as the international symbol of the point group with the addition of glide planes and screw axis. Table 3.2 gives the viewing directions of the seven Bravais lattice for international notation in space group and point group.

Table 3.2 The sequence of international notation for space group or point group

Position	Triclinic	Monoclinic	Orthorhombic	Tetragonal	Trigonal	Hexagonal	Cubic
1	—	b	a	c	c	c	a
2	—	—	b	a	a	a	[111]
3	—	—	c	[110]	[210]	[210]	[110]

In the case of the space group $P4_2/nnm$ (or $P4_2\ 2/n\ 2/m$, No.134), the P indicates that the Bravais lattice is primitive, the first position $4_2/n$ represents that along c axis or [001] direction (the characteristic 4-fold rotation reveals this space group belongs to tetragonal lattice), there is a 4_2 screw axis paralleling to it and a n-glide plane $[(a+b)/2]$ perpendicular to it, the second position $2/n$ shows that along a axis or [100] direction, there is a 2-fold rotation and a n-glide plane $[(b+c)/2]$ perpendicular to it, the third position $2/m$ shows that along [110] direction, there is a 2-fold rotation and a mirror plane perpendicular to it. Note in the tetragonal system, the [100] direction and [010] direction are identical, thus the 2-fold rotation, n-glide and mirror plane should be double.

3.2.2 Symmetries in BiOI

BiOI has a tetragonal crystal structure with a centrosymmetric space group $P4/nmm$ ($P4/n\ 2_1/m\ 2/m$, No.129) and has the layered structure with an ordered packing of five atom

layers in the sequence of I-Bi-O-Bi-I along the direction of c-axis, as shown in Figure 3.3(a), in which one O atom is coordinated by four Bi atoms, forming a tetrahedron with the O atom at the centre shown in Figure 3.3(c). The Bi (I) atom is coordinated by four I (Bi) atoms, forming a [BiI] pyramid with Bi (I) atom at the spire of the pyramid, as shown in Figure 3.3(d) [Figure 3.3(e)].

A distinct feature is that the [BiI] pyramids and O layer stack alternating with the opposite [BiI] pyramids in the layered structures, shown in Figure 3.4. It can be seen clearly that the layered structure contains two opposite types of [BiI] pyramid along c-axis and a $a/2$ translation in a-axis, in which the opposite [BiI] layers connected by sharing the oxygen layer. From this side-view structure of BiOI, the obviously open [BiI] layer is stacked incompactly by comprising a layer of O atom slab that plays a role of minimizing the interaction of the opposite [BiI] layer, which is conductive to enhancing the HSP effect. Consequently, the opposite [BiI] layers are denoted here as sector α and sector β, also shown in Figure 3.3(a). Another feature is that there is an enough space, which can be regarded as vacuum slab, between [BiI] layer and the opposite [BiI] layer in another unit cell. This vacuum slab can also minimize the interaction between the [BiI] layer and its inversion partner. What is more, the vacuum slab makes the layered material very easy to cleave due to weak van der Waals force, such that the HSP effect localized on the separated real sector has a practical application potential.

As indicated in the space group $P4/nmm$ ($P4/n\ 2_1/m\ 2/m$), the BiOI is a primitive Bravais lattice with C_4 operations (including $C_4^1, C_4^2 = C_2, C_4^3, e$) as the principle axis along [001] direction and a n-glide plane [$\{M_z|(1/2,1/2,0)\}$] perpendicular to the principle axis [for O atoms, shown in Figure 3.3(f) whose point group is D_{2d}], two 2_1 screw axes along [100] and [010] directions and two mirror planes perpendicular to them respectively, two C_2 rotation axes along [110] and [1-10] directions and two mirror planes perpendicular to them respectively [for Bi and I atoms shown in Figure 3.3(g) whose point group is C_{4v}]. Note that the screw axes are located at the centre of two distinct Bi atoms. In total, there are 16 symmetry operators in the $P4/nmm$ space group. They are:

$$\{e|0\}(x,y,z) = (x,y,z) \tag{3.18a}$$

$$\{C_{2z}^1|0\}(x,y,z) = (-x,-y,z) \tag{3.18b}$$

$$\{C_{4z}^1|(1/2\,,1/2\,,0)\}(x,y,z) = (-y+1/2\,,x+1/2\,,z) \tag{3.18c}$$

$$\{C_{4z}^3|(1/2\,,1/2\,,0)\}(x,y,z) = (y+1/2\,,-x+1/2\,,z) \tag{3.18d}$$

$$\{C_{2y}^{1}|(1/2\,,1/2\,,0)\}(x,y,z)=(-x+1/2\,,y+1/2\,,-z) \quad (3.18e)$$

$$\{C_{2x}^{1}|(1/2\,,1/2\,,0)\}(x,y,z)=(x+1/2\,,-y+1/2\,,-z) \quad (3.18f)$$

$$\{M_zM_xC_{4z}^{1}|0\}(x,y,z)=(y,x,-z) \quad (3.18g)$$

$$\{M_zM_yC_{4z}^{3}|0\}(x,y,z)=(-y,-x,-z) \quad (3.18h)$$

$$\{i|(1/2\,,1/2\,,0)\}(x,y,z)=(-x+1/2\,,-y+1/2\,,-z) \quad (3.18i)$$

$$\{M_z|(1/2\,,1/2\,,0)\}(x,y,z)=(x+1/2\,,y+1/2\,,-z) \quad (3.18j)$$

$$\{M_xC_{4z}^{1}|0\}(x,y,z)=(y,-x,-z) \quad (3.18k)$$

$$\{M_zC_{4z}^{3}|0\}(x,y,z)=(-y,x,-z) \quad (3.18l)$$

$$\{M_x|0\}(x,y,z)=(x,-y,z) \quad (3.18m)$$

$$\{M_y|0\}(x,y,z)=(-x,y,z) \quad (3.18n)$$

$$\{M_xC_{4z}^{3}|(1/2\,,1/2\,,0)\}(x,y,z)=(-y+1/2\,,-x+1/2\,,z) \quad (3.18o)$$

$$\{M_xC_{4z}^{1}|(1/2\,,1/2\,,0)\}(x,y,z)=(y+1/2\,,x+1/2\,,z) \quad (3.18p)$$

The matrix representations for all the symmetry operators are listed in the Appendix A. Among the 16 symmetry operators, there are 8 symmetry operators marked with red color, under which the X point is invariant (i.e., $\{\alpha|\tau\}\vec{k}_x=\alpha\vec{k}_x+\vec{\tau}=\vec{k}_x+\vec{G}$) [18], which will be discussed in more detail in the next section.

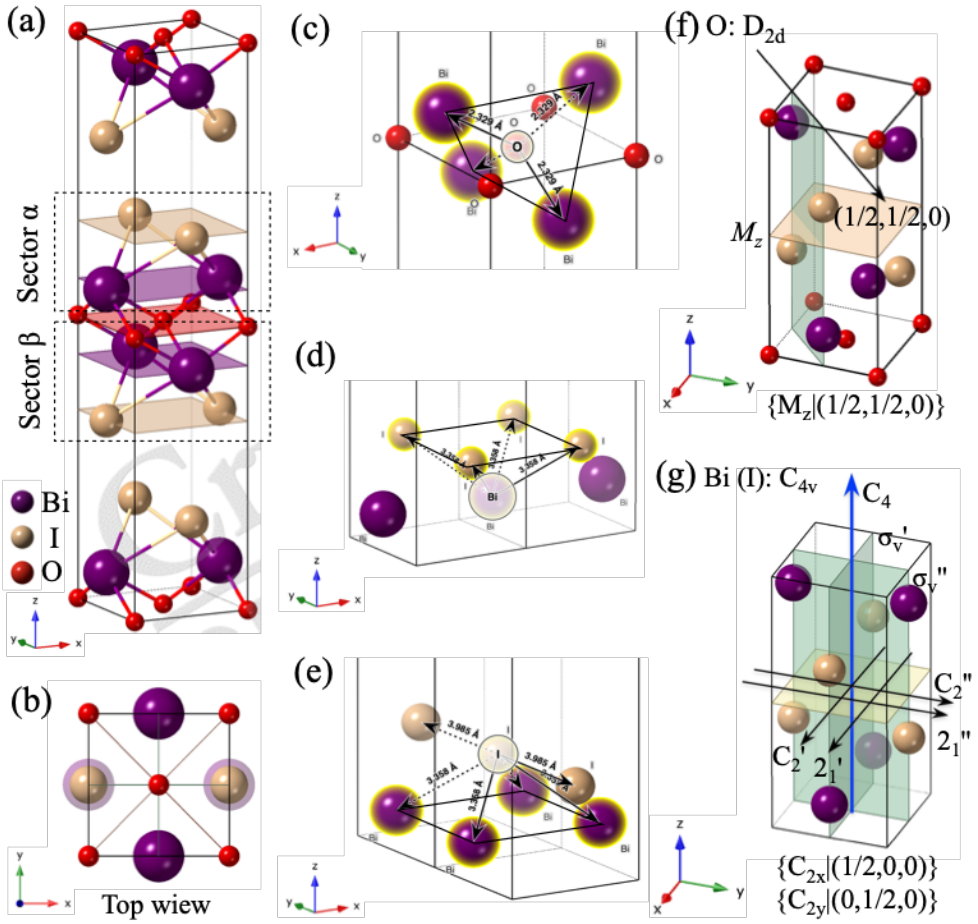

Figure 3.3 Crystal structure and symmetries for BiOI. (a) squint view of BiOI crystal consisted of two packed unit cells along c-axis. (b) Top view of BiOI. (c) O atom and its four nearest Bi atoms neighbors form a tetrahedron, in which the O atom is located at the center. (d) & (e) Bi (I) atom and its four nearest I (Bi) atoms neighbors form a pyramid, of which the Bi (I) occupies the apex. (f) & (g) the nonsymmorphic n-glide $[\{M_z|(1/2,1/2,0)\}]$, 2_1 screw axes $[\{C_{2x}|(1/2,0,0)\}, C_{2y}|(0,1/2,0)\}]$ and other symmorphic symmetries. The locations of the screw axes are shown exactly in (g). Note, in (g) there does not exist a horizontal mirror plane, here the yellow plane is merely used to show the locations of screw axes and rotation axes.

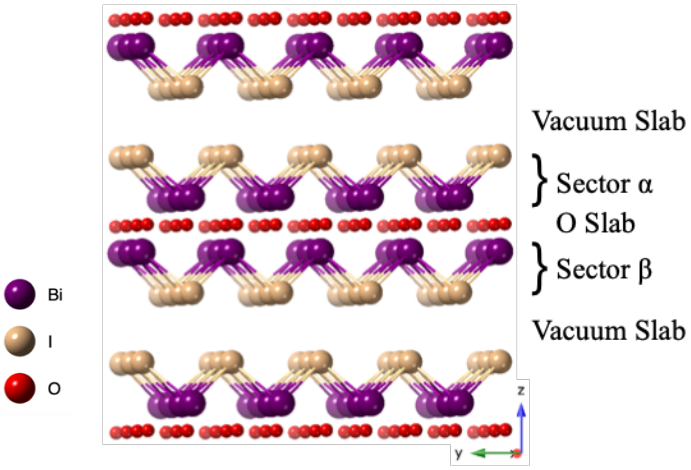

Figure 3.4 The layered structure of BiOI along c-axis. The sector α and its inversion partner sector β are incompactly stacked by a O slab or a vacuum slab that minimizing the compensations between the opposite sectors, such that, the inversion asymmetry (C_{4v}) introduced dipole fields in [BiI] pyramid layers will lead to a net spin polarization located in each sector.

3.3 Electronic Structure of Bismuth Oxyiodide (BiOI)

In this section, prior to show the electronic structure (band dispersion) of BiOI, it is necessary to introduce the theoretical backgrounds for the band structure calculation, including density functional theory (DFT) and tight-binding (TB) model, which will be frequently used in the following discussion. Logically, these two methods will be explained briefly in section 3.3.1, followed by the DFT results of BiOI in sanction 3.3.2 and TB model results in section 3.3.3, followed by a discussion with symmetry analysis of the band degeneracy and splitting in section 3.3.4.

3.3.1 Theories for band calculation

(1) Brief introduction to density functional theory (DFT)

It is a many-body problem for solids band structure calculation, where some important approximations must be considered. Frist, the Hamiltonian for an ideal solid can be written as:

$$\boldsymbol{H} = \sum_{I=1}^{N_I} \frac{\overrightarrow{P_I}^2}{2M_I} + \sum_{i=1}^{N_e} \frac{\overrightarrow{p_e}^2}{2m_e} + \frac{1}{2}\sum_{\substack{I,J \\ I\neq J}} \frac{Z_I Z_J e^2}{\left|\overrightarrow{R_I} - \overrightarrow{R_J}\right|} + \frac{1}{2}\sum_{\substack{i,j \\ i\neq j}} \frac{e^2}{\left|\vec{r_i} - \vec{r_j}\right|} - \frac{1}{2}\sum_{i,I} \frac{Z_I e^2}{\left|\vec{r_i} - \overrightarrow{R_I}\right|} \tag{3.19}$$

$$= T_N + T_e + V_{NN}\left(\vec{R}\right) + V_{ee}(\vec{r}) + V_{Ne}(\vec{r}, \vec{R})$$

where N refers the number of nuclei (subscript I) or electrons (subscript e), $\overrightarrow{P_I}$ momentum for nucleus and $\overrightarrow{p_e}$ momentum for electron, M_I mass for nucleus and m_e mass for electron, $\overrightarrow{R_I}$ coordinate for nucleus and $\vec{r_i}$ coordinate for electron, and Z_I charge for nucleus.

Consequently, the one electron Schrödinger equation reads:

$$\boldsymbol{H}\Phi\left(x, \vec{R}\right) = E\Phi\left(x, \vec{R}\right) \tag{3.20}$$

here, $x \equiv (\vec{r}, s)$ denotes full set of electronic positions and spin variables. Since there is a large difference in the time-scales of nuclei and electrons motion, one can make a ansatz that the wavefunction $\Phi\left(x, \vec{R}\right)$ is separable, i.e., $\Phi\left(x, \vec{R}\right) = \Psi\left(x, \vec{R}\right)\chi(\vec{\mathrm{R}})$ where $\Psi\left(x, \vec{R}\right)$ represents electrons wavefunction and $\chi(\vec{\mathrm{R}})$ means nuclei wavefunction, thus, the Schrodinger equation can be adiabatically decoupled as [138,139]:

$$\boldsymbol{H}_e\Psi_n\left(x, \vec{R}\right) = \left[T_e + V_{ee}(\vec{r}) + V_{Ne}(\vec{r}, \vec{R})\right]\Psi_n\left(x, \vec{R}\right) = \varepsilon_n\Psi_n\left(x, \vec{R}\right) \tag{3.21a}$$

$$\boldsymbol{H}_N\chi_n(\vec{\mathrm{R}}) \approx \left[T_N + V_{NN}\left(\vec{R}\right) + \varepsilon_n\left(\vec{R}\right)\right]\chi_n(\vec{\mathrm{R}}) = \epsilon_n\chi_n(\vec{\mathrm{R}}) \tag{3.21b}$$

here the $\varepsilon\left(\vec{R}\right)$ is the electron eigenvalue depending parametrically on the nuclei positions $\vec{R}$. This assumption is called Born-Oppenheimer approximation or adiabatical approximation. Due to the motion of nuclei is much slower than electrons, one can regard the nuclei as moving in the average potential of the electron gas (ε_n), and if neglecting quantum effects in nuclei dynamics, then the motion of nuclei can be described by classical Newtonian $-\nabla\epsilon(\vec{R}) = dP_I/dt$, hence, the $\epsilon_n = T_N + V_{NN}\left(\vec{R}\right) + \varepsilon_n\left(\vec{R}\right)$.

The next purpose is solving (3.21a). In early quantum chemistry, there is method called Hartree-Fock approximation, where Slater determinant is used to describe the wavefunction and an average effective potential is adopted to replace the $V_{ee}(\vec{r}) + V_{Ne}(\vec{r}, \vec{R})$. That is to say, the many electron wavefunction is represented as $\Psi_n\left(x, \vec{R}\right) = \boldsymbol{\mathcal{A}}[\varphi_1(x_1)\varphi_2(x_2) \ldots \varphi_n(x_n)]$, (here

$\mathcal{A}$ is antisymmetry operator, $\mathcal{A} = \frac{1}{\sqrt{N!}}\sum_P (-1)^P$ with P denoting exchange arrangement in math). By the variational condition $\delta \frac{\langle \Psi_n | \boldsymbol{H}_e | \Psi_n \rangle}{\langle \Psi_n | \Psi_n \rangle} = 0$, one can obtain the Hartree-Fock equation [138,139]:

$$\left[-\frac{\hbar^2}{2m}\nabla^2 + V_{ee}(\vec{r}) + \int d^3x' \frac{\varphi_i(x')\varphi_i^*(x')}{|x - x'|} \right.$$

$$\left. - \sum\nolimits_j \int d^3x' \frac{\left[\varphi_j^*(x')\varphi_i(x')\varphi_i^*(x)\varphi_j(x)\right] / \varphi_i^*(x)\varphi_i(x)}{|x - x'|} \right] \varphi_i(x) \qquad (3.22)$$

$$\equiv \left[-\frac{\hbar^2}{2m}\nabla^2 + V_{HF}(\vec{r}) \right] \varphi_i(x) = \varepsilon_i \varphi_i(x)$$

The difficulty in solving this equation is that the integral terms contain the wave functions $\varphi_i(x)$, $\varphi_j(x)$ to be solved, so it can only be solved iteratively. This approximation (Hartree-Fock self-consistent field approximation) simplifies the many-electron Schrödinger equation to the single-electron effective potential Schrödinger equation. This approximation has considered the electron-electron exchange interaction, but does not consider the repulsive interaction between spin antiparallel electrons, i.e., the electron correlation interaction.

In solid physics, there is another method to solve equation (3.21a), which is the celebrated density functional theory (DFT). The starting point of this theory is based on the Hohenberg-Kohn theorem [139,140]: (1) the ground state energy $\varepsilon_0[n_0(\vec{r})]$ of a many body system is a unique functional of the particle density $n_0(\vec{r}) = \sum_i |\varphi_i(\vec{r})|^2$; (2) the functional $\varepsilon[n(\vec{r})]$ has its minimum relative to variations $\delta n(\vec{r})$ of the particle density at the equilibrium density $n_0(\vec{r})$, i.e., $\delta\varepsilon[n(\vec{r})]/\delta n(\vec{r})\,|_{n(\vec{r})=n_0(\vec{r})} = 0$.

According to the Hohenberg-Kohn theorem, the ground state energy can be obtained by the variation of the energy functional to the density function [139], i.e., $E[n] = T[n] + E_H[n] + E_{xc}[n] + \int V(\vec{r}) n d^3r$, with kinetic energy $T[n]$, electron-electron interaction $E_H[n]$ (Hartree energy), exchange and correlation energies $E_{xc}[n]$ and potential energy $\int V(\vec{r}) n d^3r$. Since one know nothing about the kinetic energy terms $T[n]$ of interacting particles, W. Kohn and L. J. Sham assumed that the kinetic energy functional $T[n]$ can be replaced by a known non-interacting kinetic energy functional $T'^{[n]} = \sum_i \int \varphi_i^*(\vec{r})(-\hbar^2\nabla^2/2m)\varphi_i(\vec{r}) d^3r$ with the

prerequisite that the difference between the two kinetic energy functional must to be included in the exchange correlation item $E_{xc}[n]$, leaving only the $E_{xc}[n]$ item is unknown. Therefore, one can obtain a equation analog to Hartree-Fock equation, which is called Kohn-Sham equation [139]:

$$\left\{-\frac{\hbar^2}{2m}\nabla^2 + V(\vec{r}) + e^2\int\frac{n(\overrightarrow{r'})}{|\overrightarrow{r'}-\vec{r}|}d^3r + \mu_{xc}[n(\vec{r})]\right\}\varphi_i(\vec{r}) = \left[-\frac{\hbar^2}{2m}\nabla^2 + V_{KS}(\vec{r})\right]\varphi_i(\vec{r}) = \varepsilon_i\varphi_i(\vec{r}) \tag{3.23}$$

with $\mu_{xc}[n(\vec{r})] = \delta E_{xc}[n(\vec{r})]/\delta n(\vec{r})$. Corresponding to the effective potential $V_{HF}(\vec{r})$ in the Hartree-Fock equation, here is the Kohn-Sham effective potential $V_{KS}(\vec{r})$. According to the Kohn-Sham theorem, the particle number density function obtained in this way accurately determines the energy and wave function of the ground state of the system, as well as the expected values of various physical quantity operators.

The next work is to solve the Kohn-Sham equation. First, one should choose a basis set. A natural choice for system with periodic boundary condition is the plane waves or the projector augmented waves, because it is easy to pass from real to reciprocal space representation by FFT [139]. The next step is to find an approximate expression for the effective potential term $V_{KS}(\vec{r})$. Here are some frequently used effective potential in early days , such as the Kohn-Sham-Gasper exchange-correlation approximation $V = -2\,(3/\pi)^{1/3}\,[n(\vec{r})]^{1/3}$, the Slater X_α approximation $V = -3\alpha(3/\pi)^{1/3}[n(\vec{r})]^{1/3}$ with $(2/3 \le \alpha \le 1)$, the Wigner-Pines exchange-correlation approximation $V = -0.88\,(2/3r_s + 7.79)/(r_s + 7.79)^2$ with $r_s = -0.88/\varepsilon - 7.79$, Hedin-Lundqvist exchange-correlation approximation $V = -\,(0.045/2)\ln[1 + (21/r_s)]$ with $\varepsilon = -(0.045/2)\{[1 + (r_s/21)^2]ln\ln[1 + (21/r_s)] + r_s/42 - (r_s/21)^2 - 1/3\}$, Ceperley-Alder exchange-correlation approximation $V = -\,0.9164/r_s$ with $\varepsilon = -0.2846/(1 + 1.0529\sqrt{r_s} + 0.3334r_s$ for $r_s \ge 1$ and $\varepsilon = -0.096 + 0.0622lnr_s - 0.0232r_s + 0.004r_s lnr_s$ for $r_s \le 1$.

Nowadays, people have developed many new approximations [139]: (1) the generalized gradient approximation (GGA) [141] $V = \int f[n(\vec{r},\uparrow), n(\vec{r},\downarrow), \nabla n(\vec{r},\uparrow), \nabla n(\vec{r},\downarrow)]$, in which there are many different strategies to determine the function $f[n(\vec{r},\uparrow), n(\vec{r},\downarrow), \nabla n(\vec{r},\uparrow), \nabla n(\vec{r},\downarrow)]$ like the methods of Perdew-Wang (PW), Becke-Perdew (BP), Lee-Yang-Parr (LYP), and Perdew-Burke-Ernzernhof (PBE); (2) Meta-GGA [142], where an additional kinetic energy density of

the electrons is included; (3) Hybrid functionals (HF) [143], where exact exchange and local density energies are hybridized; (4) DFT+U [144], where the on-site Coulomb repulsion is described by the Hubbard Hamiltonian; (5) GW approximation [145], where the full interacting for quasiparticle excitation is calculated by Green's function and dynamical screened Coulomb interaction is described by the W function.

(2) Brief introduction to tight binding (TB) model

From another perspective, consider the formation of energy band by placing isolated atoms on the lattice point of the Bravais lattice. For the convenience of processing, we only discuss the situation where the electron wave functions of neighboring atoms overlap each other very little, that is, the situation where electrons are tightly bound to the atom.

Assuming $\varphi_i(\vec{r})$ is the single electron eigenstate of isolated atom, corresponding to eigenvalue ε_i, illustrated as:

$$\left[-\frac{\hbar^2}{2m}\nabla^2 + V_{atom}(\vec{r})\right]\varphi_i(\vec{r}) = \varepsilon_i\varphi_i(\vec{r}) \tag{3.24}$$

where $V(\vec{r})$ is potential for single atom, i is the index for specific quantum state. The starting point of the tight-binding approximation is to regard the Bloch wave function $[\psi(\vec{r})]$ in the crystal as a linear combination of N degenerate atomic wave functions $[\varphi_i(\vec{r})]$, that is, a linear combination of atomic orbitals (LCAO).

$$\psi(\vec{r}) = \sum_{\vec{R}_m}\frac{1}{\sqrt{N}}e^{i\vec{k}\cdot\vec{R}_m}\varphi_i\left(\vec{r}-\vec{R}_m\right) \tag{3.25}$$

with the assumption that $\int \varphi_i^*\left(\vec{r}-\vec{R}_n\right)\varphi_i\left(\vec{r}-\vec{R}_m\right) = \delta_{nm}$, where $\vec{r}$ is the position of electron in the atom frame and $\vec{R}_n$ is the position of the n-th atom in the lattice frame.

Put the Bloch wave function $[\psi(\vec{r})]$ (3.25) into the crystal Schrödinger equation $\left[-\frac{\hbar^2}{2m}\nabla^2 + V(\vec{r})\right]\psi(\vec{r}) = \varepsilon\psi(\vec{r})$, one gets:

$$\sum_{\vec{R}_m} e^{i\vec{k}\cdot\vec{R}_m}\left[-\frac{\hbar^2}{2m}\nabla^2 + V(\vec{r}) - \varepsilon\right]\varphi_i\left(\vec{r}-\vec{R}_m\right) = 0 \tag{3.26}$$

Replace the kinetic term in (3.26) by (3.24), and left-handed multiply $\varphi_i^*(\vec{r})$ and integrate, one gets:

$$\begin{aligned}\varepsilon_i - \varepsilon + \int \left[V(\vec{r}) - V_{atom}\left(\vec{r} - \vec{R}_m\right)\right] |\varphi_i(\vec{r})|^2 d\vec{r} \\ + \sum_{\vec{R}_m \neq 0} e^{i\vec{k}\cdot\vec{R}_m} \int \varphi_i^*(\vec{r})\left[V(\vec{r}) - V_{atom}\left(\vec{r} - \vec{R}_m\right)\right]\varphi_i\left(\vec{r} - \vec{R}_m\right) d\vec{r} \\ = 0\end{aligned} \tag{3.27}$$

Thus, in simplified notation the eigenvalue $\varepsilon(\vec{k})$ reads:

$$\varepsilon(\vec{k}) = \varepsilon_i - J(0) - \sum_{\vec{R}_m \neq 0} e^{i\vec{k}\cdot\vec{R}_m} J(\vec{R}_m) \tag{3.28}$$

where $\Delta V = V(\vec{r}) - V_{atom}\left(\vec{r} - \vec{R}\right)$ is the potential difference between crystal periodic and atomic potential located at $\vec{R}_m$, $-J(0) = \int [V(\vec{r}) - V_{atom}(\vec{r})]\,|\varphi_i(\vec{r})|^2 d\vec{r}$ is the overlap integral when $\vec{R}_m = 0$, and $-J\left(\vec{R}_m\right) = \int \varphi_i^*(\vec{r})[V(\vec{r}) - V_{atom}(\vec{r})]\varphi_i\left(\vec{r} - \vec{R}_m\right) d\vec{r}$ is the near neighbors overlap integral.

3.3.2 DFT calculation results of BiOI

First-principles calculations were carried out using the Vienna *ab initio* simulation package (VASP) [146] with in the frame work of DFT [147] with the exchange correlation described by the Perdew-Burke-Ernzerhof (PBE) [148] of GGA functional. The electronic structure was treated by projector-augmented wave (PAW) pseudopotential [149] with a planewave-basis cutoff 500 eV. The whole BZ was sampled by a 10×10×6 Γ-centered grid. The experimental lattice constants of $a = b = 3.98$Å, and $c = 9.14$Å were taken while atoms were fully relaxed until the total force on each atom less than 10^{-3} eV/Å and the total energy minimization was performed with a tolerance of 10^{-6} eV. SOC was included in calculations self-consistently. The detail of the DFT calculation is attached in Appendix B.

Figure 3.5 presents the electronic structure of BiOI. The high symmety points and lines ($\Gamma, X, M, Z, R, A, \Delta, \Sigma, \mathrm{Y}, \mathrm{W}, \Lambda, \mathrm{V}, \mathrm{U}, \mathrm{T}, \mathrm{S}$) are shown in Figure 3.5(a). Figure 3.5(b) and (c) show

the DFT calculated band dispersions along high symmetry paths in the absence and presence of SOC, respectively. The k_z dispersions along $\Gamma - Z|X - R|M - A$ paths are shown in Figure 3.5(d). Obviously, due to the layered crystal structure, the k_z dispersion is quite flat. However, the periodic dispersions can still be distinguished, indicating that BiOI is a bulk crystal.

Clearly, the valence band maximum (VBM) is close to the X point, and the bandgap is about 1.3eV. By choosing different doping elements, it offers the possibility to manipulate the electronic structure such that it has the strongest absorption in the visible light range and exhibits the best visible-light photocatalytic activity, which is highly desirable from the viewpoint of the photocatalytic applications [150]. As a typical p-type semiconductor, BiOI can serve as an efficient visible-light photosensitizer for n-type TiO_2 with a large band gap to greatly enhance its photocatalytic efficiency [151].

Another noticeable feature is that at the points X, M, R and A, the glide reflection symmetry $\{M_z|(1/2,1/2,0)\}$ anticommutes with the inversion operator, leading to an extra two-fold degeneracy between two pairs of Kramer's degeneracy, i.e., four-fold degeneracy including the spin, which will be well discussed in section 3.3.4. Such a four-fold degeneracy is maintained along the entire X-M and R-A lines in the absence of SOC (due to the quasi-2D nature of BiOI crystal), as shown in Figure 3.5(f) and (h). Thus, the band splitting along the X-M and R-A lines is caused by SOC solely. In analogy to the conventional Rashba/Dresselhaus effect, such a splitting is composed of two sets of spin splitting bands originating from the sectors α and β, respectively [19]. In comparison, the splitting along the Γ-X and Z-R lines are contributed by both of orbital repulsions and the SOC effect, and are thus larger than those along the X-M and R-A lines, as shown in Figure 3.5(e)~(h).

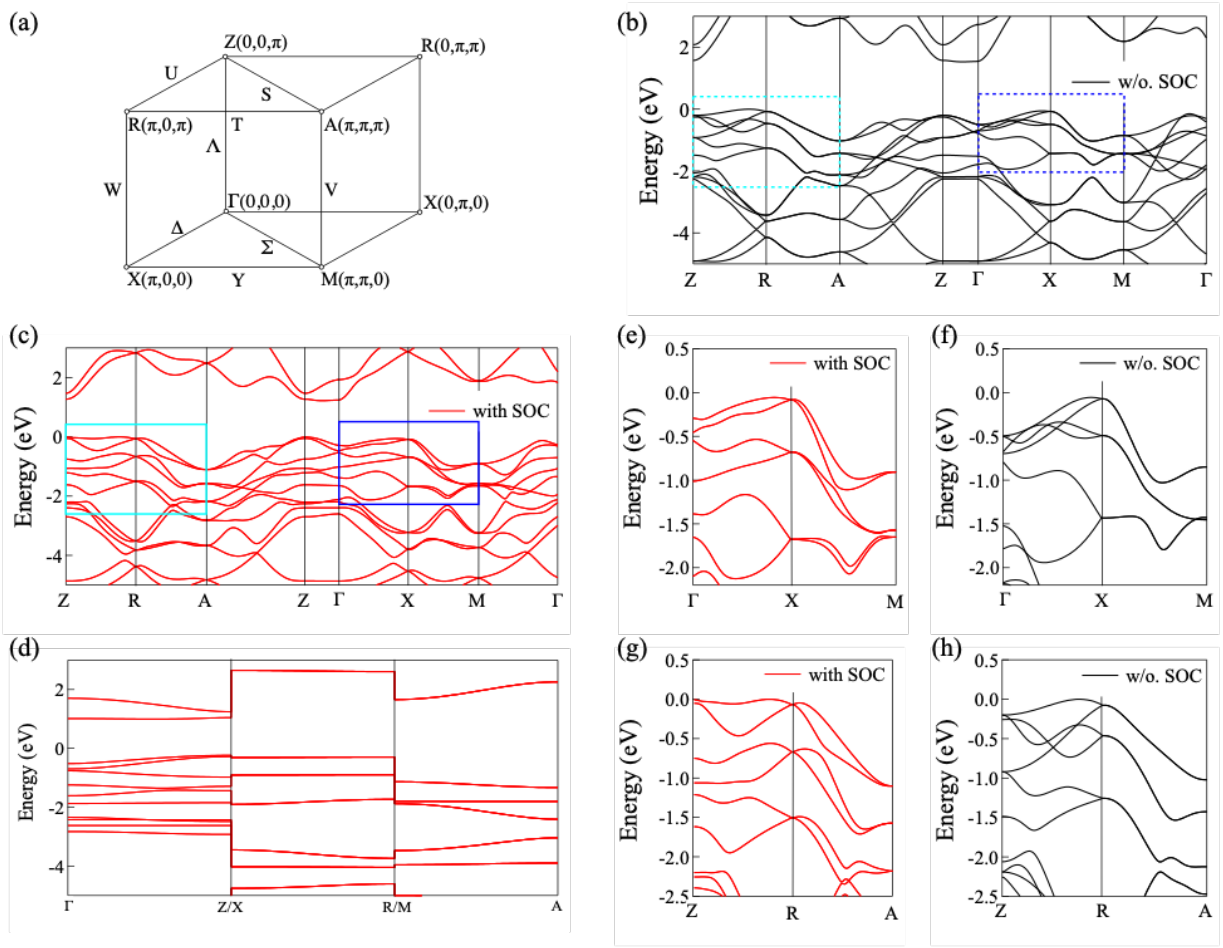

Figure 3.5 Electronic structure of BiOI in the absence and presence of SOC. (a) BZ and high symmetry paths. (b)~(c) electronic structure without and with SOC. (d) band dispersions along k_z paths. (e)~(h) zoom in figures corresponding to rectangles in (c) and (d). It is noticeable that at X, M, R and A points, they are four-fold degenerated including spin, such degeneracies are maintained along X-M and R-A lines when SOC is turn off. Due to the contribution of orbital repulsions and SOC effects, the splitting along Γ-X and Z-R lines are larger than the ones along X-M and R-A lines.

Figure 3.6 shows the orbitals projection with atom resolved. It is obvious that the bottom of conduction bands is mainly contributed by Bi 6 p_z and Bi 6 s orbitals as shown in Figure 3.6(a) and (d). The principal contributors for the top valence bands are I 5 s, I 5 p_z, I 5 p_x and I 5 p_y orbitals. It is noticeable that in the vicinity of the points of Γ and X, the top two valence bands (designated as VB1 and VB2) are mainly composed of the 5 p_x + 5 p_y and 5 s orbitals, while VB3-VB6 are dominated by the 5 p_z and 5 s orbitals. However, in the vicinity of the M point, the top most valence bands (VB1 and VB2) are mainly dominated by the 5 p_z and 5 s orbitals,

whereas for VB3-VB6 bands the 5 p_x + 5 p_y and 5 s orbitals are much more prevailing, as presented in Figure 3.6(b) and (e). As for other lower valence bands like VB7 to VB11, the predominant contributors are O's 2p and 2s orbitals. Same phenomenon also occurs at Z-R-A-Z lines, due to the quasi-2D nature of BiOI system.

Since most of the physical properties are dominated by top of the valence bands, thus, here we focus on the top three pairs of valence bands (VB1-VB6), as mentioned above whose principal contributors are I 5 p_z and I 5 s orbitals that are of great importance for the establishment of the spin textures in the next section 3.4. It is worth emphasizing that the iodine (I) mentioned here is exactly comes from the cleavage surface of the BiOI crystal as described in section 3.2.2.

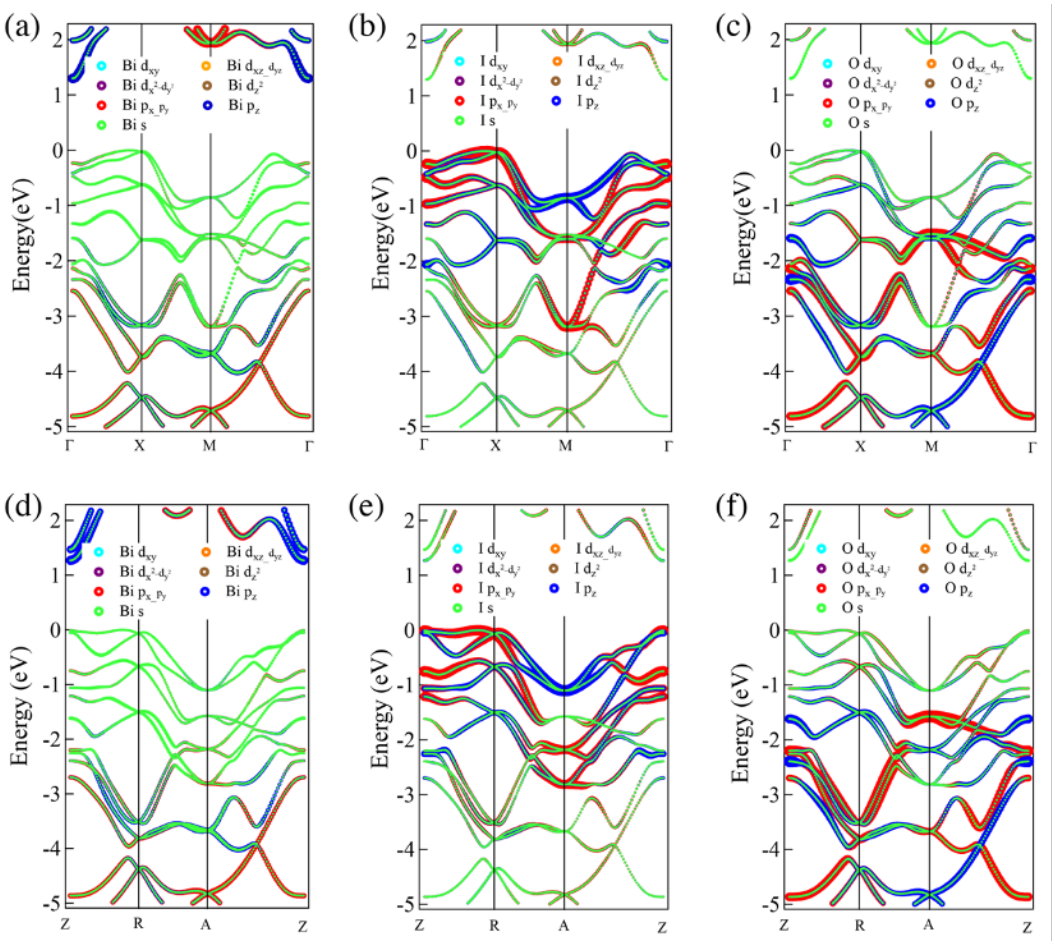

Figure 3.6 Orbital projection of BiOI electronic structure. (a)~(c) shows the projection along Γ-X-M-Γ, and (d)~(f) shows the projection along Z-R-A-Z which presents the same phenomenon as the top row because of the quasi-2D nature of BiOI crystal.

3.3.3 TB model calculation results of BiOI

From previous section, we know that it is four-fold degenerated at the time reversal invariant momenta (TRIM) and two-fold spin degenerated along BZ boundaries by the DFT calculation. To explain the band degeneracy and splitting intuitively, the TB model is helpful to interpretate the degeneracy and splitting.

Considering identical atoms, A and B occupy, respectively, two square lattice points, which has a specific displacement along z-axis and a glide translation along $(x+y)/2$ direction, as shown in Figure 3.7(a). This constructed 2D lattice is applied to simulate the inversion symmetry and nonsymmorphic symmetry in space group $P4/nmm$, and these two square lattices represent sector a and b, respectively. The identical atom A and B can be regarded as iodine atoms because they occupy the same position in $P4/nmm$ space group. For convenience, the lattice constants on the directions of x, y and z are assumed to be 1 in the unit of crystal constants.

In this case the Bloch wavefunction (3.25) of the sectors in this model can be constructed as:

$$\psi_{kn}^{A(B)}(\vec{r}) = \frac{1}{\sqrt{N}} \sum_{\vec{R}_m} e^{i\vec{k}\cdot(\vec{R}_m + \vec{R}_{A(B)})} \varphi_n\left(\vec{r} - \vec{R}_m - \vec{R}_{A(B)}\right) \tag{3.29}$$

where A(B) denotes the two kind of atoms in non-equivalent positions, i.e., in sector a and b; k, n are quantum numbers, adopted to distinguish quantum states in each sector; $\vec{R}_m$ is the position of the unit cell and $\vec{R}_{A(B)}$ is the position of atoms A and B in the frame of refence of unit cell. If choosing the Bloch sums as the basis functions, the wavefunction of this model is a linear combination of the basis:

$$\Psi_{kn}(\vec{r}) = c_{kn}^{A} \psi_{kn}^{A}(\vec{r}) + c_{kn}^{B} \psi_{kn}^{B}(\vec{r}) \tag{3.30}$$

with

$$\left|c_{kn}^{A}\right|^2 + |c_{kn}^{B}|^2 = 1 \tag{3.31}$$

The matrix elements of this model Hamiltonian $\boldsymbol{H} = -\frac{\hbar^2}{2m}\nabla^2 + V(\vec{r})$ can be written as:

$$\begin{aligned} H_{mn}^{AB} &= \left\langle \psi_{km}^{A}(\vec{r}) \middle| \boldsymbol{H} \middle| \psi_{kn}^{B}(\vec{r}) \right\rangle \\ &= \int \sum_{\vec{R}_j} \sum_{\vec{R}_l} \frac{1}{N} e^{i\vec{k}\cdot(\vec{R}_l - \vec{R}_j + \vec{R}_B - \vec{R}_A)} \varphi_m^*\left(\vec{r} - \vec{R}_j - \vec{R}_A\right) \boldsymbol{H} \varphi_n\left(\vec{r} - \vec{R}_l - \vec{R}_B\right) d\vec{r} \end{aligned} \tag{3.32}$$

$$= \sum_{\vec{R}_l} e^{i\vec{k}\cdot(\vec{R}_l-\vec{R}_j+\vec{R}_B-\vec{R}_A)} \int \varphi_m^*(\vec{r}-\vec{R}_j-\vec{R}_A)\boldsymbol{H}\varphi_n(\vec{r}-\vec{R}_l-\vec{R}_B)d\vec{r}$$

$$= \sum_{\vec{R}_l} e^{i\vec{k}\cdot(\vec{R}_l-\vec{R}_j+\vec{R}_B-\vec{R}_A)}\, t_{mn}^{jl,AB}$$

where $t_{mn}^{jl,AB} = \int \varphi_m^*(\vec{r}-\vec{R}_j-\vec{R}_A)\boldsymbol{H}\varphi_n(\vec{r}-\vec{R}_l-\vec{R}_B)d\vec{r}$ is parameter describing the hopping between two different atoms with the quantum states of $\varphi_m(\vec{r}-\vec{R}_j-\vec{R}_A)$ and $\varphi_n(\vec{r}-\vec{R}_l-\vec{R}_B)$, located at positions of $\vec{R}_j+\vec{R}_A$ and $\vec{R}_l+\vec{R}_B$, respectively. This integral is a three-center integral, whose calculation is very difficult. However, if we adopt the Slater-Koster approximation [152,153], in which the integral is approximated to a two center integral, and can be expressed as a function of radial integral ($V_{mn\alpha}$). For instance, the nearest hopping between p_x and p_y orbitals can be expressed as $lm(V_{pp\sigma}-V_{pp\pi})$, where l, m and n are direction cosines of the vector from one atom to another nearest atom. The hopping parameters between s and p_x, p_y, p_z orbitals are shown in Table 3.3. More details on the Slater-Koster approximation and its hopping parameters are presented in Appendix C.

Table 3.3 The hopping parameters t_{mn} between s (s) and p_x, p_y, p_z (x,y,z) orbitals can be approximately expressed as radical integrals $V_{mn\alpha}$, which scale with the vector $\vec{d}$. The direction cosines are defined as $l=\vec{d}\cdot\vec{x}/d$, $m=\vec{d}\cdot\vec{y}/d$, $n=\vec{d}\cdot\vec{z}/d$ [19].

t_{ss}	$V_{ss\sigma}$	t_{xx}	$l^2V_{pp\sigma}+(1-l^2)V_{pp\pi}$
t_{sx}	$V_{sp\sigma}$	t_{xy}	$lm(V_{pp\sigma}-V_{pp\pi})$
t_{xs}	$-lV_{sp\sigma}$	t_{yz}	$mn(V_{pp\sigma}-V_{pp\pi})$

The matrix elements $H_{mn}^{AB}=\sum_{\vec{R}_l} e^{i\vec{k}\cdot(\vec{R}_l-\vec{R}_j+\vec{R}_B-\vec{R}_A)}\, t_{mn}^{jl,AB}$ can be applied to multi-orbital case if one set the quantum number m,n representing different orbitals, or single orbital if m,n representing only one orbital per atom. This is a universal expression of Hamiltonian in the frame of TB model.

In our case, one atom A have four nearest neighbor atoms B and four next nearest neighbors A, as shown in Figure 3.7(b). The relative position vectors $\vec{R}_l - \vec{R}_j + \vec{R}_B - \vec{R}_A$ are hence denoted as d_{11}, d_{12}, d_{13}, d_{14} for the nearest neighbors and d_{21}, d_{22}, d_{23}, d_{24} for the next nearest neighbors. Correspondingly, the hopping parameters $t_{mn}^{jl,AB}$ are denominated as t_{mn}^{11}, t_{mn}^{12}, t_{mn}^{13}, t_{mn}^{14} (t_{mn}^{21}, t_{mn}^{22}, t_{mn}^{23}, t_{mn}^{24}) for nearest (next nearest) neighbors. It is noticeable that $t_{mn}^{11} = t_{mn}^{12} = t_{mn}^{13} = t_{mn}^{14}$ and $t_{mn}^{21} = t_{mn}^{22} = t_{mn}^{23} = t_{mn}^{24}$ are equivalent due to the symmetries in this crystal structure. If we consider only one orbital for each atom, then, the hopping parameters can be rewritten in the following form:

$$H_{jl} = \sum_{l} e^{i\vec{k}\cdot\vec{d}_{jl}}\, t^{jl} \tag{3.33}$$

For example, the matrix element of $H_{A_1B_l}$ (nearest hopping) can be expressed as: $H_{A_1B_l} = e^{i\vec{k}\cdot\vec{d}_{11}}t^{11} + e^{i\vec{k}\cdot\vec{d}_{12}}t^{12} + e^{i\vec{k}\cdot\vec{d}_{13}}t^{13} + e^{i\vec{k}\cdot\vec{d}_{14}}t^{14} = t_1\left(e^{i\vec{k}\cdot\vec{d}_{11}} + e^{i\vec{k}\cdot\vec{d}_{12}} + e^{i\vec{k}\cdot\vec{d}_{13}} + e^{i\vec{k}\cdot\vec{d}_{14}}\right) = t_1\left(e^{i\left(\frac{k_x}{2}+\frac{k_y}{2}\right)} + e^{i\left(-\frac{k_x}{2}+\frac{k_y}{2}\right)} + e^{-i\left(\frac{k_x}{2}+\frac{k_y}{2}\right)} + e^{i\left(\frac{k_x}{2}-\frac{k_y}{2}\right)}\right) = t_1 cos\frac{k_x}{2} cos\frac{k_y}{2}$. In the same way, the matrix element of $H_{A_1A_l}$ (next nearest hopping) is $t_2\left(e^{ik_x} + e^{ik_y} + e^{-ik_x} + e^{-ik_y}\right) = t_2(cosk_x + cosk_y)$. Note the constants are absorbed into t_1 and t_2 respectively. Therefore, the Hamiltonian of this TB model can be written as:

$$H = \begin{bmatrix} H_{A_1A_l} & H_{A_1B_l} \\ H_{B_1A_l} & H_{A_lA_1} \end{bmatrix} = \begin{bmatrix} t_2(cosk_x + cosk_y) & t_1 cos\frac{k_x}{2} cos\frac{k_y}{2} \\ t_1 cos\frac{k_x}{2} cos\frac{k_y}{2} & t_2(cosk_x + cosk_y) \end{bmatrix} \tag{3.34}$$

$$= t_1 cos\frac{k_x}{2} cos\frac{k_y}{2}\tau_x + t_2\left(cosk_x + cosk_y\right)\tau_0$$

where $\tau_x = \begin{bmatrix} 0 & 1 \\ 1 & 0 \end{bmatrix}$ and $\tau_0 = \begin{bmatrix} 1 & 0 \\ 0 & 1 \end{bmatrix}$.

The next is to take the SOC term into account. An electron hopping from the atom A to its for next near neighbors will fell an effective field originating from the local asymmetry. Considering the original SOC term $-\frac{\hbar}{4m_0^2c^2}\boldsymbol{\sigma}\cdot(\boldsymbol{p}\times\nabla V)$ in (3.6), in which the $\boldsymbol{p}\times\nabla V$ represents an effective magnetic field perpendicular to the in-plane lattice. Here, if we use another vector with the same direction to represent this effective magnetic field, thus, the SOC term can be written as $-\eta\boldsymbol{\sigma}\cdot$

$(\vec{d}_{1j} \times \vec{d}_{1l})$ where the other parameters are all absorbed in η and $\vec{d}_{1j}, \vec{d}_{1l}$ are position vectors along the two nearest bonds connecting the next nearest neighbors $\vec{d}_{2j}$ shown in Figure 3.7(c) [19]. To obtain the SOC term in reciprocal space, in this case, we should sum over the four next nearest neighbors' SOC effects and transform the real space vector $\vec{d}_{1j} \times \vec{d}_{1l}$ in reciprocal space. First, the vector $\vec{d}_{1j} \times \vec{d}_{1l}$ in reciprocal space should be:

$$\begin{aligned}\vec{d}_{1j} \times \vec{d}_{1l} = &\left[\vec{d}_{14} \times \left(-\vec{d}_{13}\right) + \left(-\vec{d}_{12}\right) \times \vec{d}_{11}\right] e^{i\vec{k}\cdot\vec{d}_{21}} \\ &+\left[\vec{d}_{11} \times \left(-\vec{d}_{14}\right) + \left(-\vec{d}_{13}\right) \times \vec{d}_{12}\right] e^{i\vec{k}\cdot\vec{d}_{22}} \\ &+\left[\vec{d}_{12} \times \left(-\vec{d}_{11}\right) + \left(-\vec{d}_{14}\right) \times \vec{d}_{13}\right] e^{i\vec{k}\cdot\vec{d}_{23}} \\ &+\left[\vec{d}_{13} \times \left(-\vec{d}_{12}\right) + \left(-\vec{d}_{11}\right) \times \vec{d}_{14}\right] e^{i\vec{k}\cdot\vec{d}_{24}}\end{aligned} \tag{3.35a}$$

Considering the symmetries, the Fourier term of $\left[\vec{d}_{12} \times \left(-\vec{d}_{11}\right) + \left(-\vec{d}_{14}\right) \times \vec{d}_{13}\right] = -\left[\vec{d}_{13} \times \left(-\vec{d}_{12}\right) + \left(-\vec{d}_{11}\right) \times \vec{d}_{14}\right] \equiv \vec{\xi}_1$, meanwhile the term of $\left[\vec{d}_{14} \times \left(-\vec{d}_{13}\right) + \left(-\vec{d}_{12}\right) \times \vec{d}_{11}\right] = -\left[\vec{d}_{12} \times \left(-\vec{d}_{11}\right) + \left(-\vec{d}_{14}\right) \times \vec{d}_{13}\right] \equiv \vec{\xi}_2$. Therefore, the (3.35) equals to:

$$\begin{aligned}\vec{d}_{1j} \times \vec{d}_{1l} &= -\vec{\xi}_1\left(e^{i\vec{k}\cdot\vec{d}_{24}} - e^{i\vec{k}\cdot\vec{d}_{22}}\right) + \vec{\xi}_2\left(e^{i\vec{k}\cdot\vec{d}_{21}} - e^{i\vec{k}\cdot\vec{d}_{23}}\right) \\ &= -\vec{\xi}_1\left(2isink_y\right) + \vec{\xi}_2\left(2isink_x\right) \\ &\equiv \left(-sink_y, sink_x\right)\vec{\xi}\end{aligned} \tag{3.35b}$$

Then the SOC term can be rewritten as:

$$-\eta\boldsymbol{\sigma} \cdot \left(\vec{d}_{1j} \times \vec{d}_{1l}\right) = \lambda_R\left(\sigma_y sink_x - \sigma_x sink_y\right) \tag{3.36}$$

where $\tau_z = \begin{bmatrix}1 & 0\\ 0 & -1\end{bmatrix}$ shares the same direction with $\vec{\xi}$, λ_R is the Rashba strength. Combining equation (3.34), thus, we obtain the single orbital TB Hamiltonian as:

$$H = t_1 cos\frac{k_x}{2} cos\frac{k_y}{2}\tau_x \otimes \sigma_0 + t_2\left(cosk_x + cosk_y\right)\tau_0 \otimes \sigma_0 + \lambda_R \tau_z \otimes \left(\sigma_y sink_x - \sigma_x sink_y\right) \tag{3.37}$$

in which the first (second) term describes the nearest (next nearest) neighbor hopping, while the third term depicts Rashba SOC induced by local polar fields; $t_1(t_2)$ is the inter-sector or nearest (intra-sector or next nearest) electron hopping that contributes to the diagonal (off-diagonal) terms in this Hamiltonian on the basis of $\{|\alpha\uparrow\rangle, |\alpha\downarrow\rangle, |\beta\uparrow\rangle, |\beta\downarrow\rangle\}$ and thus the τ and σ are the Pauli matrices under the basis of $\{|\alpha\rangle, |\beta\rangle\}$ and $\{|\uparrow\rangle, |\downarrow\rangle\}$, respectively.

Next we solve the secular equation of this single orbital TB Hamiltonian. First, the Hamiltonian reads:

$$\begin{bmatrix} t_2\left(cosk_x + cosk_y\right) & -\lambda_R\left(isink_x + sink_y\right) & t_1 cos\frac{k_x}{2} cos\frac{k_y}{2}\tau_x & 0 \\ \lambda_R\left(isink_x - sink_y\right) & t_2\left(cosk_x + cosk_y\right) & 0 & t_1 cos\frac{k_x}{2} cos\frac{k_y}{2}\tau_x \\ t_1 cos\frac{k_x}{2} cos\frac{k_y}{2}\tau_x & 0 & t_2\left(cosk_x + cosk_y\right) & \lambda_R\left(isink_x + sink_y\right) \\ 0 & t_1 cos\frac{k_x}{2} cos\frac{k_y}{2}\tau_x & \lambda_R\left(-isink_x + sink_y\right) & t_2\left(cosk_x + cosk_y\right) \end{bmatrix}$$
$$\equiv \begin{bmatrix} N & -D & M & 0 \\ -D^* & N & 0 & M \\ M & 0 & N & D \\ 0 & M & D^* & N \end{bmatrix} \tag{3.38}$$

where $M = t_1 cos\frac{k_x}{2} cos\frac{k_y}{2}$, $N = t_2\left(cosk_x + cosk_y\right)$, $D = \lambda_R\left(isink_x + sink_y\right)$. Then, by diagonalizing the determinant $|H - EI|$ (I is a 4×4 identity matrix), we can get the eigenvalues to be:

$$E_{1,2} = N - \sqrt{(M^2 + DD^*)} \equiv N - U \tag{3.39a}$$

$$E_{3,4} = N + \sqrt{(M^2 + DD^*)} \equiv N + U \tag{3.39b}$$

with four corresponding orthogonal eigenvectors:

$$\Psi_1 = \frac{1}{\sqrt{2}}\begin{pmatrix} 1 \\ D^*/U \\ -M/U \\ 0 \end{pmatrix}, \Psi_2 = \frac{1}{\sqrt{2}}\begin{pmatrix} 0 \\ -M/U \\ -D/U \\ 0 \end{pmatrix}, \Psi_3 = \frac{1}{\sqrt{2}}\begin{pmatrix} 1 \\ -D^*/U \\ M/U \\ 0 \end{pmatrix}, \Psi_4 = \frac{1}{\sqrt{2}}\begin{pmatrix} 1 \\ M/U \\ D/U \\ 0 \end{pmatrix} \quad (3.40)$$

The corresponding band dispersions for top three pairs of the valence bands drawn based on equation (3.39) with SOC turn on ($\lambda_R/t_1 = -0.2$) and off ($\lambda_R = 0$) is depicted in Figure 3.7(c). Evidently, the TB model shows similar results as DFT calculations that (i) it is four-fold degenerated at TRIM, and (ii) two-fold degenerated along BZ boundaries with the presence of SOC, and (iii) the band gaps are larger along BZ center to boundaries than the one along BZ boundaries. These results are difficult to understand from DFT calculations, however, much easier by TB model. The $E(\vec{k}) - \vec{k}$ dispersions of the TB model are given by $E(\vec{k}) = N \pm U = N \pm \sqrt{\left(t_1 cos\frac{k_x}{2} cos\frac{k_y}{2}\right)^2 + \lambda_R^2\left(\left(sink_y\right)^2 - (sink_x)^2\right)}$. For example, (i) at the TRIM of $X(\pi, 0)$ and $M(\pi, \pi)$, the corresponding eigenvalues are $E(X) = E(M) = N$, which states the four-fold degeneracy (spin included) at TRIM; while (ii) along BZ boundaries, the eigenvalues are $E(Z) = N \pm \lambda_R sink_y$ $(0 < k_y < \pi)$, which responsible for the two-fold degeneracy (spin included) and the explanation for the band splitting only regulated by SOC (λ_R) along Z directions; (iii) along Δ directions, the eigenvalues are $E(\Delta) = N \pm \lambda_R\sqrt{\left(\frac{t_1}{\lambda_R}\right)^2\left(\cos\frac{k_x}{2}\right)^2 + (cosk_x)^2 - 1}$ $(0 < k_x < \pi)$, which gives an explanation of the two-fold degeneracy (spin included) and a large band splitting due to both SOC (λ_R) and orbitals repulsion (t_1), as for Σ directions, the eigenvalues are $E(\Sigma) = N \pm t_1\left(cos\frac{k_y}{2}\right)^2$, $(0 < k_x < \pi)$, which reveals that the two-fold band splitting is fully controlled by the orbitals repulsion (t_1).

To explain the degree of wavefunction segregation (DWS) between different sectors, we adopted a quantity named sector polarization as illustrated in equation (3.15). Here the wavefunction projected onto sector α or β can be illustrated as $\rho_n^{\alpha/\beta} = \sum_{i\in\alpha/\beta}\langle\Psi_n(\vec{k})|i\rangle\langle i|\Psi_n(\vec{k})\rangle$ and the sector polarization reads $P_n^{sec}(\vec{k}) = \left(\rho_n^{\alpha} - \rho_n^{\beta}\right)/\left(\rho_n^{\alpha} + \rho_n^{\beta}\right)$ depicted in Figure 3.7(d). Note that in choosing $\Psi_n(\vec{k})$, if two eigenstates are degenerate, any linear combination of the two states is also an eigenstate of the system. Therefore, $P_n^{sec}(\vec{k})$ is gauge variant for a single branch of doubly degenerate bands, depending on the unitary transformation of basis [19].

The index $P_n^{sec}(\vec{k})$ of sector polarization for the lowest doubly degenerate bands $\{E_1(\vec{k}), E_2(\vec{k})\}$ and corresponding eigenstates $\{\Psi_1(\vec{k}), \Psi_2(\vec{k})\}$ with different splitting strengths $(t_1/\lambda_R)^{-1}$are shown in Figure 3.7(d). It manifests that along the BZ boundaries X–M (Z lines), $P_n^{sec}(\vec{k})$ stabilizes at its maximum value ± 1, indicating a vanishing hopping effect (compensatory interference) guaranteeing a fully wavefunction segregation onto the real sectors α and β. In sharp contrast, the $P_n^{sec}(\vec{k})$ at Γ points is exactly zero, stating the wavefunctions are entangled completely. These observations can be well understood by the TB Hamiltonian, in which the off-diagonal matrix elements in the 2×2 block matrix are contributed solely by the first term of equation (3.37) (i.e., M). At the BZ boundary, the $M = t_1 cos\frac{k_x}{2} cos\frac{k_y}{2} = 0$ vanishes, and the Hamiltonian is thus the direct sum of two matrices separately exerted on two subspaces spanned by two sectors:

$$H = \begin{bmatrix} N & -D & & \\ -D^* & N & & \mathcal{O} \\ & & N & D \\ & \mathcal{O} & D^* & N \end{bmatrix} = \begin{bmatrix} M_\alpha & \mathcal{O} \\ \mathcal{O} & M_\beta \end{bmatrix} = M_\alpha \oplus M_\beta \tag{3.41}$$

Therefore, the two eigenstates $\{\Psi_\alpha(\vec{k}), \Psi_\beta(\vec{k})\}$ are naturally chosen to be in either sector α or β, resulting in a maximum $P_n^{sec}(\vec{k})$ in the diagonalized block matrix. In the language of group theory that two bands with different subgroup representations do not hybridize when they meet each other, leading to a degenerate band-crossing point. In either case, the representation space of this special point can be spanned as a direct sum of two subspaces from the two crossing bands [19].

On the other hand, when the wavevector travels from BZ boundaries to Γ points, the off-diagonal terms of TB Hamiltonian become more and more predominant, leading to descending $P_n^{sec}(\vec{k})$ with the electron density finally distributed equally in sectors α and β at Γ points. Note that if we do not consider any symmetry requirements but just separate the two sectors very far away from each other, the off-diagonal terms of equation (3.40) also vanish because of the negligible hopping parameter t_1, which accounts for the strategy to insert thick slab between the opposite sectors to minimize the interaction. However, such a strategy is just a trivial method preventing the wavefunctions overlap of two individual inversion-asymmetric systems in k-space and is not helpful for practical material design.

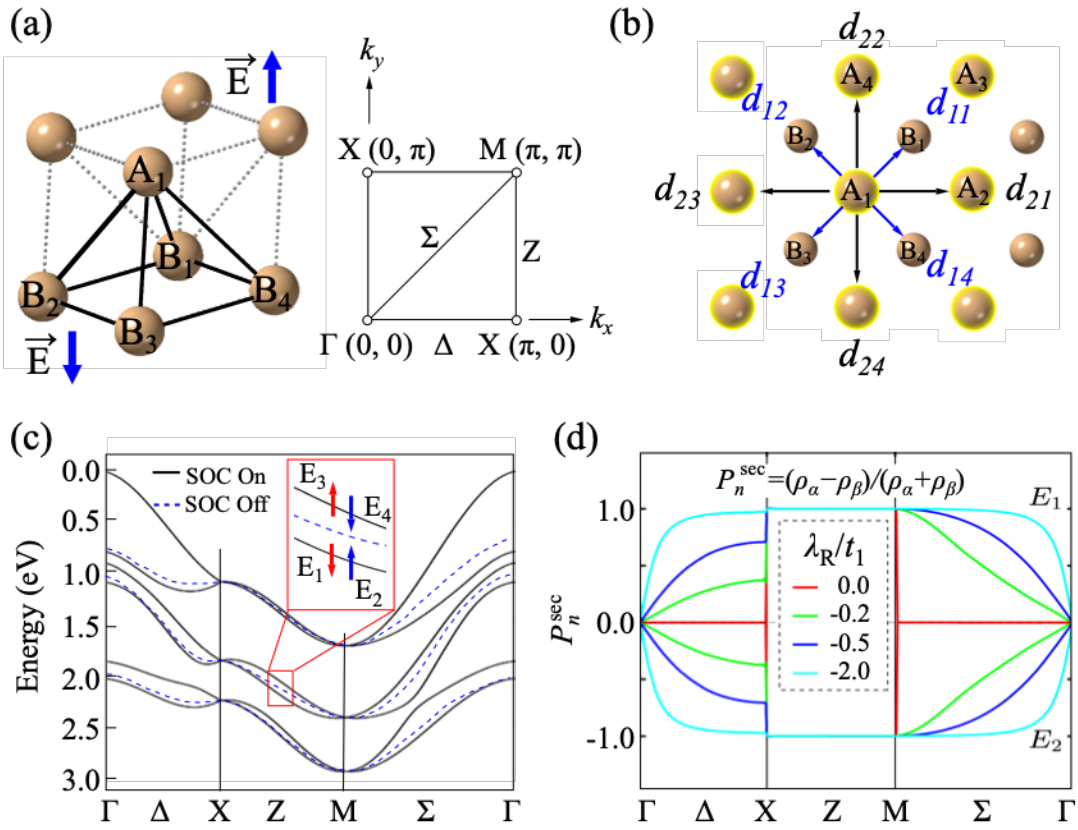

Figure 3.7 Crystal structure and corresponding band structure of TB model. (a) unit cell consists of two square sublattices with glide and screw symmetries (left side), and high symmetric paths in 2D BZ (right side). (b) overview of the sublattices and its nearest (next nearest) distances. (c) band dispersions along high symmetric paths drawn based on TB model. The black solid lines represent the SOC is turn on while blue dash lines represent the SOC is off, and the red rectangle is a zoom in of the picked bands. Note the solid lines are all doubly degenerated because off spin degeneracy, and the dash lies are all four-fold degeneracy. (d) the sector polarization, which is an index to quantitatively depict the degree of wavefunction segregation.

3.3.4 Symmetry analysis of the band structure

In the DFT calculations and TB model, we have obtained a series of important results, such as degeneracy and splitting of energy bands. However, we should further carefully analyze the roles of symmetry on the band dispersion. Even in the TB model, the symmetry is hidden in the constructed crystal model, thus hidden in the parameters M, N, and D, making it not obvious. In

this section, we will systematically analyze the contribution of symmetries to the degeneracy of energy bands, especially nonsymmorphic symmetries (glide planes and screw axes), of which the irreducible representations are only two dimensional. Consequently, the eigenvalues in these invariant subspaces are doubly degenerate (spin excluded).

Prior to analyze the symmetry effects on band degeneracy, it is benefit to recall that: (i) In a crystal the effect of the point group operator P_R acting on a function $f(\vec{r})$ is defined to be $P_R f(\vec{r}) = f(R^{-1}\vec{r})$, where R is a orthogonal transformation in real space $\left(R\vec{r} = \overrightarrow{r'}\right)$. (ii) The operator R transforms a Bloch function $\psi_k(\vec{r}) = e^{i\vec{k}\cdot\vec{r}}\mu_k(\vec{r})$ into a new function $\psi_{k'}(\vec{r})$, where k' is derived from k by a rotation R applied in the k space, i.e., $P_R\psi_k(\vec{r}) = \psi_k(R^{-1}\vec{r}) = e^{i\vec{k}\cdot R^{-1}\vec{r}}\mu_k(R^{-1}\vec{r}) = e^{i\vec{k}\cdot\overrightarrow{r'}}\mu_k\left(\overrightarrow{r'}\right) = e^{i\overrightarrow{k'}\cdot\vec{r}}\mu_{k'}(\vec{r}) = \psi_{Rk}(\vec{r}) = \psi_{k'}(\vec{r})$, which can be noted as $\vec{k}\cdot R^{-1}\vec{r} = R\vec{k}\cdot\vec{r}$. (iii) It is well known that if P_R commute with H ($[P_R, H] = 0$) and $\psi_k(\vec{r})$ is a solution to the Schrodinger equation, then the $P_R\psi_k(\vec{r})$ is also a solution to the Schrodinger equation with the same energy. These three relations will play an important role in our following symmetry discussion.

Now, let us consider the 2D BZ shown in Figure 3.7(a). The space group of the TB model have mirror planes m perpendicular to the a-axis at $x = a/4$ and $3a/4$, and a glide plane g parallel to the a-axis. First, we discuss the glide-plane effect at the time reversal invariant X points. If $\psi_k(\vec{r}) = \psi_X(x, y)$ is a solution for the Schrodinger equation at $\vec{k} = \pi/a$ denoted as X in BZ, the symmetry operations act on the wavefunction $\psi_X(x, y)$ are listed below.

The glide operation g implies that:

$$g\psi_X(x, y) = \psi_X(g^{-1}x, g^{-1}y) = \psi_X(x + \tfrac{a}{2}, -y) \tag{3.42}$$

The space inversion operator i enforces:

$$i\psi_X(x, y) = \psi_X(i^{-1}x, i^{-1}y) = \psi_X(-x, -y) \tag{3.43}$$

The mirror plane m at $x = a/4$ manifests:

$$m\psi_X(x, y) = \psi_X(m^{-1}x, m^{-1}y) = \psi_X(-x + \tfrac{a}{2}, y) \tag{3.44}$$

Then it is obvious that g commutes to mi:

$$g\psi_X(x, y) = mi\psi_X(x, y) \text{ or } [g, mi] = 0 \tag{3.45}$$

It is much easier to proof the degeneracy at the X points. Suppose that the representation of the glide operation is pure one-dimensional, since $i^2\psi_X(x,y) = \psi_X(x,y)$, it is straightforward that the representation of i is ± 1, i.e., $i\psi_X(x,y) = \pm\psi_X(x,y)$. Meanwhile, due to $m^2\psi_X(x,y) = \psi_X(x,y)$, it would follow that $m\psi_X(x,y) = \pm\psi_X(x,y)$ [154]. By (3.42), it is apparent to obtain the representation of g^2:

$$g^2\psi_X(x,y) = mimi\psi_X(x,y) = (\pm 1)^2(\pm 1)^2\psi_X(x,y) = \psi_X(x,y) \tag{3.46}$$

However, on the other hand, if one considers the coordinates transformation and the representation of translation operation, it follows:

$$\begin{aligned} g^2\psi_X(x,y) = g\psi_X\left(x+\frac{a}{2},-y\right) &= \psi_X(x+a,y) \\ &= e^{ik_x a}\psi_X(x,y) \\ = e^{i\pi}\psi_X(x,y) &= -\psi_X(x,y) \end{aligned} \tag{3.47}$$

which contradicts (3.46). Therefore, the assumption that the representation of X points cannot be one-dimensional. That is to say the bands must degenerate at the X points. Since the states of $\psi_X(x,y)$ and $g\psi_X(x,y)$ must be degenerate, whose eigenvalues must be the same because the Hamiltonian is invariant under the operations g. Actually, it is much easier to find that the irreducible representation at the X points (C_{4v}) is two-dimensional from any group theory textbook [136]. Therefore, eigenstates in this invariant subspace are doubly degenerate.

Now, we continue to proof that the irreducible representation is two-dimensional along the $M-X$ line (Z direction). In the same way with proof by contradiction. Let T be the time reversal operator, we know that in the absence of spin:

$$T\psi_Z(x,y) = \psi_{-Z}(x,y) \tag{3.48}$$

On the boundary $\vec{k}_Z = \left(\frac{\pi}{a},y\right)$ it must follow:

$$-\vec{k}_Z = \left(-\frac{\pi}{a},-k_y\right) = \left(\frac{\pi}{a},-k_y\right) \tag{3.49}$$

Thus, from (3.45) and assuming the state along Z direction to be nondegenerate, thus:

$$gT\psi_z(x,y) = mi\psi_{-Z}(x,y) = m\psi_z(x,y) = \psi_z(x,y) \tag{3.50}$$

where in the last step we have used the relation of $\vec{k} \cdot R^{-1}\vec{r} = R\vec{k} \cdot \vec{r}$, i.e., $m_x^{-1}\left(\frac{\pi}{a}, k_y\right) = \left(\frac{\pi}{a}, k_y\right)$, rather than letting m_x directly act on the coordinates as in (3.47).

However, since $[g, T] = 0$, thus one can obtain:

$$gTgT\psi_Z(x, y) = g^2\psi_Z(x, y) = -\psi_Z(x, y) \tag{3.51}$$

where in the last step we have used the argument of (3.47). This result (3.51) contradicts (3.50). So, the $\psi_Z(x, y)$ and $gT\psi_Z(x, y)$ must be independent states, but their eigenvalues must be the same because the Hamiltonian is invariant under the operations gT. Therefore, the bands must stick on the zone boundary line Z. Similarly, if one check any group textbook, it easy to find that the Z lines' irreducible representation is two-dimensional, indicating the bands along Z directions are two-fold degenerate.

We now consider the electron spin effect to the band structure. Adding the spin without turning on the SOC simply doubles the degeneracy of every state [154], i.e., the states at TRIM and along BZ boundaries should be four-fold degenerate. But the SOC will lift some of the degeneracy. For example, due to the SOC the band dispersions along the $M - X$ direction is only two-fold degenerate while at TRIM they maintain four-fold degenerate which is well discussed in the TB model. Another shortcut way is to consult the double-group representations of these high symmetric points or directions in any group theory textbook.

3.4 Spin Textures of Bismuth Oxyiodide (BiOI)

In the previous section, we have shown that the valence bands along the BZ boundaries are double-degenerate, and each branch consists of sectors α and β respectively. Furthermore, the spin polarization on the sector, or the degree of wavefunction segregation (DWS) shows that the wave functions are completely separated on the BZ boundaries, implying nearly perfect spin polarization in centrosymmetric crystal, i.e., HSP effect. This can be can also be understood by the local effective magnetic fields, shown in Figure 3.8, where panel (a) shows the position of the cross section that corresponding to the charge density in panel (b) local potential in panel (c) and effective magnetic fields in panel (d).

It can be seen from panel (b) that the charge density with glide symmetry is highly localized at the centers of the squares within the iodine layers, forming potential wells depicted in panel

(c). By taking the gradient of the potentials one can obtain the effective magnetic fields $\boldsymbol{B}_{eff} \approx \boldsymbol{p} \times \nabla V$ perpendicular to sector α and β as shown in panel (d). The effective magnetic fields emerge in the SOC term as $-\frac{\hbar}{4m_0^2c^2}\boldsymbol{\sigma} \cdot (\boldsymbol{p} \times \nabla V)$.

It can also be seen that the charge density of the opposite sectors does not show strong overlap, revealing the wavefunctions are well separated, indicating that there should be a very weak interaction between the opposite sectors, so that the spin polarizations are highly localized at each individual sectors.

In this section, the HSP effect calculated by DFT will be illustrated in section 3.4.1 in which the orbitals projection onto one single sector is also included, while the TB model results are presented in section 3.4.2.

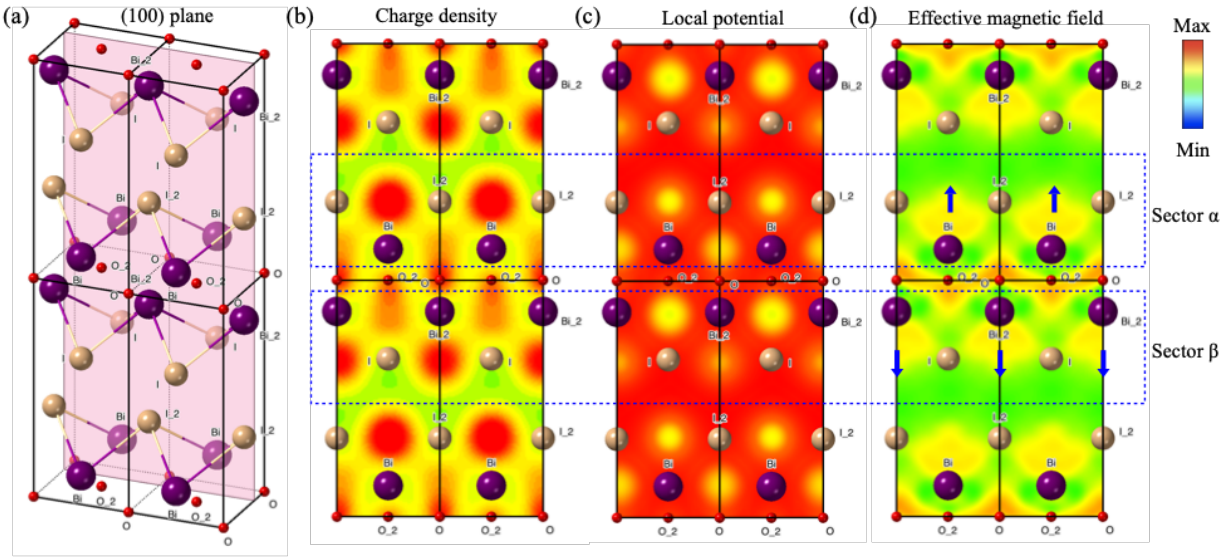

Figure 3.8 Illustration for the effective magnetic fields of BiOI in $1 \times 2 \times 2$ unit cells. (a) the cross section locates at the center of the pyramid of [BiI] along (100) plane. (b), (c) and (d) represents charge density, potentials, and magnetic fields respectively, whose position corresponds to panel (a).

3.4.1 DFT calculation for hidden spin polarization in bismuth oxyiodide (BiOI)

Prior to presenting the DFT results of HSP effects, we should emphasize two points that (i) each branches of the valence bands are doubly degenerated composing of sector α and β, shown in Figure 3.9(a) rather than restating Figure 3.5 where it did not manifest the spin degeneracy

intuitively; and (ii) the total orbital contribution (the sum of atoms Bi, O and I) to the valence bands is depicted in Figure 3.9(b) and with VB1 and VB2 as representatives, the weighted atomic orbitals is shown in Figure 3.9(c) & (d). In the next section, we will project the spin textures of each valence bands onto individual sector and we will also discuss the orbital-resolved spin textures. More details about the orbital occupancy for VB3 to VB6 please refer Appendix D.

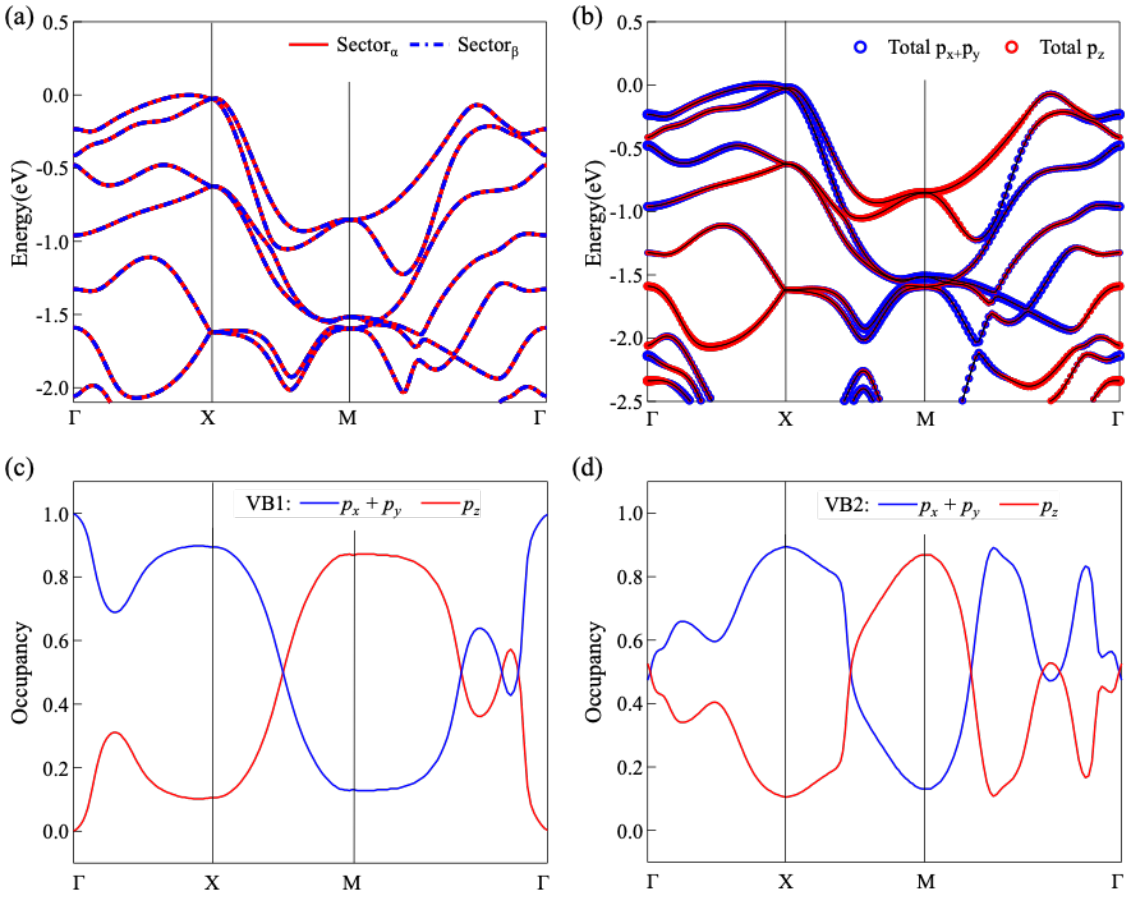

Figure 3.9 Sector resolved (a) and orbital resolved (b) band dispersions of top three pairs of valence bands of BIOI. (c) & (d) the weighted atomic orbitals ($p_x + p_y, p_z$) occupancy for VB1 and VB2, respectively.

The HSP calculation was evaluated by projecting each Bloch wavefunction $|\psi_n(k)\rangle$ $(n = 1,2)$ of two-fold degenerate states onto the spin ($\boldsymbol{s}_\eta$) and atomic orbital basis $|\phi_{klm\sigma}\rangle_j^\tau$, $(\sigma = \uparrow, \downarrow; \tau = \alpha, \beta)$ of each atomic site (j) of sector α or β, finding the mean value of spin operators ($\boldsymbol{S}_{\eta lm\sigma j}^\tau =$

$\boldsymbol{s}_\eta \otimes |\phi_{klm\sigma}\rangle_{jj}^{\tau\tau}\langle\phi_{klm\sigma}|$) under these projected wavefunctions, and finally summing results of $\langle\psi_n(k)|\boldsymbol{S}_{\eta lm\sigma j}^{\tau}|\psi_n(k)\rangle$ for a given spin direction (η) and sector (τ) that contains a number of atomic sites in one unit cell. The Wigner–Seitz radii for constructing $|\phi_{klm\sigma}\rangle_j^{\tau}$ used in this study are listed in the pseudopotentials of the VASP simulation package [141]. Finally, the HSP effects can be written in the following form:

$$S_{\eta lm\sigma j}^{\tau}(k) = \sum_{n=1}^{2}\langle\psi_n(k)|\boldsymbol{s}_\eta \otimes |\phi_{klm\sigma}\rangle_{jj}^{\tau\tau}\langle\phi_{klm\sigma}|\psi_n(k)\rangle \tag{3.52}$$

It is notable that in the degenerate states the set of wavefunctions $|\psi_n(k)\rangle$ ($n = 1,2$) can transform to another basis set by unitary transformation. However, as a trace-like physical quantity, HSP is invariant under such unitary transformation, which ensure the feasibility of measuring and detecting (please refer Appendix E for the proof of this gauge invariant).

Figure 3.10 shows the spin textures of three representative valence bands VB1, VB3 and VB5 of BiOI, as for the complete spin textures of the VB1 to VB6 please refer Appendix F. The corresponding spin texture, projected onto the real space sectors α and β, forming the inversion partners, are shown as brown and cyan arrows in the 3D $E(\vec{k}) - k_x - k_y$ space (panels (a) (b), and (c)) and red and blue arrows in the 2D $k_x - k_y$ space (panels (d), (e) and (f)). They manifest two branches of spin polarization (indicated in Figure 3.10(a), (b) and (c) by brown and cyan arrows) dominated by the two opposite [BiI] real-space sectors shown in Figure 3.3(a) and Figure 3.4.

It is straightforward to see that (i) the spin polarizations, from the two inversion-symmetric [BiI] layers, have opposite directions and compensate each other completely in the whole BZ, as a result of the constraint of the centrosymmetry. This phenomena is thus called spin-layer locking; (ii) there are both helical (in the vicinity of *M* points) and non-helical (adjacent to *X* points) spin textures for each individual sector, suggesting that there are Rashba SOC terms ($\sigma_x k_y - \sigma_y k_x$) deriving from the SIA at the *M* points, and Dresselhaus SOC terms ($\sigma_x k_x - \sigma_y k_y$) originating from the BIA at the *X* points, meanwhile, it also confirms that the R-2 effect is accompanied by the D-2 effect; (iii) the calculated spin polarization (polarized spin vectors) localized on a specific [BiI] layer is highly polarized along the BZ boundary but almost vanishes around the zone center, confirming that the HSP effect is generally compensated by inversion partners near the Γ point

but immune from the hopping effect around the boundary of the BZ due to its nonsymmorphic crystal structure. This k-dependent spin polarization is routinely called spin-momentum locking. Therefore, in the case of our BiOI, the spin polarization is thus spin-momentum-layer locking.

Another notable feature is that the out-of-plane polarization is very weak, which does not exceed 20% due to the layered structure, shown in Figure 3.10(d), (e) and (f) as the color scheme. This result reveals that it still exhibits spin flipping with respect to X points, after all, this is only quasi-two-dimensional structure.

The spin textures of p orbitals projected onto sector α are shown in Figure 3.10(g), (h) and (i) where the red, blue, and green arrows represent the projection of p_x, p_y and p_z orbitals. In the case of VB1, it manifests that the spin texture at X points is manly dominated by the in-plane orbitals p_x and p_y while at M points it is manly contributed by p_z orbitals, agree well with the weighted atomic orbitals ($p_x + p_y, p_z$) occupancy for VB1.

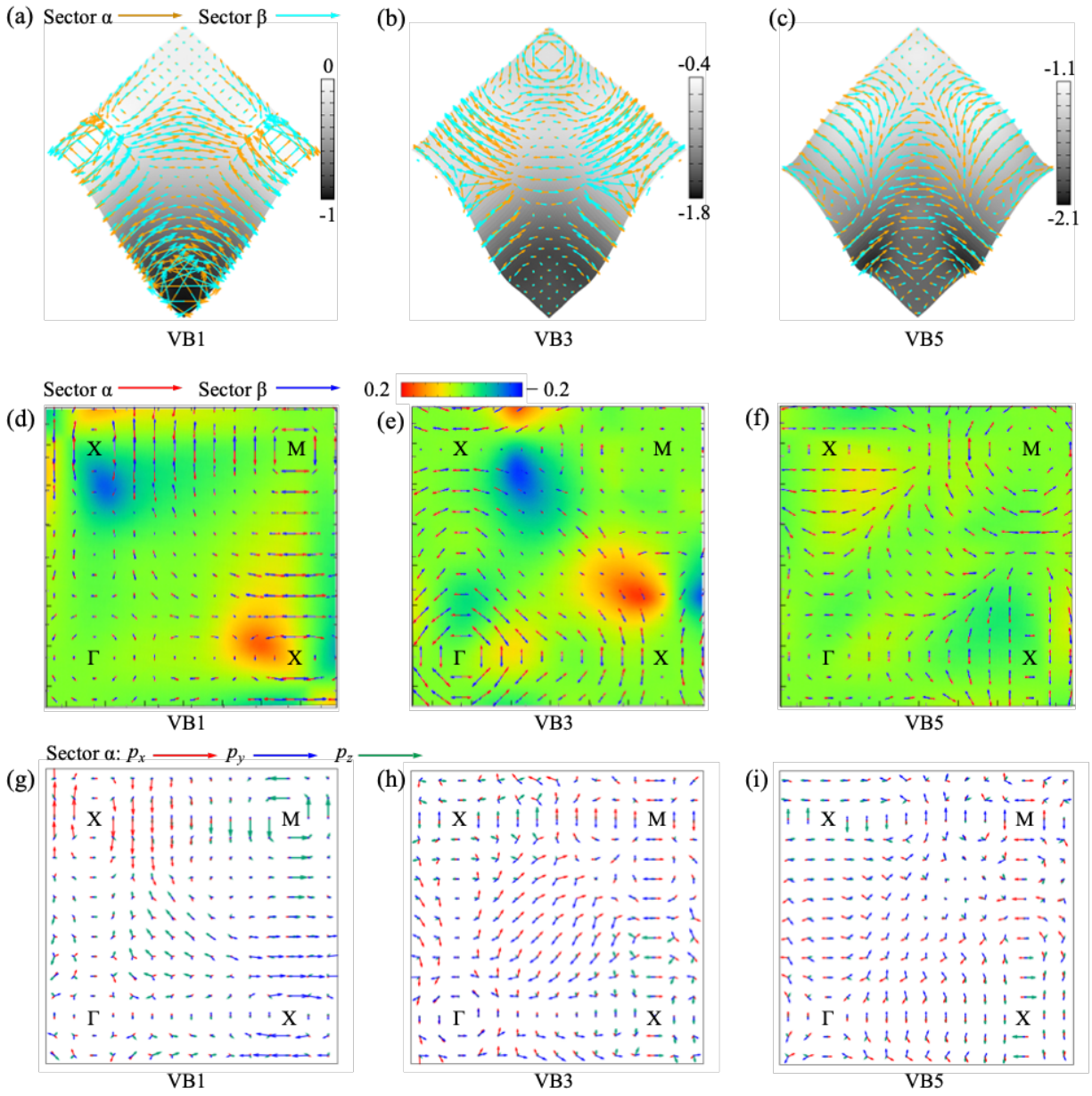

Figure 3.10 DFT calculated spin textures of BiOI. (a), (b) and (c) 3D valence bands with spin vectors for VB1, VB2 and VB3. (d), (e) and (f) projected 2D spin textures for VB1, VB2 and VB3. (g), (h) and (i) orbital resolved spin textures projected onto sector α for VB1, VB2 and VB3.

3.4.2 TB calculation for hidden spin polarization in bismuth oxyiodide (BiOI)

The TB calculation for HSP of each sector (such as sector α) was performed by taking the mean value of the spin operators ($\boldsymbol{S}^{\tau}_{\eta lm\sigma j} = \boldsymbol{s}_{\eta} \otimes |\phi_{klm\sigma}\rangle^{\tau\tau}_{jj}\langle\phi_{klm\sigma}|$) with single orbital (such as p_z), which can be written as follow:

$$S^{\alpha}_{\eta \boldsymbol{z}}(k) = \sum_{n=1}^{2} \langle\psi_n(k)|\boldsymbol{s}_{\eta} \otimes p_z\rangle^{\alpha\alpha}_{jj}\langle p_z|\psi_n(k)\rangle \tag{3.53}$$

Note that the p_z orbital including s, p_x, p_y orbitals can be written as a linear combination of the four eigenstates of the model Hamiltonian.

Figure 3.11 shows the spin textures calculated by TB model Hamiltonian, in which the row (a) represents the spin textures projected on sector α and β indicated by red and blue arrows respectively, and row (b) represents the orbital resolved spin textures projected onto the sector α with red, blue, and green arrows stand for the contribution of p_x, p_y and p_z orbitals. These results generally agree with the DFT results that (i) the spin textures of sector α and β are fully compensated as shown by the opposite spin vectors; (ii) there are helical and non-helical spin textures at M and X points, confirming the existence of the Rashba and Dresselhaus spin splitting; (iii) the magnitude of the spin polarization along BZ boundary is much larger than that at BZ center, excepting VB5. This is because in the model Hamiltonian we only took two identical atoms A and B of one element (such as iodine) into consideration. Actually, in the DFT calculation for atomic orbital weighted band dispersions shown in Figure 3.6, one can see that the lower valence band has the larger contribution from oxygen orbitals. However, it does not make a strong affect to the top valence bands because these band are mainly dominated by the iodine's p orbitals.

Even though the model Hamiltonian are largely simplified, it can covey many important physics, such as the four-fold degeneracy at TRIM, two-fold degeneracy along BZ boundary, SOC induced band splitting along M-X direction, larger band gaps along M-X directions than that along Γ-X directions, opposite spin directions for sector α and β, helical and non-helical spin textures at X and M points, and the spin is highly polarized along the BZ boundary, while the same effect almost vanishes around the zone center. All these physics can be attributed to the nonsymmorphic crystal structure.

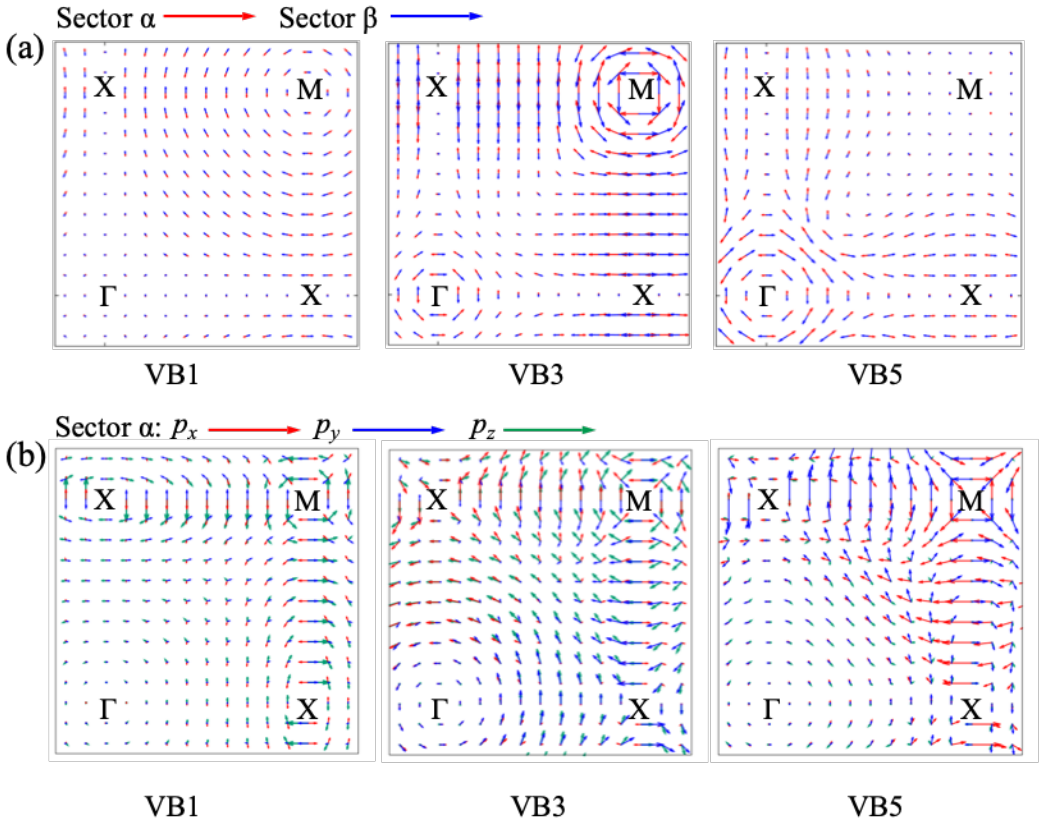

Figure 3.11 Spin textures calculated by model Hamiltonian. (a) sector resolved spin textures for VB1, VB3 and VB5. (b) orbital resolved spin textures of sector α for VB1, VB3 and VB5.

Chapter 4 High Resolution ARPES Study of the Band Structure of BiOI

In this chapter we will introduce the experimental results. First, we will briefly introduce the sample preparation and characterization, which will be arranged in section 4.1, then the photon energy dependent experiment to reveal its k_z dispersion will be introduced in section 4.2, and finally, the ARPES results on in plane band dispersions will be fully explained in section 4.3.

4.1 Sample Preparation and Characterization

The BiOI single crystal used in this work was synthesized by chemical vapor transport (CVT) method [155] with BiI_3 as the transport agent [156,157]. The Bi_2O_3 (Innochem, 99%) and BiI_3 (Alfa, 99%) powder were placed in an alumina crucible with a molar ratio of Bi_2O_3: BiI_3=1: 1. The crucible was sealed in a quartz tube under argon environment. The tube was then flame-sealed under dynamic vacuum and placed inside a two-zone furnace. The crystals were grown over a period of 9 days with a temperature gradient from 973 K to 833 K. Finally, millimetre-size single crystals were obtained and characterized by low-energy-electron-diffraction (LEED) and powder X-ray diffraction (XRD) shown in Figure 4.1.

Figure 4.1(a) shows the *in-situ* cleaved fresh surface of single crystal BiOI, with a flat surface revealing the merit of the layered structure. Figure 4.1(b) shows the LEED pattern measured at beam energy of 130.2 eV. Figure 4.1(c) presents the powder XRD patterns. For the powder XRD measurement, a number of BiOI single crystals were ground into powder in a mortar, where a little silica powder was added as an abrasive to improve the powder effect. The peaks of Si can be observed in the XRD patterns which is distinguished by the blue color. It can be seen that the peaks for BiOI agree well with the one of theoretical calculation. The clear LEED pattern and accurate XRD peaks undoubtedly confirm that the prepared BiOI is of high quality.

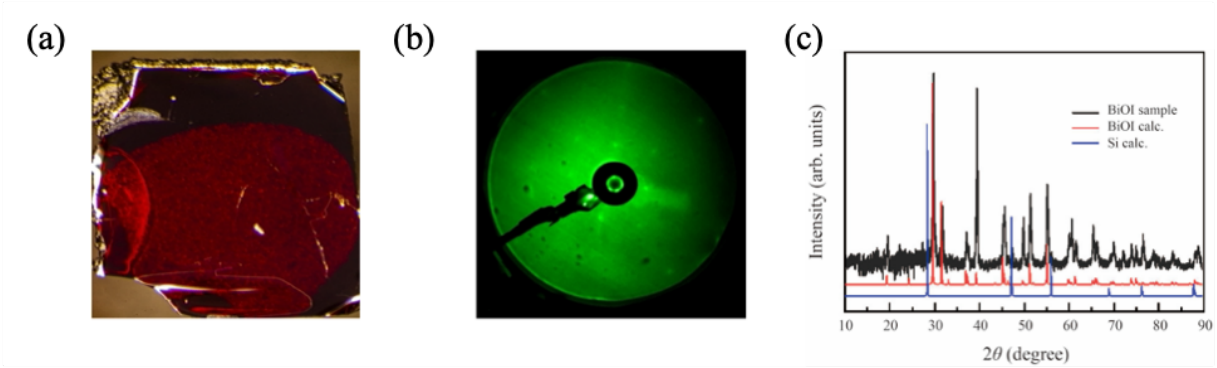

Figure 4.1 Crystal structure characterizations of BiOI. (a) in-situ cleaved surface. (b) LEED pattern measured at beam energy of 130.2 eV. (c) powder XRD peaks of BiOI with Si as abrasive powder.

Prior to the band dispersion measurements, we made a survey measurement over a wide energy range to observe some outer core levels using photon energy of 99 eV at 30K. In Figure 4.2(a), the angle-integrated photoemission spectrum exhibits I 4d and Bi 5d orbitals. The lower two panels, Figs. 4.2(b) and 4.2(c) respectively show I 4d and Bi 5d core-level spectra fitted using two voigt functions. In Figure 4.2(b), the binding energies (peak positions) of I $4d_{3/2}$ and I $4d_{5/2}$ are 51.14 eV and 49.42 eV, respectively. The peak width is a full width at half maximum (FWHM) of 0.5 eV, and the peak separation due to the spin-orbit interaction is 1.72 eV. Meanwhile, in Figure 4.2(c) the binding energies of Bi $5d_{3/2}$ and Bi $5d_{5/2}$ are 29.44 eV and 26.44 eV. The peak width is about 0.44 eV (FWHM) and the peak separation is 3 eV. These binding energies are consistent with theoretical calculations of single crystal of iodine and bismuth [158,159]. Another important feature is that it does not show appreciable surface-bulk peak separation in these core-level spectra. All these results further confirm that the measured BiOI is of high purity and quality.

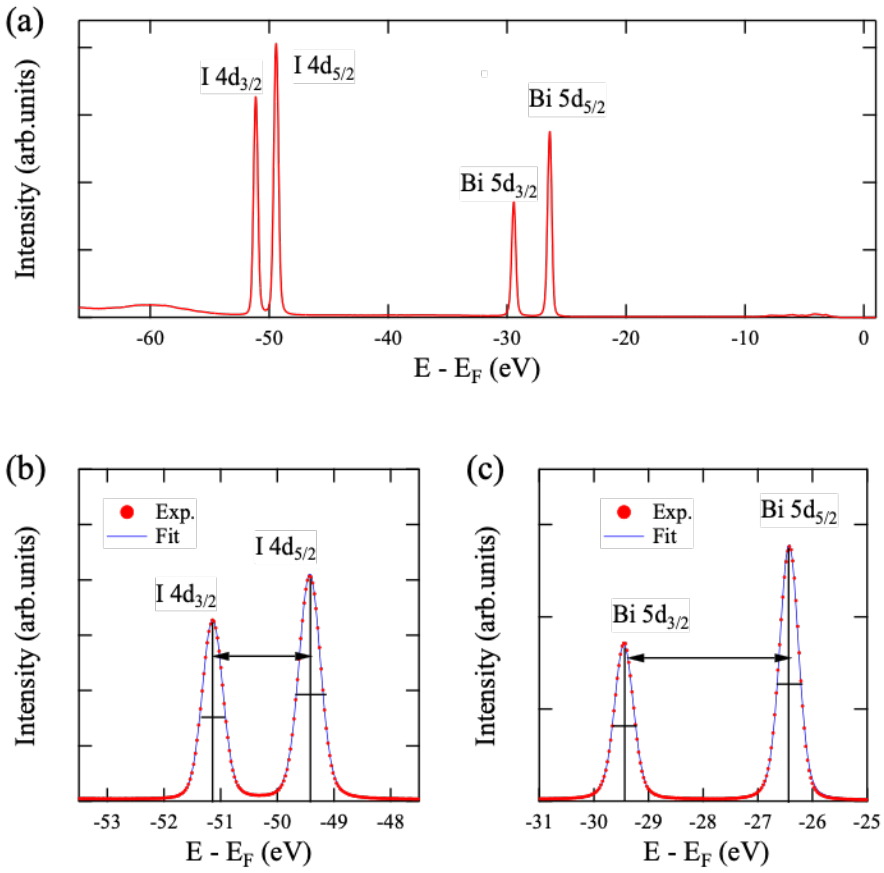

Figure 4.2 Angle-integrated photoemission spectrum of BiOI. (a) A wide energy survey taken at 30K and photon energy of 99 eV. Peaks simulation with voigt function to show the iodine's 4d orbital intensity (b) and bismuth 5d orbitals intensity (c).

4.2 ARPES Study of the Electronic Structure of BiOI

In this section, we will analyze the electronic structure of the centrosymmetric BiOI in detail based on our high resolution ARPES results. First, we need to locate accurate high symmetry points and lines, so we did k_z (section 4.2.1) and CEC (section 4.2.2) experiments, and then we specifically analyzed the band dispersion along M-X direction (section 4.2.3) and Γ-X direction (section 4.2.4) with the comparison to our theoretical calculations.

4.2.1 ARPES study of the kz dispersion with variable photoenergies

Since BiOI crystalizes in a quasi-2D manner as illustrated in section 3.2, its k_z dispersion is fairly flat which was presented in section 3.3. However, it still presents a finite k_z dependence especially along Γ-Z direction as illustrated in Figure 3.5(d). To experimentally evaluate the k_z position along the Γ-Z direction, we need to estimate the inner potential using a formula $k_\perp = \frac{1}{\hbar}\sqrt{2m(E_k + V_0)}$ which was described in section 2.3. In our case, based on the finite k_z dispersion as detected by changing photon energy together with the lattice parameter *c*, the inner potential was experimentally evaluated to be about 9 eV.

Figure 4.3 shows the constant energy contour (CEC) on the $k_x - k_z$ plane with binding energy of 4.82 eV. It can be seen from this figure that there indeed exists periodic structure. Even so, its k_z dependent band dispersion is small due to its quasi 2D layered structure. Figure 4.4 shows the ARPES intensity maps along the A-R-A and R-Z-R lines measured under the photoenergy of 76 eV and the M-X-M and X-Γ-X lines measured under the photoenergy of 65 eV, which was experimentally determined from the Figure 4.3. The corresponding DFT results are overlaid on the ARPES image plots. One can see good agreements between the ARPES and DFT results. Moreover, the band dispersions along A-R-A and R-Z-R lines show very similar dispersions as the ones along the M-X-M and X-Γ-X lines, which further confirms that BiOI is a quasi 2D material.

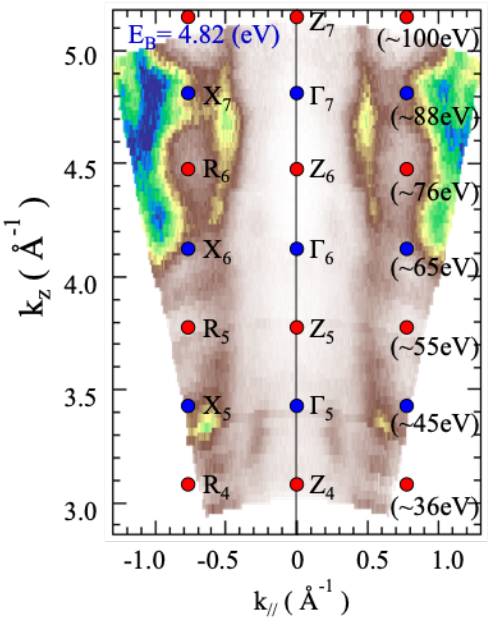

Figure 4.3 Photon energy dependent measurement reveals the inertial periodic dispersion along Γ-Z direction.

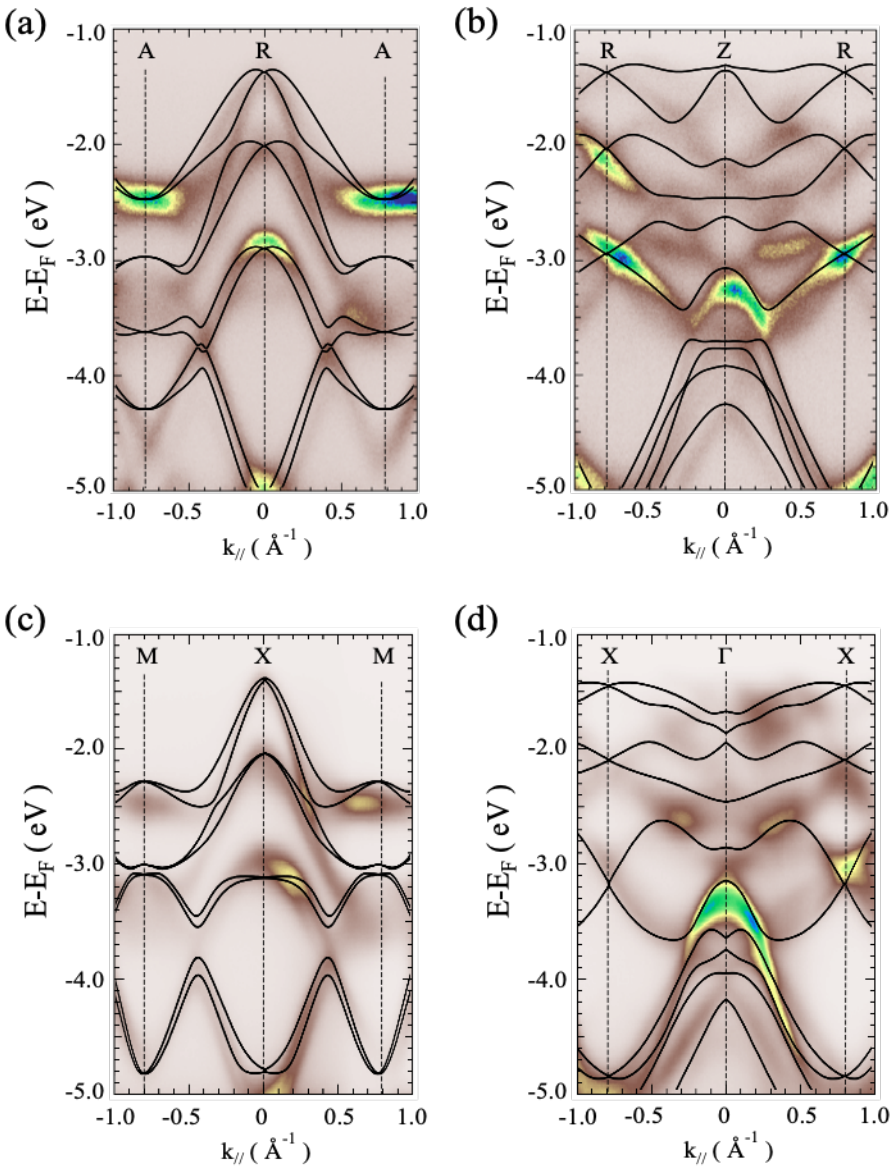

Figure 4.4 DFT bands (black solid lines) overlaid on ARPES image plots, where (a) shows the A-R-A bands, (b) shows the R-Z-R bands, (c) shows the M-X-M bands and (d) shows the X- Γ-X bands.

4.2.2 ARPES study of the constant energy contours of BiOI

After determining the k_z dispersion, it is thus easy for us to measure the constant energy contours (CECs) of the Γ-X-M plane. Figure 4.5 shows the experiment measured and DFT calculated CECs for VB1 and VB2, in which the CECs were measured under the photon energy

of 65 eV corresponding to Γ_6 in Figure 4.3. It can be seen from Figure 4.5(a) that a square-like CEC exists at around -1.3 eV, whose corners are on the lines connecting next nearest X points. As the energy is lowered, the CEC centered at the X point is expanded like ellipse and eventually forms contours like bowknot surrounding the M point merging with the CEC centered at the Γ point, which agrees well with the DFT calculated CECs of VB1 and VB2. These CEC maps provide us with an overview of the top valence bands, which is beneficial for us to locate the high symmetry paths.

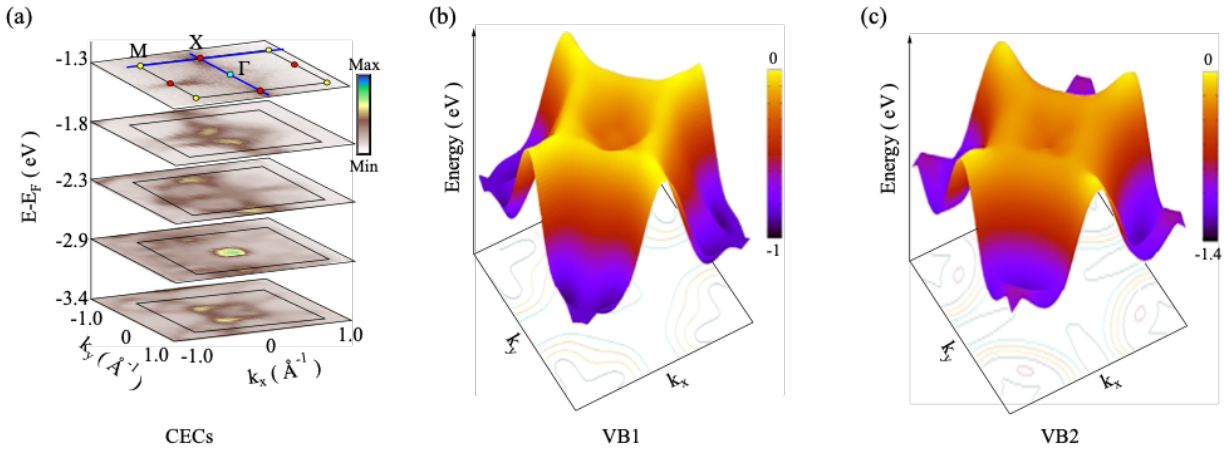

Figure 4.5 Experiment measured (a) and DFT calculated CECs of VB1 (b) and VB2(c) under the photoenergy of 65eV.

4.2.3 ARPES study of the band dispersion along M-X direction

In our pervious theoretical discussion, we predicated that that (i) it is four-fold degenerated at TRIM, and (ii) two-fold degenerated along BZ boundaries with the presence of the SOC, and (iii) the band gaps are larger along the BZ center to boundaries than the one along BZ boundaries. Here, by our high resolution ARPES, we experimentally revealed these features, which is illustrated in Figure 4.6 in which the band dispersion along M-X direction is measured under the photoenergy of 65eV.

Figure 4.6 panel (a) shows a large energy range from -1 eV to -7.5 eV of the bands along the M-X direction, and panel (b) shows the zoom in bands corresponding to the rectangle in panel (a) with a overlay of our previous DFT calculation, and panel (c) is the corresponding high

contrast bands after taking second differential using panel (b), and panel (d) is the small angle (5°) integrated EDCs based on panel (b), and panel (e) shows the extracted two special EDCs indicated by green in panel (d).

It can be seen from panel (a) that the band dispersions we measured along the M-X direction are clearly resolved which is useful to get an overview of the whole dispersion while it is difficult to assess the band splitting along M-X direction. However, in panel (b) it seems feasible to distinguish the band splitting along M-X direction and band degeneracy at X point, as indicated by the DFT plots. To further reveal this band degeneracy and splitting, panel (c) shows the high contrast of the intensity after second differential, where one can clearly distinguish the band splitting along M-X direction for VB1 and VB2. This is also confirmed by small angle integral of the EDCs shown in panels (d) and (e), in which one can find that there are some discernible peaks that corresponding to different valence bands. However due to the small gaps between VB3 and VB4, VB5 and VB6 and linewidth broadening which is larger than the peak splitting, it is not easy to clearly separate these peaks.

Figure 4.6 Band degeneracy and splitting along M-X direction. (a) A large energy range overview of the band dispersions along M-X direction. (b) Top three pairs of the valence bands with the overlay of DFT plots indicated in (a) by rectangle. (c) Second differential of the top three pairs valence bands. (d) Small angle integral of these valence bands, where the blue ones respectively represent the X point and the point Z in vicinity of X point which are extracted in (e).

4.2.4 APRES study of the band dispersion along Γ-X direction

Figure 4.7 shows the band dispersions along Γ-X direction, where panel (a) present a large energy range from -7.5eV to -1eV for a general overview of the band structure, and panel (b) shows the zoom in structure with DFT plots overlaid on it of the top three pairs valence bands corresponding to the rectangle in (a), and (c) is the second differential structure of these valence bands, and panel (d) is the angle integrated EDCs where two special curves were extracted in panel (e).

One can find that the experimentally measured band structure generally agrees with the DFT predication, shown in panels (a) and (b), this can confirm the orbital and SOC interaction which was discussed in section 3.3. In panel (c) it clearly shows the band dispersion after second differential. This is further confirmed by the angle integral EDCs in panel (d) and (e) in which

the energy positions (peaks) of theses valence bands can be clearly distinguished. What is more, the peaks position distances (i.e., the gap size) of different valence bands, such as the band gap of VB5 and VB6 (i.e., the peak position distance between Δ5 and Δ6), is much larger than the ones along M-X direction as experimentally shown in Figure 4.6(e).

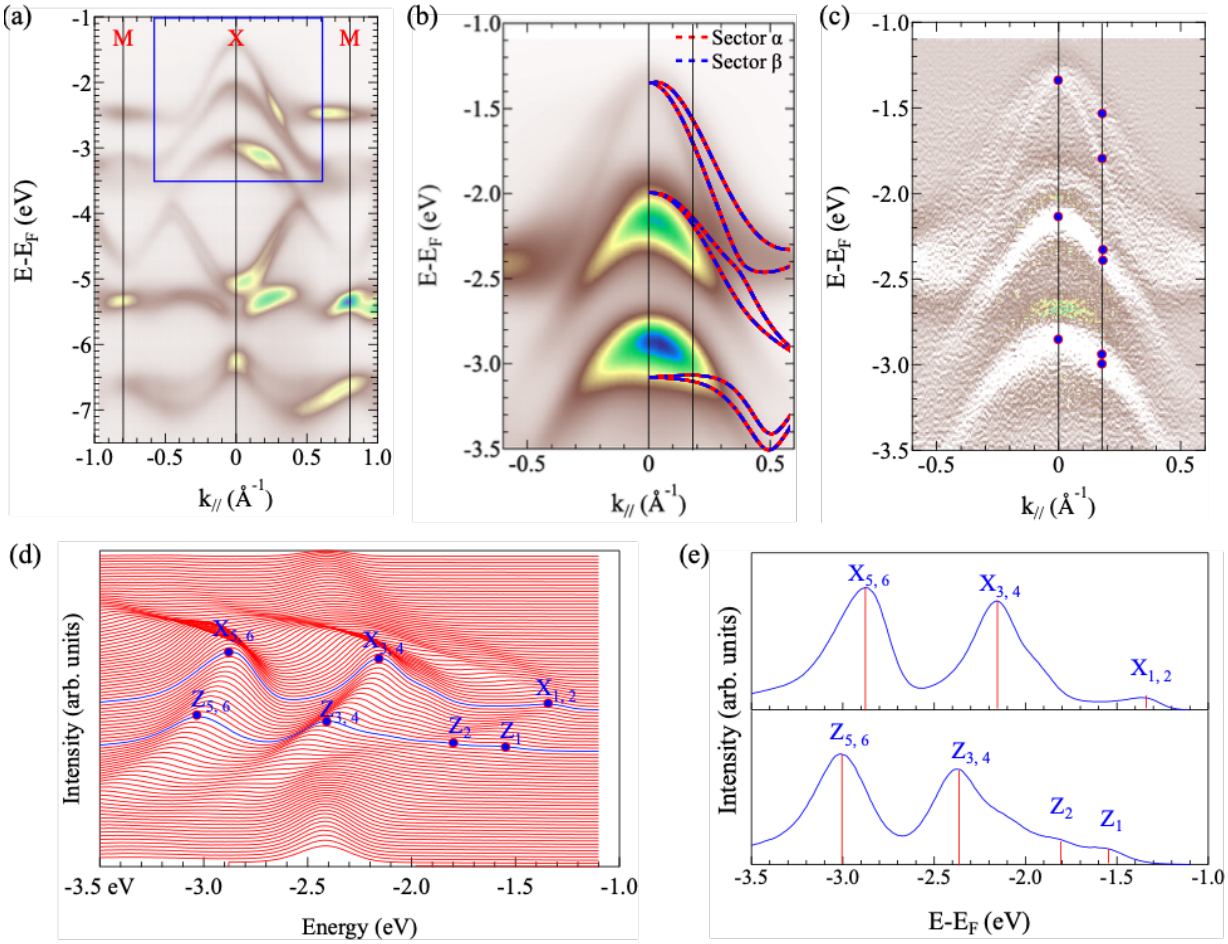

Figure 4.7 Band degeneracy and splitting along Γ-X direction. (a) A large energy range overview of the band dispersions along Γ-X direction. (b) Top three pairs of the valence bands with the overlay of DFT plots indicated in (a) by rectangle. (c) Second differential of the top three pairs valence bands. (d) Small angle integral of these valence bands, where the blue ones respectively represent the Γ point and the point Δ in vicinity of Γ point which are extracted in (e).

4.3 Summary

The high quality BiOI samples in this study has been confirmed by X-ray diffraction, very low energy electron diffraction and core-level photoemission spectroscopy. The electronic structures of the k_z dispersion of BiOI obtained by both DFT calculation and ARPES measurement consistently show a 2D behavior with a relatively flat dispersion along the c axis.

By directly comparing the calculated bulk band structure with the ARPES data, a good agreement is found, indicating that the surface effect that breaks the global inversion symmetry is relatively weak. The predicted four-fold degeneracy at the X and M points and the splitting two-fold degenerate branches (VB1 to VB6) away from X and M are all supported by the ARPES measured dispersion.

Furthermore, the EDCs measured along the M-X-M and X-Γ-X directions show that at the X point, the degenerate peaks, *i.e.*, $X_{1,2}, X_{3,4}$ and $X_{5,6}$ are unambiguously present, while at the Γ point, each of the degenerate peak splits into two individual peaks, *i.e.*, from Γ_1 to Γ_6. Consequently, three pairs of Rashba-like hole-type valence bands are formed at the X and M points, with the band crossing points located around –1.4 eV, –2.1 eV, and –3.0 eV for the X point, respectively. These results agree well with our calculation that only the time-reversal invariant momenta at the BZ boundary (e.g., the X point) demonstrate a four-fold degeneracy, while the Γ point does not exhibit such behavior, thus confirming the nonsymmorphic feature of the material.

Chapter 5 Observation of the Hidden Spin Polarization in Centrosymmetric BiOI

5.1 Introduction

Exploring different quantum materials with strong HSP effects could considerably expand the choice of materials for nonmagnetic spintronic devices. However, while the local symmetry breaking in the real space is the essential characteristics of the HSP, its underlying physics, involving the microscopic mechanism of the way the spin, momentum, and sector lock to each other, remains elusive. Recent theoretical works predicted that the magnitude of the HSP effect is distinct around the Brillouin zone (BZ) center and the BZ boundary. Here, by using systematic spin-ARPES measurements, we have directly investigated the spin polarization of a single crystal BiOI with nonsymmorphic symmetry. We have observed up to 80% net spin polarization along the BZ boundary (X-M) but significantly suppressed spin polarization around Γ, indicating a unique momentum dependence of the HSP effect. These measured results confirm our tight-binding (TB) model and density functional theory (DFT) calculations that the nonsymmorphic symmetry minimizes the spin compensation between adjacent sectors at the BZ boundary, thus successfully retaining the local spin polarization of each sector.

5.2 Spin Polarizations along Γ-X Direction

According to our previous theoretical predication that the spin is highly polarized along the Brillouin zone boundary, while the same effect almost vanishes around the zone center due to its nonsymmorphic crystal structure. Note that the spin polarizations at the TRIM, i.e. the BZ center (Γ point) and the X and M points, is fully compensated since in a nonmagnetic centrosymmetric BiOI the high symmetry points will always have zero spin polarization due to the Kramer's degeneracy theorem.

In this section we will systematically present the in-plane spin polarizations of BiOI measured by spin-ARPES with two different geometries, including the vertical Γ-X direction and horizontal Γ-X direction, to compare with our theoretical predications. Here the wide-ranging

measurements involving different geometries is to verify that the observed spin polarization and spin textures are essentially intrinsic.

5.2.1 Spin polarizations along vertical Γ-X direction

Figure 5.1 presents the S_x spin component of the in-plane spin polarization along vertical Γ-X direction measured by spin-ARPES under the photon energy of 30 eV and at the temperature of 30K. The representative spin resolved EDCs (①~⑭) for the top three pairs of the two-fold degenerate bands VB1-VB6 are shown in this figure. The spin-ARPES data clearly shows that at the time-reversal invariant points X and Γ (momentum points ② and ⑪), the spin-resolved EDCs generally full overlap between the spin up and spin down components, indicating negligible spin polarization; this is consistent with the spin degeneracy originating from Kramer's pairs.

When the momenta moved away from the X point, we have observed significant spin polarization (up to 80%) along this vertical Γ-X direction (representative momentum points ④, ⑤, ⑥, ⑦, ⑧, ⑨ and ⑩). For momenta ⑧ and ⑨, nearly all the six VBs were resolved as the individual polarizations peaked with opposing polarization signs in each pair. This is because the band splitting along Γ-X direction was more significant compared to the splitting along the X-M direction as discussed in section 3.3 and section 4.2. In sharp contrast, the spin polarization surrounding the Γ point was very weak which is no more than 30% as indicated by the momentum points ① and ③.

Due to the short photoelectron escape depth, ~5 Å [160], for the photoelectron kinetic energies of 20-100 eV, and a large lattice constant $c = 9.12$ Å, the detected photoemission signal mainly arises from the topmost sector (a) of the cleaved BiOI single crystal, which is favourable to detect the spin polarization from a local sector.

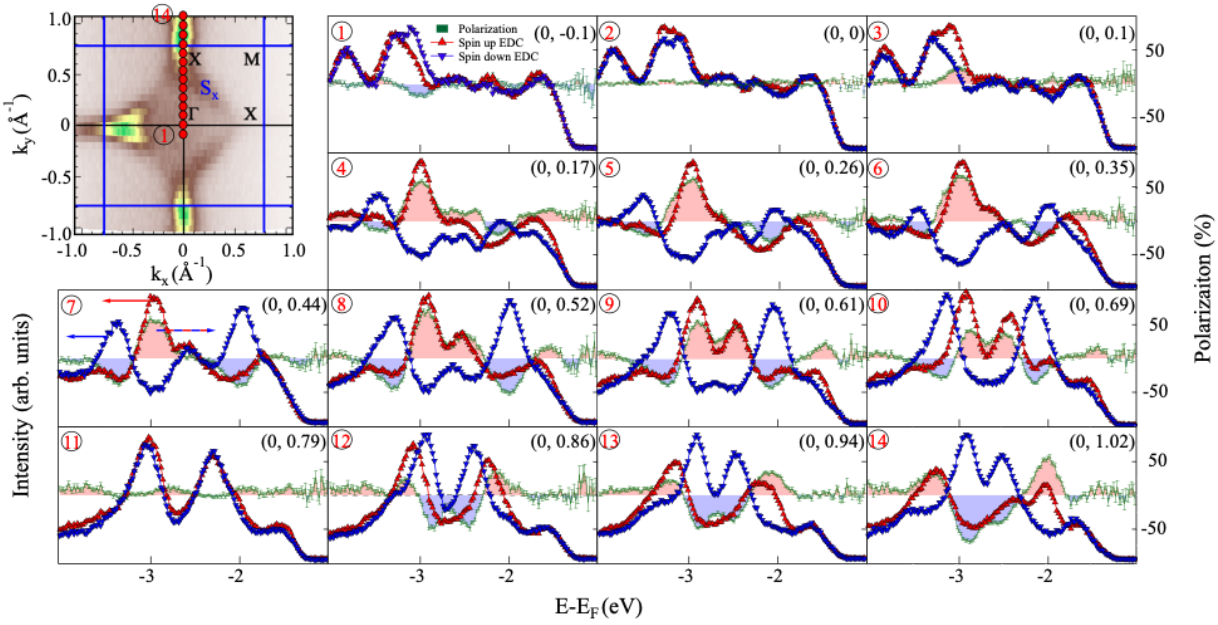

Figure 5.1 The evolution of spin polarization of the S_x component along Γ-X in k_y axis at the photon energy of 30 eV and temperature of 30 K. For each EDC panel the corresponding momentum coordinate (in Å^{-1}) is provided in the top right corner. Red circles in the $k_x - k_y$ mapping also indicate the momentum position for those EDCs.

Figure 5.2 presents the same physics as Figure 5.1 but for the corresponding S_y spin component. There are also fourteen representative spin resolved EDCs (①~⑭) for the top three pairs of the two-fold degenerate bands VB1-VB6. These spin-ARPES data also shows that at the time-reversal invariant points X and Γ (momentum points ② and ⑪), the spin-resolved EDCs generally full overlap between the spin up and spin down components, consistent with the spin degeneracy originating from Kramer's pairs. However, when the momenta moved away from the X point, we find that the spin polarizations are almost negligible (no more than 20%) along this vertical Γ-X direction. Of the same phenomena, the spin polarization surrounding the Γ point was also very weak as indicated by the momentum points ① and ③. This result agrees well with our theoretical predication of the spin textures shown in section 3.4.

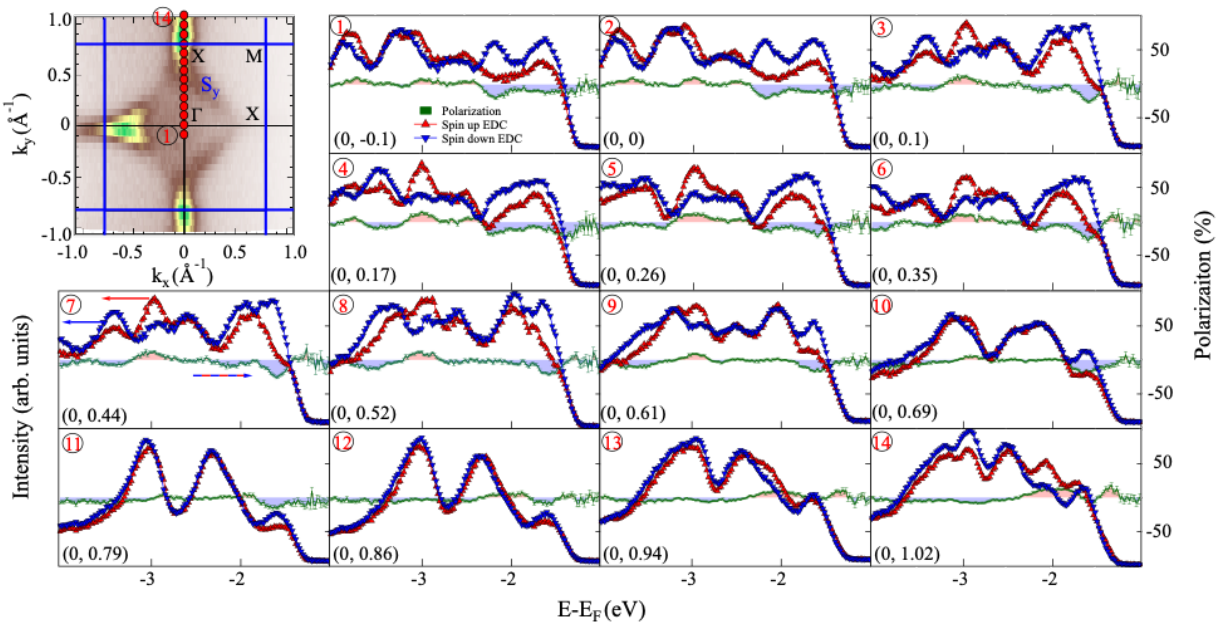

Figure 5.2 The evolution of spin polarization of the S_y component along Γ-X in k_y axis at the photon energy of 30 eV and temperature of 30 K. For each EDC panel the corresponding momentum coordinate (in Å^{-1}) is provided in the top right corner. Red circles in the $k_x - k_y$ mapping also indicate the momentum position for those EDCs.

5.2.2 Spin polarizations along horizontal Γ-X direction

Figure 5.3 shows the spin polarizations of both S_x and S_y components measured at the photon energy of 30 eV and temperature of 30 K, but along horizontal Γ-X direction. There are six representative spin resolved EDCs (①~⑥) for the top three pairs of the two-fold degenerate bands VB1-VB6. One can see from this figure that the spin-ARPES data clearly shows that the spin polarization in both S_x and S_y components when in vicinity to the Γ point is very weak which is no more than 30% as indicated by the momentum points ①. However, when the momenta moved away from the Γ point, we have observed significant spin polarization (up to 80%) in S_y component and almost negligible S_x component along this vertical Γ-X direction (representative momentum points ②, ③, and ④). For momenta ③ and ④, nearly all the six VBs were resolved as the individual polarizations peaked with opposing polarization signs in each pair, which is of great similarity to the phenomena as shown in Figure 5.1. These wide-ranging measurements involving different geometries (in vertical and horizontal directions) clearly verify that the observed spin polarizations are essentially intrinsic. At the time-reversal

invariant points X (momentum point ⑥), the spin-resolved EDCs fully overlap between the spin up and spin down components, indicating the spin degeneracy originating from Kramer's pairs.

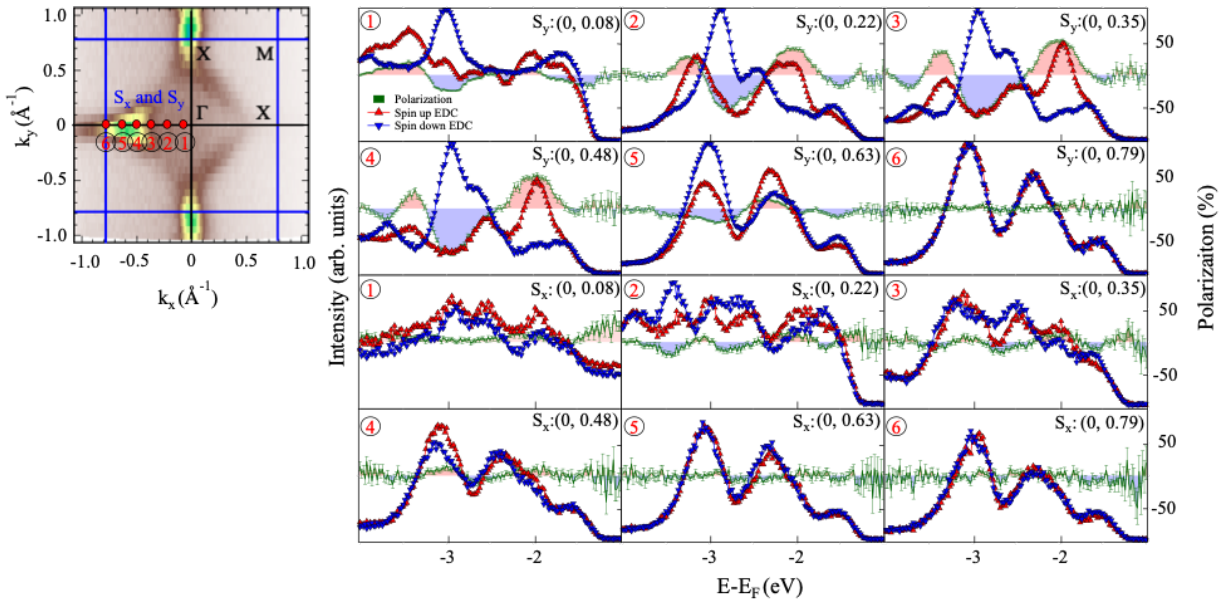

Figure 5.3 Spin polarizations of the S_x and S_y components along horizontal Γ-X direction at the photon energy of 30 eV and temperature of 30 K. For each EDC panel the corresponding momentum coordinate (in $Å^{-1}$) is provided in the right side. Red circles in the $k_x - k_y$ mapping also indicate the momentum position for those EDCs.

It should be emphasized that as shown in Figure 5.1 there seems to be some energy shifts at first glance, especially at the energy positions around 3 eV. However, this can be understood very straightforward if one makes a spin integral of the up and down components of the spin resolved EDCs, i.e., the sum of the intensity of the spin-up and spin-down components. Then we can find that the energy positions for all the peaks are the same, as illustrated in the following Figure 5.4.

This is because in the spin-ARPES measurements, the spin detectors can only measure one component of the spin resolved EDC at one time. Finally, the spin polarization equals to the intensity difference of the both component, which can be formulated as $P_i = \frac{(I_+ - I_-)}{S_{eff}(I_+ + I_-)}$. It is worth noting that, for all the spin resolved EDCs shown in Figure 5.1 the sums of each pair as

spin-integrated EDCs coincide with EDCs measured by normal ARPES in both peak energies and intensity ratios.

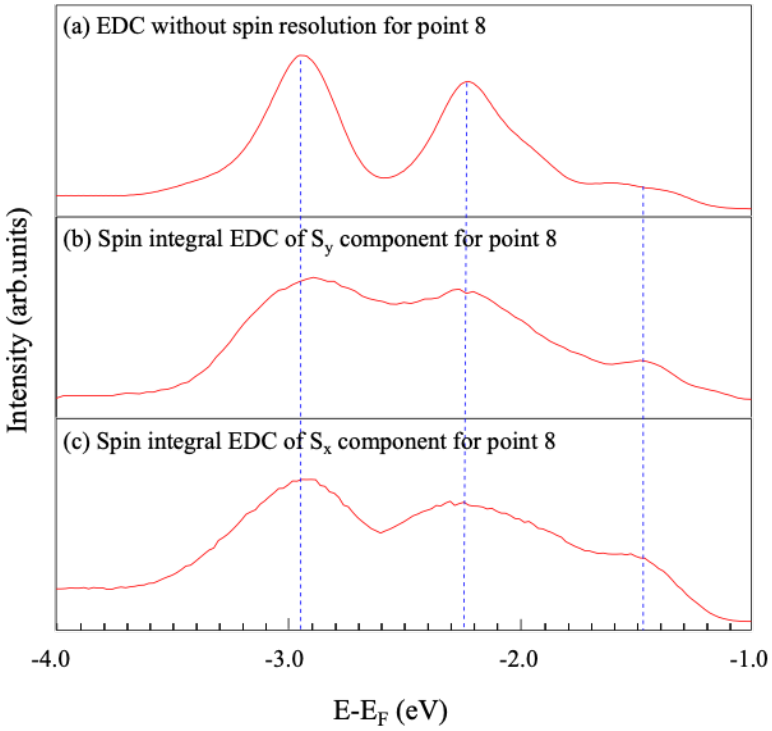

Figure 5.4 Illustration for the energy (peak) positions. Panel (a) depicts the total intensity (i. e. without spin resolution) of the EDC of the position ⑧ in Figure 5.1. Panel (b) depicts the spin integral (i. e. the sum of the S_{y-} and S_{y+} components) EDC of the S_y component of the spin polarization at the same position ⑧ and panel (c) depicts the same physics but for S_x component. It clearly shows that after integration the energy positions agree with each other very well, and the peaks also conform to the energy positions in Figure 4.6.

5.3 Spin Polarizations along M-X Direction

Figure 5.5 presents the spin polarizations along BZ boundary (M-X line) along both horizontal and vertical directions measured under the photon energy of 65 eV and temperature of 30 K. The spin polarization of the S_y component at the top X point is almost zero (momentum point ②) as a result of the symmetry demands, while it increases up to ~80% away from the X point

(momentum points ① and ③) and then decreases to zero at the M point (momentum point ⑥) in the horizontal geometry.

Along the vertical direction (along the k_y direction), the S_x component is suppressed around the X point (including X point which is not shown) and increases abruptly towards M along k_y direction. It reaches ~80% at (-0.79, ±0.4) $Å^{-1}$ (momentum point ⑧) and remains high value along the whole M-X line except the TRIM. It worth mentioning that the sign of the S_x and S_y components are changed with respect to the X points. These experimentally observed results consistent well with our theoretical results in section 3.4, in which the detailed evolution of S_x and S_y components were discussed in different geometries.

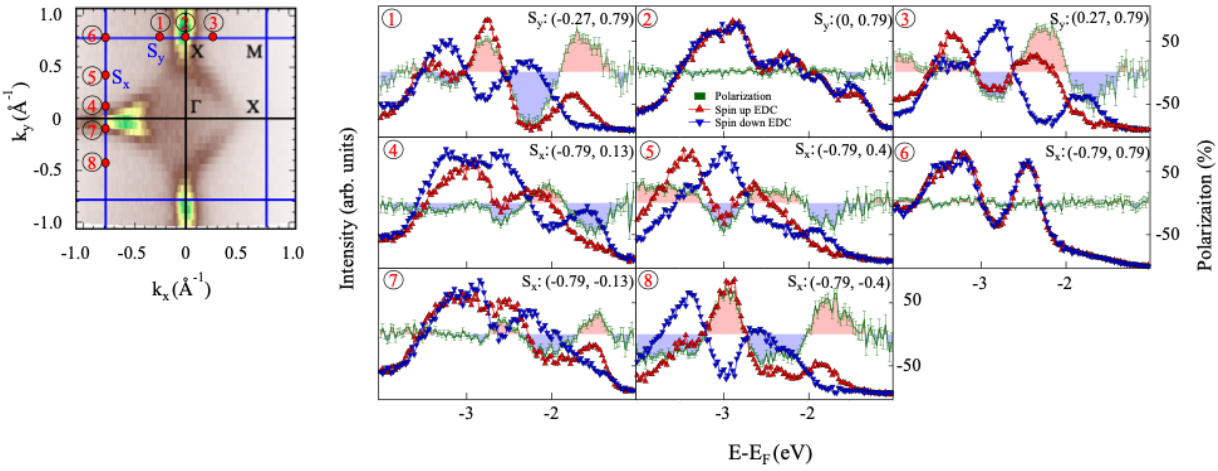

Figure 5.5 The evolution of spin polarization along BZ boundary (M-X) in k_x and k_y axis under the photon energy of 65 eV and temperature of 30 K. For each EDC panel the corresponding momentum coordinate (in Å^{-1}) is provided in the right side. Red circles in the $k_x - k_y$ mapping also indicate the momentum position for those EDCs.

Compared with the previous measurements of HSP materials such as WSe_2 [20], $PtSe_2$ [23], $LaO_{0.55}F_{0.45}BiS_2$ [129] and Bi2212 [24] that focus on the spin-momentum locking around a single high-symmetry point, our work revealed the distinct polarization features surrounding different high-symmetry points and paths (Γ, X, M pints and Γ-X, M-X lines), and observed a sharp contrast between them. Such observations suggest that momentum-dependent spin polarization originates from the HSP rather than merely from the surface potential gradient; further, these observations suggest the key factors affecting the HSP effect, such as the nonsymmorphic symmetry and orbital characters.

5.4 Out-of-plane Spin Polarizations along M-X direction

Our TB model and DFT calculation reveals that even the strongest out-of-plane spin texture (located at the centre of the Γ-Z direction) is less than 20%, which is far smaller than the in-plane polarization due to small values of the off-diagonal terms in the model Hamiltonian. Figure 5.6 shows the S_z component of spin polarization along BZ boundary with five representative points. Apparently, the S_z component is negligibly small and decreases dramatically in magnitude but still exists the change of the sign of the spin polarization (momentum points ①, ②, ③ and ④). It is not surprising that at the X point the polarization is zero (momentum point ⑤). This

observed result that the S_z component is much smaller than in plane polarizations, with net spin polarization no more than 20%, consistent well with our DFT prediction.

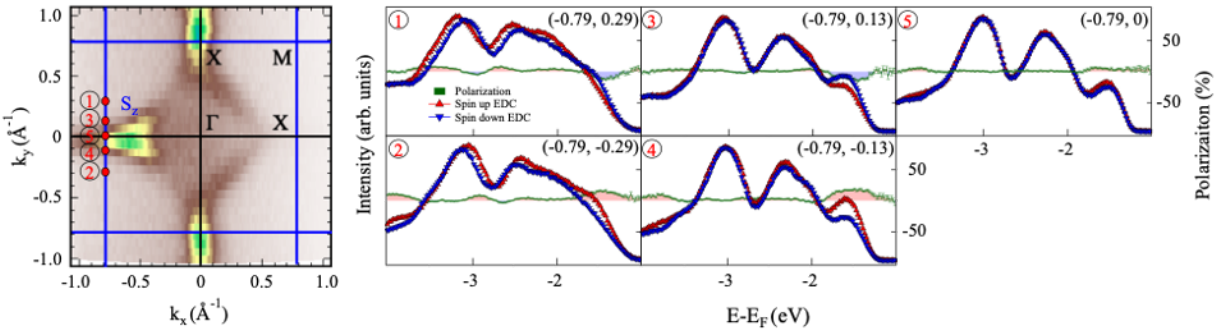

Figure 5.6 S_z component of spin polarization along M-X boundary measured under the photon energy of 30 eV and temperature of 30 K. For each EDC panel the corresponding momentum coordinate (in Å^{-1}) is provided in the right side. Red circles in the $k_x - k_y$ mapping also indicate the momentum position for those EDCs.

5.5 Spin Momentum Locking in Centrosymmetric BiOI

In addition to the momentum dependence and high spin polarization, there is another feature of the HSP at the X point, namely, the spin texture that is localized on the measured sector, manifesting a novel way of spin-momentum-layer locking [161-163]. As illustrated in section 5.2, for the vertical Γ-X line, the S_x component is strong, while the S_x component vanishes. Analogously, for the horizontal Γ-X line, the S_y component is strong, while the S_y component vanishes. Similarly, as illustrated in section 5.3, For the vertical M-X line, the S_x component is strong, while the S_y component almost vanishes. As for the horizontal M-X line, the S_y component is strong, while the S_x component vanishes. Since the S_z component is considerably less intense than the in-plane ones discussed in section 5.4, this finding indicates a perpendicular spin orientation to the wavevector lying in the $k_x - k_y$ plane. We have further confirmed the specific spin texture for all the three pairs of valance bands, as illustrated in Figure 5.7(a) and (b); note that only the spin textures of VB1, VB3, and VB5 are shown in Figure 5.7(b), while the spin orientations of VB2, VB4 and VB6 are opposite to their counterparts. Surprisingly, while the VB1-2 pair shows a weak spin polarization, VB3-4 and VB5-6 pairs exhibit Dresselhaus-

type spin textures with large magnitude, rather than the Rashba spin polarization induced by the local polar field.

Here we employed the *p*-polarization geometry, where the vector potential of incident photon lies on the incidence plane. Based on the dipole selection rule [164,165], the p_x and p_z orbitals are selectively detected. Furthermore, by changing the incidence angle of photons, one can change the ratio of the vector potential components parallel ($A_{\parallel}$) and perpendicular ($A_{\perp}$) to the sample surface. The dipole transition matrix element for the p_z (p_x) orbital is in proportion to the magnitude of $A_{\perp}$ ($A_{\parallel}$) component, and $A_{\perp}$ is larger than $A_{\parallel}$ in the present geometry. In our orbital-projected band calculation in section 3.4, the VB3-6 bands at the X point and the VB1-2 bands at the M point are mainly derived from the p_z orbital. Therefore, we have performed DFT calculations on the p_z-projected spin textures localized on the top BiI layer, i.e., sector a, as shown in Figure 5.7(c) and (d). We found qualitative agreement with the counterparts measured by spin-ARPES shown in section 5.2 and section 5.3. All three VB pairs exhibited weak spin polarization (<20%) around the Γ point. As shown in Figure 5.7(d), in the vicinity of X, only the VB1-2 pair manifested very weak spin polarization due to the tiny contribution of the p_z orbital of these bands (see Figure 3.6). In comparison, the spin textures of VB3-4 and VB5-6 around X exhibited a Dresselhaus type pattern with considerable magnitude. Moreover, the spin patterns of VB3 and VB5 are opposite to each other, which also agrees with the experiment. Thus, we have concluded that the DFT results successfully reproduce the features of the experimental observations, confirming the fact that the measured spin polarization originates from the intrinsic HSP in BiOI.

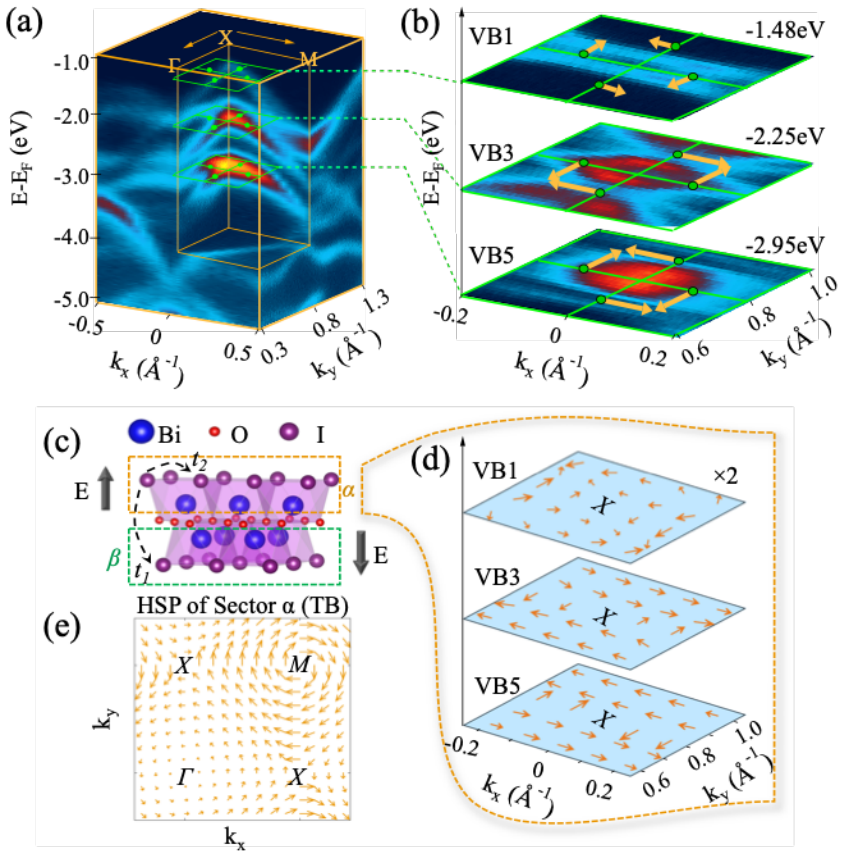

Figure 5.7 HSP effect in BiI sector. (a) Overview of ARPES-measured spectra of BiOI plotted in the $k_x - k_y - E$ space. (b) Schematic sketch of the measured spin textures of VB1, VB3, and VB5 by spin-ARPES, with the momentum cross-sections denoted by the green squares in panel (a). (c) The layered structure of BiOI with two BiI sectors experiencing opposite local dipole fields (black arrows). (d) DFT calculation for p_z-projected HSP of VB1, VB3, and VB5 around X for the sector a. The spin magnitude of VB1 is multiplied by a factor of two. (e) Spin texture for the sector a calculated by our tight-binding (TB) model, showing Dresselhaus and Rashba type HSP effects for X and M, respectively.

5.6 Summary

In summary, combining spin-ARPES measurements and theoretical calculations, we report distinct spin-momentum-layer locking phenomena at different BZ positions in a centrosymmetric material BiOI. The measured spin polarization localized on a specific BiI layer is highly polarized along the BZ boundary but almost vanishes around the zone center due to its

nonsymmorphic crystal structure. The layer-resolved spin texture, either Rashba or Dresselhaus type, reflects the symmetry of both real space and *k*-space. Our findings experimentally demonstrate the existence of the HSP effect and shed light on the design metrics to utilize high spin polarization in centrosymmetric materials by revealing the intimate interplay between spin, orbital, and layer degrees of freedom.

Chapter 6 Conclusion

The spin polarization in nonmagnetic materials is conventionally attributed to the outcome of spin-orbit coupling when the global inversion symmetry is broken. The recently discovered hidden spin polarization (HSP effect) indicates that a specific atomic site asymmetry could also induce measurable spin polarization, leading to a paradigm shift in research on centrosymmetric crystals for potential spintronic applications.

In this study, by using systematic spin- and angle-resolved photoemission spectroscopy compared with theoretical calculations (DFT and TB calculations), we have investigated the electronic structure and particularly the spin polarizations of the single crystal BiOI with nonsymmorphic symmetry (glide plane and screw axis). We have observed up to 80% net spin polarization along the BZ boundary (X-M direction) but suppressed net spin polarization around BZ center (Γ point), indicating a unique momentum dependence of the HSP effect, i.e., the spin-momentum-layer locking in centrosymmetric BiOI.

Our observed spin polarizations (textures) agree well with our tight-binding (TB) model and density functional theory (DFT) calculations that in contrast to the Γ point, the nonsymmorphic symmetry minimizes the spin compensation between adjacent sectors at the BZ boundary, thus successfully retaining the local spin polarization of each sector. This distinct spin-momentum-layer locking phenomena in a centrosymmetric, layered material, not only demonstrates the existence of hidden spin polarization, but also uncovers the microscopic mechanism of spin, momentum, and layer locking to each other BiOI.

Our findings reveal the delicate interplay between spin-momentum-sector locking and symmetry protection in HSP systems, thus shedding light on the possibility of all-electrical manipulation.

Appendices

Appendix A: Matrix representation for symmetry operations in BiOI

Symmetry operator	Matrix representation	Symmetry operator	Matrix representation
$\{e\|0\}$	$\begin{bmatrix}0&0&0&0\\0&1&0&0\\0&0&1&0\\1&0&0&1\end{bmatrix}$	$\{C_{2z}^{1}\|0\}$	$\begin{bmatrix}0&0&0&0\\0&-1&0&0\\0&0&-1&0\\1&0&0&1\end{bmatrix}$
$\{C_{4z}^{1}\|(1/2,1/2,0)\}$	$\begin{bmatrix}0.5&0&0&0\\0.5&0&1&0\\0&-1&0&0\\1&0&0&-1\end{bmatrix}$	$\{C_{4z}^{3}\|(1/2,1/2,0)\}$	$\begin{bmatrix}0.5&0&0&0\\0.5&0&1&0\\0&-1&0&0\\1&0&0&1\end{bmatrix}$
$\{C_{2y}^{1}\|(1/2,1/2,0)\}$	$\begin{bmatrix}0.5&0&0&0\\0.5&-1&0&0\\0&0&1&0\\1&0&0&-1\end{bmatrix}$	$\{C_{2x}^{1}\|(1/2,1/2,0)\}$	$\begin{bmatrix}0.5&0&0&0\\0.5&1&0&0\\0&0&-1&0\\1&0&0&-1\end{bmatrix}$
$\{M_zM_xC_{4z}^{1}\|0\}$	$\begin{bmatrix}0&0&0&0\\0&0&1&0\\0&1&0&0\\1&0&0&-1\end{bmatrix}$	$\{M_zM_yC_{4z}^{3}\|0\}$	$\begin{bmatrix}0&0&0&0\\0&0&-1&0\\0&-1&0&0\\1&0&0&-1\end{bmatrix}$
$\{i\|(1/2,1/2,0)\}$	$\begin{bmatrix}0.5&0&0&0\\0.5&-1&0&0\\0&0&-1&0\\1&0&0&-1\end{bmatrix}$	$\{M_z\|(1/2,1/2,0)\}$	$\begin{bmatrix}0.5&0&0&0\\0.5&1&0&0\\0&0&1&0\\1&0&0&-1\end{bmatrix}$
$\{M_xC_{4z}^{1}\|0\}$	$\begin{bmatrix}0&0&0&0\\0&0&1&0\\0&-1&0&0\\1&0&0&-1\end{bmatrix}$	$\{M_zC_{4z}^{3}\|0\}$	$\begin{bmatrix}0&0&0&0\\0&0&-1&0\\0&1&0&0\\1&0&0&-1\end{bmatrix}$
$\{M_x\|0\}$	$\begin{bmatrix}0&0&0&0\\0&1&0&0\\0&0&-1&0\\1&0&0&-1\end{bmatrix}$	$\{M_y\|0\}$	$\begin{bmatrix}0&0&0&0\\0&-1&0&0\\0&0&1&0\\1&0&0&-1\end{bmatrix}$

$\{M_x C_{4z}^3 \mid (1/2\,, 1/2\,, 0)\}$	$\begin{bmatrix} 0.5 & 0 & 0 & 0 \\ 0.5 & 0 & -1 & 0 \\ 0 & -1 & 0 & 0 \\ 1 & 0 & 0 & 1 \end{bmatrix}$	$\{M_x C_{4z}^1 \mid (1/2\,, 1/2\,, 0)\}$	$\begin{bmatrix} 0.5 & 0 & 0 & 0 \\ 0.5 & 0 & 1 & 0 \\ 0 & 1 & 0 & 0 \\ 1 & 0 & 0 & 1 \end{bmatrix}$

Appendix B: Details of DFT calculations

Input file (1): POSCAR

Bi2I2O2	#Name of system
1.00000000000000	#Scaling factor
3.9800000000000000 0.0000000000000000 0.0000000000000000 0.0000000000000000 3.9800000000000000 0.0000000000000000 0.0000000000000000 0.0000000000000000 9.1400000000000006	#These three lines define the lattice vectors of the crystal cell.
Bi I O	#Constituent element
2 2 2	#Number of atoms
Direct	#Direct coordinates
-0.0000000000998772 0.4999999998898549 0.8621613016748401 0.5000000000998771 0.0000000001101451 0.1378386983251599 0.0000000000214139 0.5000000002109384 0.3417265457912487 0.4999999999785861 -0.0000000002109381 0.6582734542087512 -0.0000000004758274 0.0000000004804904 -0.0000000000331731 0.5000000004758275 0.4999999995195097 0.0000000000331731	#These six lines give the three coordinates for each atom in the form of $\vec{R} = x_1\vec{a}_1 + x_2\vec{a}_2 + x_3\vec{a}_3$.

Input file (2): POTCAR

When we preparing the POTCAR file (pseudopotential, PP file), according to the elements in the system, we need to combine the POTCAR of three elements (Bi, I, O) to form a new POTCAR file, by using the command:

$$cat\ PAW\_PBE/Bi/POTCAR\ PAW\_PBE/O/POTCAR\ >\ BiOI/POTCAR$$

The parameters of POTCAR for each atom can be directly recommended by VASP. Here is an example of the iodine's POTCAR file (only the key information is extracted):

PAW_PBE I 08Apr2002	#Name and date
7.00000000000000	#No. of valency electrons
parameters from PSCTR are:	
VRHFIN =I : s2p5	# Atomic configuration

LEXCH = PE	# Type of E_{xc}
EATOM = 315.8678 eV, 23.2156 Ry	#Energy of pseudoatom
TITEL = PAW_PBE I 08Apr2002	#Same as 1st line
LULTRA = F use ultrasoft PP ?	#False:Not to use USPP
IUNSCR = 1 unscreen: 0-lin 1-nonlin 2-no	#1:Nonlinear unscreen
RPACOR = 2.200 partial core radius	#Raius of partial core
POMASS = 126.904; ZVAL = 7.000 mass and valenz	# Mass of pseudoatom; No. of valence electrons
RCORE = 2.300 outmost cutoff radius	#Radius of outmost cutoff
RWIGS = 2.810; RWIGS = 1.487 wigner-seitz radius (au A)	# Wigner-Seitz radius for each atom type.
ENMAX = 175.647; ENMIN = 131.735 eV	#Max. and Min. cutoff energies
ICORE = 3 local potential	#Local potential of pseudoatom
LCOR = T correct aug charges	#True to correct augmentation (aug.) charges
LPAW = T paw PP	#True to use PAW PP
EAUG = 370.139	#Energy cutoff for aug. charge
DEXC = 0.000	#Derivative of exchange and correlation
RMAX = 2.359 core radius for proj-oper	
RAUG = 1.300 factor for augmentation sphere	
RDEP = 2.392 radius for radial grids	
RDEPT = 2.170 core radius for aug-charge	

Input file (3): KPOINTS

BiOI	#Name of system
0	#Auto to generate k points
G	#Generate the k points with Gamma point as the center
18 18 10	#Number of grids in k space
0 0 0	#Translation in k space

Input file (4): INCAR

SYSTEM = BiOI	#Name in the comment line
# Parallelisation	
NPAR = 8 # 4-24, 5-40, 6-48, 8-80/128, 16-256 cores	#Number of cores to execute the parallel calculation
# Initialisation	
ISTART = 0	# 0: start a new calculation
ICHARG = 2	# 2: The initial charge density is determined by pseudopotential and construct LCAO
	# Electronic self-consistent iteration (SCI)
# Electronic Relaxation	# Precision of the real space projectors
PREC = ACCURATE	# Projection done in real space
LREAL = AUTO	# Electronic relaxation optimization algorithm
ALGO = NORMAL	# Cutoff energy
ENCUT = 500	# Maximum steps allowed for SCI
NELM = 200	# Minimum steps allowed for SCI
NELMIN = 5	# Convergence limit
EDIFF = 1E-06	# Additional grid is used
ADDGRID = TRUE	# Non-spherical contributions from the gradient corrections inside the PAW spheres will be included
LASPH = TRUE	# Spin polarized calculations are performed.
ISPIN = 2	# Use symmetry
ISYM = 2	
# Ionic Relaxation	# Atomic position optimization
EDIFFG = -1e-03	# Break condition for the ionic relaxation loop
IBRION = -1	# The ions are not moved
ISIF = 2	# Stress tensor is calculated and positions are allowed to change
ISMEAR = 0	# Partial occupancies are smeared by Gaussian for each orbital
SIGMA = 0.03	# The width of the smearing in 0.03eV
NSW = 0	# Maximum number of ionic steps
# Miscellaneous	
	# DOSCAR and lm-decomposed PROCAR are written

LORBIT = 11	# Number of gridpoints on which the DOS is evaluated
# NEDOS = 2000	# Charge densities (files CHGCAR and CHG) are written
LCHARG = TRUE	# wavefunctions are written to the WAVECAR file
LWAVE = TRUE	# Number of bands in the calculation
NBANDS = 88	
# SOC and other	# Spin-orbit coupling is taken into account
LSORBIT = TRUE	# DFT-D2 method of correction is calculated
LVDW = TRUE	

Appendix C: Slater-Koster Approximation in TB Model

"Tight binding" has existed for many years as a convenient and transparent model for the description of electronic structure in molecules and solids [166]. The classic paper of Slater and Koster (SK) [152] provides the systematic procedure for formulating a tight binding model. In their paper one can find the famous "Slater–Koster" parameters that are used to build a tight binding Hamiltonian.

Considering a crystal whose Hamiltonian can be written as $H = -\frac{\hbar^2}{2m}\nabla^2 + V_R(\vec{r})$, for each atomic orbital with quantum numbers lm one can construct a Bloch state: $\psi_{lm}^{\alpha}(k,r) = \frac{1}{\sqrt{N}}\Sigma_i e^{iT_i\cdot k}\psi_{lm}(r - T_i - R_\alpha)$ where T_i is the ith lattice vector and R_α is the position of atom α in the unit cell. In this Bloch basis, the Hamiltonian and the overlap matrix are given by:

$$H_{lm,l'm'}^{\alpha,\alpha'}(k) = \left\langle \psi_{lm}^{\alpha}(k)\middle|H\middle|\psi_{l'm'}^{\alpha'}(k)\right\rangle \tag{C-1}$$

$$O_{lm,l'm'}^{\alpha,\alpha'}(k) = \left\langle \psi_{lm}^{\alpha}(k)\middle|\psi_{l'm'}^{\alpha'}(k)\right\rangle \tag{C-2}$$

The solution to the secular equation yields the band structure. The Hamiltonian matrix is thus given by

$$H_{lm,l'm'}^{\alpha,\alpha'}(k) = \varepsilon_{l'\alpha'}^{0} O_{lm,l'm'}^{\alpha,\alpha'}(k) + \Delta\varepsilon_{lm,l'm'}^{\alpha}\delta_{\alpha,\alpha'} - \frac{1}{N}\sum_{i\alpha\neq i'\alpha'} e^{i(T_{i'}-T_i)\cdot k} t_{lm,l'm'}^{i\alpha,i'\alpha'} \tag{C-3}$$

where $\varepsilon_{l'\alpha'}^{0}$ are atomic levels, $\Delta\varepsilon_{lm,l'm'}^{\alpha} = \int dr\psi_{lm}^{*}(r - R_\alpha)[V_R(r) - V(r - R_\alpha)]\psi_{l'm'}(r - R_\alpha)$ is the crystal-field matrix, and $t_{lm,l'm'}^{i\alpha,i'\alpha'} = -\int dr\psi_{lm}^{*}(r - R_\alpha - T_i)[V_R(r) - V(r - R_{\alpha'} - T_{i'})]\psi_{l'm'}(r - R_{\alpha'} - T_{i'})$ is the hopping integral (parameter). This hopping parameter contains two-center and three-center terms, if the basis is localized, one can ignore the three-center contributions and assume that $t_{lm,l'm'}^{i\alpha,i'\alpha'} \sim -V_{lm,l'm'}^{i\alpha,i'\alpha'}$. This is the so-called Slater-Koster two-center integral, which can be expressed as a function of few independent two-center integrals, shown in the following table for s, p, and d-functions forming σ, π, and δ bonds.

Table C1 Slater-Koster integrals for s, p, and d-functions where $\vec{d}$ is the distance between the atoms and l, m and n are the direction cosines to the neighboring atom defined as $l = \vec{d} \cdot \vec{x}/d$, $m = \vec{d} \cdot \vec{y}/d$, $n = \vec{d} \cdot \vec{z}/d$.

$$
\begin{aligned}
E_{s,s} &= V_{ss\sigma} \\
E_{s,x} &= lV_{sp\sigma} \\
E_{x,x} &= l^2 V_{pp\sigma} + (1-l^2)V_{pp\pi} \\
E_{x,y} &= lmV_{pp\sigma} - lmV_{pp\pi} \\
E_{x,z} &= lnV_{pp\sigma} - lnV_{pp\pi} \\
E_{s,xy} &= \sqrt{3}lmV_{sd\sigma} \\
E_{s,x^2-y^2} &= \frac{\sqrt{3}}{2}(l^2-m^2)V_{sd\sigma} \\
E_{s,3z^2-r^2} &= [n^2 - (l^2+m^2)/2]V_{sd\sigma} \\
E_{x,xy} &= \sqrt{3}l^2 mV_{pd\sigma} + m(1-2l^2)V_{pd\pi} \\
E_{x,yz} &= \sqrt{3}lmnV_{pd\sigma} - 2lmnV_{pd\pi} \\
E_{x,zx} &= \sqrt{3}l^2 nV_{pd\sigma} + n(1-2l^2)V_{pd\pi} \\
E_{x,x^2-y^2} &= \frac{\sqrt{3}}{2}l(l^2-m^2)V_{pd\sigma} + l(1-l^2+m^2)V_{pd\pi} \\
E_{y,x^2-y^2} &= \frac{\sqrt{3}}{2}m(l^2-m^2)V_{pd\sigma} - m(1+l^2-m^2)V_{pd\pi} \\
E_{z,x^2-y^2} &= \frac{\sqrt{3}}{2}n(l^2-m^2)V_{pd\sigma} - n(l^2-m^2)V_{pd\pi} \\
E_{x,3z^2-r^2} &= l[n^2 - (l^2+m^2)/2]V_{pd\sigma} - \sqrt{3}ln^2 V_{pd\pi} \\
E_{y,3z^2-r^2} &= m[n^2 - (l^2+m^2)/2]V_{pd\sigma} - \sqrt{3}mn^2 V_{pd\pi} \\
E_{z,3z^2-r^2} &= n[n^2 - (l^2+m^2)/2]V_{pd\sigma} + \sqrt{3}n(l^2+m^2)V_{pd\pi} \\
E_{xy,xy} &= 3l^2m^2V_{dd\sigma} + (l^2+m^2-4l^2m^2)V_{dd\pi} + (n^2+l^2m^2)V_{dd\delta} \\
E_{xy,yz} &= 3lm^2nV_{dd\sigma} + ln(1-4m^2)V_{dd\pi} + ln(m^2-1)V_{dd\delta} \\
E_{xy,zx} &= 3l^2mnV_{dd\sigma} + mn(1-4l^2)V_{dd\pi} + mn(l^2-1)V_{dd\delta} \\
E_{xy,x^2-y^2} &= \frac{3}{2}lm(l^2-m^2)V_{dd\sigma} + 2lm(m^2-l^2)V_{dd\pi} + [lm(l^2-m^2)/2]V_{dd\delta} \\
E_{yz,x^2-y^2} &= \frac{3}{2}mn(l^2-m^2)V_{dd\sigma} - mn[1+2(l^2-m^2)]V_{dd\pi} + mn[1+(l^2-m^2)/2]V_{dd\delta} \\
E_{zx,x^2-y^2} &= \frac{3}{2}nl(l^2-m^2)V_{dd\sigma} + nl[1-2(l^2-m^2)]V_{dd\pi} - nl[1-(l^2-m^2)/2]V_{dd\delta} \\
E_{xy,3z^2-r^2} &= \sqrt{3}\left[lm(n^2-(l^2+m^2)/2)\right]V_{dd\sigma} - 2lmn^2V_{dd\pi} + \left[lm(1+n^2)/2\right]V_{dd\delta}\right] \\
E_{yz,3z^2-r^2} &= \sqrt{3}\left[mn(n^2-(l^2+m^2)/2)V_{dd\sigma} + mn(l^2+m^2-n^2)V_{dd\pi} - \left[mn(l^2+m^2)/2\right]V_{dd\delta}\right] \\
E_{zx,3z^2-r^2} &= \sqrt{3}\left[ln(n^2-(l^2+m^2)/2)V_{dd\sigma} + ln(l^2+m^2-n^2)V_{dd\pi} - \left[ln(l^2+m^2)/2\right]V_{dd\delta}\right] \\
E_{x^2-y^2,x^2-y^2} &= \frac{3}{4}(l^2-m^2)^2V_{dd\sigma} + [l^2+m^2-(l^2-m^2)^2]V_{dd\pi} + [n^2+(l^2-m^2)^2/4]V_{dd\delta} \\
E_{x^2-y^2,3z^2-r^2} &= \sqrt{3}\left[(l^2-m^2)[n^2-(l^2+m^2)/2]V_{dd\sigma}/2 + n^2(m^2-l^2)V_{dd\pi} + [(1+n^2)(l^2-m^2)/4]V_{dd\delta}\right] \\
E_{3z^2-r^2,3z^2-r^2} &= [n^2-(l^2+m^2)/2]^2V_{dd\sigma} + 3n^2(l^2+m^2)V_{dd\pi} + \frac{3}{4}(l^2+m^2)^2V_{dd\delta}
\end{aligned}
$$

Appendix D: Weighted Atomic Orbital Occupancy for VB1 to VB6

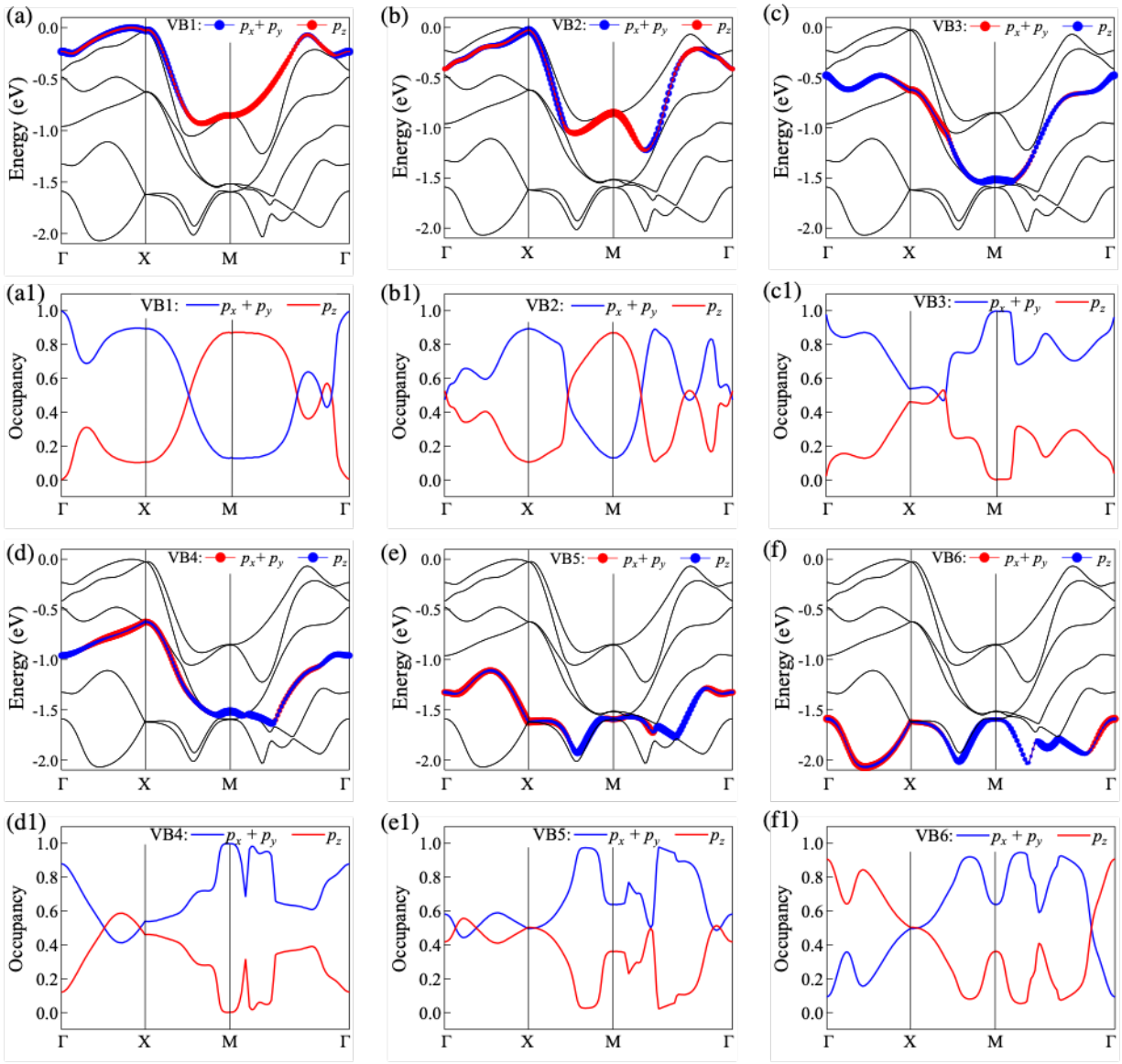

Figure D1. Weighted atomic orbital occupancy for VB1 to VB6. The *p* orbital is a sum of all the p orbitals of Bi, I, and O atoms.

Appendix E: Proof of HSP Gauge Invariant

As one can see that in the TB model, we get a particular solution $\Psi_1 = \frac{1}{\sqrt{2}}\begin{pmatrix} 1 \\ D^*/U \\ -M/U \\ 0 \end{pmatrix}, \Psi_2 = \frac{1}{\sqrt{2}}\begin{pmatrix} 0 \\ -M/U \\ -D/U \\ 0 \end{pmatrix}, \Psi_3 = \frac{1}{\sqrt{2}}\begin{pmatrix} 1 \\ -D^*/U \\ M/U \\ 0 \end{pmatrix}, \Psi_4 = \frac{1}{\sqrt{2}}\begin{pmatrix} 1 \\ M/U \\ D/U \\ 0 \end{pmatrix}$ (3.40). However, generally, by applying the linear combinations of this basis Ψ_1, Ψ_2 (Ψ_3, Ψ_4), there seems a gauge problem. Here we will proof that the HSP effect is gauge invariant.

First, we can construct a set of new double degenerate states $\Psi_1' = c_1\Psi_1 + c_2\Psi_2$ and $\Psi_2' = c_3\Psi_1 + c_4\Psi_2$. Then, set $\frac{c_4^*}{c_3^*} = -\frac{c_1}{c_2}$ to make sure the basis transforming matrix to be unitary. Thus, the new doble degenerate states can be written as $\Psi_1' = c_1\Psi_1 + c_2\Psi_2$ and $\Psi_2' = c_2^*\Psi_1 - c_1^*\Psi_2$ with $|c_1|^2 + |c_2|^2 = 1$. Now, using this new basis Ψ_1' and Ψ_2', we calculate the physical quantities:

$$\mathrm{P}_1^{\mathrm{sec}} = \frac{1}{2}(|\mathrm{c}_1|^2 - |\mathrm{c}_2|^2) + \frac{1}{2\mathrm{F}^2}[|\mathrm{c}_2|^2 - |\mathrm{c}_1|^2(\mathrm{M}^2 - \mathrm{D}^2) - 2\mathrm{M}(\mathrm{c}_1^*\mathrm{c}_2\mathrm{D} + \mathrm{c}_1\mathrm{c}_2^*\mathrm{D}^*)] \tag{E-1}$$

$$\mathrm{P}_2^{\mathrm{sec}} = \frac{1}{2}(|\mathrm{c}_2|^2 - |\mathrm{c}_1|^2) + \frac{1}{2\mathrm{F}^2}[-|\mathrm{c}_2|^2 - |\mathrm{c}_1|^2(\mathrm{M}^2 - \mathrm{D}^2) + 2\mathrm{M}(\mathrm{c}_1^*\mathrm{c}_2\mathrm{D} + \mathrm{c}_1\mathrm{c}_2^*\mathrm{D}^*)] \tag{E-2}$$

$$s_{1x}^A = \frac{1}{2F}[|c_1|^2(D + D^*) - M(c_1c_2^* + c_1^*c_2)] \tag{E-3}$$

$$s_{2x}^A = \frac{1}{2F}[|c_2|^2(D + D^*) + M(c_1c_2^* + c_1^*c_2)] \tag{E-4}$$

$$s_{1y}^A = \frac{i}{2F}[|c_1|^2(D - D^*) - M(c_1c_2^* - c_1^*c_2)] \tag{E-5}$$

$$s_{2y}^A = \frac{i}{2F}[|c_2|^2(D - D^*) + M(c_1c_2^* - c_1^*c_2)] \tag{E-6}$$

where c_1 or c_2 is variant coefficient. It shows that both sector polarization $\mathrm{P}_{\mathrm{n}}^{\mathrm{sec}}$ and spin momentum s_n^A for a single state vary with the coefficient c_1 or c_2. However, adding the effect of E_1 and E_2, the expectation values of the components of the HSP are:

$$s^A_{(1+2)x} = s^A_{1x} + s^A_{2x} = \frac{1}{2F}(D + D^*) \tag{E-7}$$

$$s^A_{(1+2)y} = s^A_{1y} + s^A_{2y} = \frac{i}{2F}(D - D^*) \tag{E-8}$$

It obviously shows that there is no relation with the coefficient c_1 or c_2. This indicate that the HSP effect is indeed gauge invariant.

Appendix F: Spin Textures for VB1 to VB6

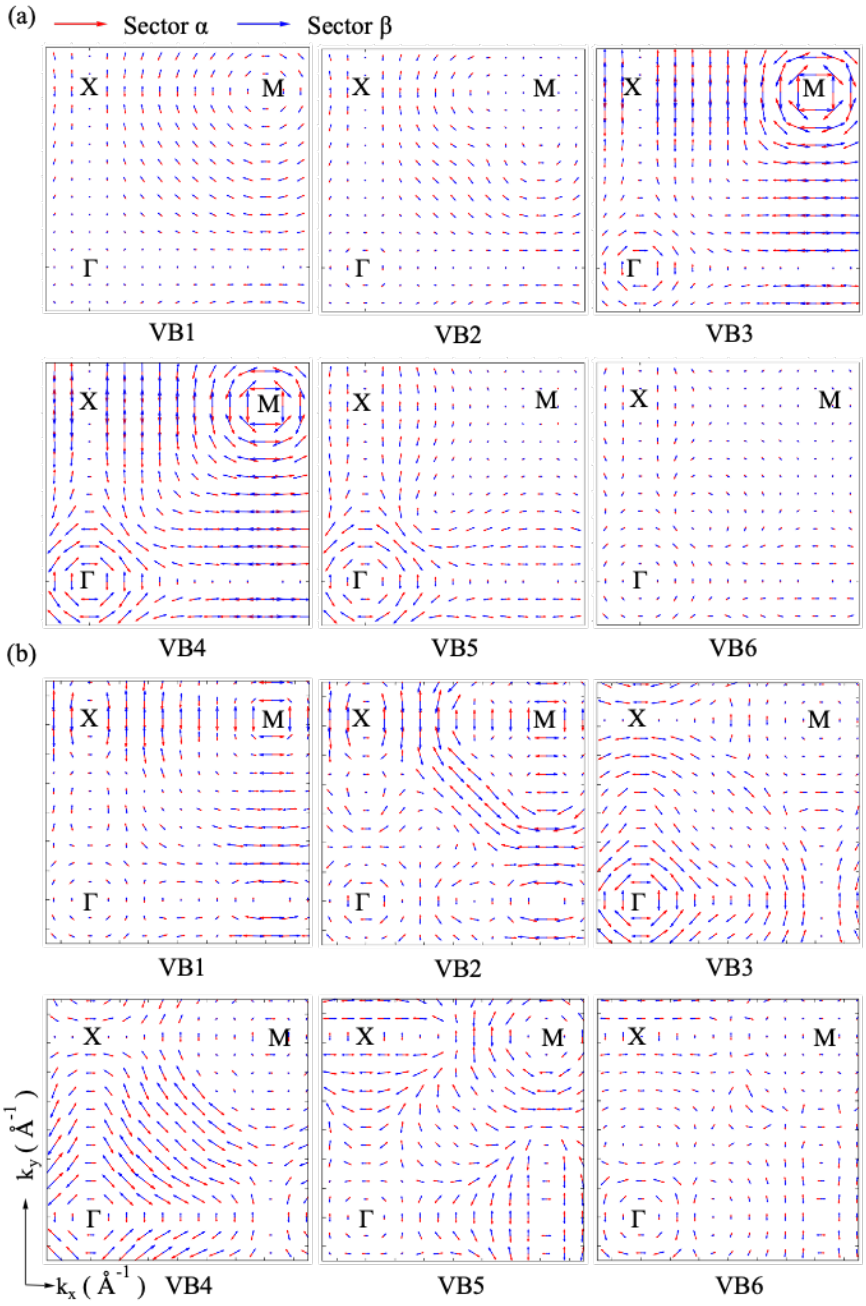

Figure F1 the spin textures of VB1 to VB6. Panel (a) is the one calculated by TB method and panel (b) is the one calculated by DFT method.

References

[1] S. Datta and B. Das, Appl. Phys. Lett. **56**, 665 (1990).

[2] I. Žutić, J. Fabian, and S. D. Sarma, Rev. Mod. Phys. **76**, 323 (2004).

[3] H. C. Koo, J. H. Kwon, J. Eom, J. Chang, S. H. Han, and M. Johnson, Science **325**, 1515 (2009).

[4] A. Manchon, H. C. Koo, J. Nitta, S. Frolov, and R. Duine, Nat. Mater. **14**, 871 (2015).

[5] A. Soumyanarayanan, N. Reyren, A. Fert, and C. Panagopoulos, Nature **539**, 509 (2016).

[6] X. Lin, W. Yang, K. L. Wang, and W. Zhao, Nature Electronics **2**, 274 (2019).

[7] Q. Liu, X. Zhang, J. A. Waugh, D. S. Dessau, and A. Zunger, Phys. Rev. B **94**, 125207 (2016).

[8] J.-W. Luo, G. Bester, and A. Zunger, Phys. Rev. Lett. **102**, 056405 (2009).

[9] R. Winkler, *Spin-orbit coupling effects in two-dimensional electron and hole systems* (Springer Science & Business Media, 2003), Vol. 191, Book-Winkler.

[10] G. Dresselhaus, Phys. Rev. **100**, 580 (1955).

[11] E. I. Rashba, Sov. Phys. Solid State **2**, 1109 (1960).

[12] Y. A. Bychkov and É. I. Rashba, JETP Lett. **39**, 78 (1984).

[13] Y. A. Bychkov and E. I. Rashba, Journal of Physics C: Solid State Physics **17**, 6039 (1984).

[14] Y. A. Bychkov and V. M. n. E. J. Z. E. T. F. Rashba, Zh. Eksp. Teor. Fiz **98**, 726 (1990).

[15] D. Di Sante, P. Barone, R. Bertacco, and S. Picozzi, Adv. Mater. **25**, 509 (2013).

[16] K. Ishizaka *et al.*, Nat. Mater. **10**, 521 (2011).

[17] X. Zhang, Q. Liu, J.-W. Luo, A. J. Freeman, and A. Zunger, Nat. Phys. **10**, 387 (2014).

[18] L. Yuan, Q. Liu, X. Zhang, J.-W. Luo, S.-S. Li, and A. Zunger, Nat. Commun. **10**, 906 (2019).

[19] Z. Yingjie, L. Pengfei, S. Hongyi, Z. Shixuan, X. Hu, and L. Qihang, Chin. Phys. Lett. **37**, 87105 (2020).

[20] J. M. Riley *et al.*, Nat. Phys. **10**, 835 (2014).

[21] E. Razzoli *et al.*, Phys. Rev. Lett. **118**, 086402 (2017).

[22] D. Santos-Cottin *et al.*, Nat. Commun. **7**, 11258 (2016).

[23] W. Yao *et al.*, Nat. Commun. **8**, 14216 (2017).

[24] K. Gotlieb *et al.*, Science **362**, 1271 (2018).

[25] X. Chen *et al.*, Nat. Mater. **18**, 931 (2019).

[26] P.-H. Lin, B.-Y. Yang, M.-H. Tsai, P.-C. Chen, K.-F. Huang, H.-H. Lin, and C.-H. Lai, Nat. Mater. **18**, 335 (2019).

[27] J. Zhou *et al.*, Sci. Adv. **5**, eaau6696 (2019).

[28] J. H. Ryoo and C.-H. Park, Npg Asia Materials **9**, e382 (2017).

[29] R. Gautier, J. M. Klingsporn, R. P. Van Duyne, and K. R. Poeppelmeier, Nat. Mater. **15**, 591 (2016).

[30] Q. Liu, X. Zhang, and A. Zunger, Phys. Rev. Lett. **114**, 087402 (2015).

[31] J. Železný, H. Gao, K. Výborný, J. Zemen, J. Mašek, A. Manchon, J. Wunderlich, J. Sinova, and T. Jungwirth, Phys. Rev. Lett. **113**, 157201 (2014).

[32] P. Wadley *et al.*, Science **351**, 587 (2016).

[33] Q. Liu and A. Zunger, Physical Review X **7**, 021019 (2017).

[34] W. C. Yu, X. Zhou, F.-C. Chuang, S. A. Yang, H. Lin, and A. Bansil, Physical Review Materials **2**, 051201 (2018).

[35] T. Yang *et al.*, Nat. Mater. **19**, 27 (2020).

[36] Q.-F. Liang, J. Zhou, R. Yu, Z. Wang, and H. Weng, Phys. Rev. B **93**, 085427 (2016).

[37] T. Bzdušek, Q. Wu, A. Rüegg, M. Sigrist, and A. A. Soluyanov, Nature **538**, 75 (2016).

[38] L. M. Schoop *et al.*, Nat. Commun. **7**, 1 (2016).

[39] A. Topp *et al.*, Physical Review X **7**, 041073 (2017).

[40] M. Arumugam and M. Y. Choi, J. Ind. Eng. Chem. **81**, 237 (2020).

[41] X. Zhang, L. Zhang, T. Xie, and D. Wang, J. Phys. Chem. C **113**, 7371 (2009).

[42] J. Cao, B. Xu, B. Luo, H. Lin, and S. Chen, Catal. Commun. **13**, 63 (2011).

[43] W. Witczak-Krempa, G. Chen, Y. B. Kim, and L. Balents, Annu. Rev. Condens. Matter Phys. **5**, 57 (2014).

[44] H. Rabitz, R. de Vivie-Riedle, M. Motzkus, and K. Kompa, Science **288**, 824 (2000).

[45] C. Brif, R. Chakrabarti, and H. Rabitz, New J. Phys. **12**, 075008 (2010).

[46] Y.-F. Chang, Int. J. Nano Mater. Sci. **2**, 9 (2013).

[47] D. Basov, R. Averitt, and D. Hsieh, Nat. Mater. **16**, 1077 (2017).

[48] Y. Tokura, M. Kawasaki, and N. Nagaosa, Nat. Phys. **13**, 1056 (2017).

[49] M. Sato and Y. Ando, Rep. Prog. Phys. **80**, 076501 (2017).

[50] S. Haindl *et al.*, Rep. Prog. Phys. **77**, 046502 (2014).

[51] C. Trang *et al.*, Nat. Commun. **11**, 1 (2020).

[52] H. Hertz, Annalen der Physik **267**, 983 (1887).

[53] A. Einstein, Annalen der Physik **322**, 132 (1905).

[54] C. Nordling, E. Sokolowski, and K. Siegbahn, Phys. Rev. **105**, 1676 (1957).

[55] D. H. Bilderback, P. Elleaume, and E. Weckert, J. Phys. B: At., Mol. Opt. Phys. **38**, S773 (2005).

[56] C. Kunz, J. Phys.: Condens. Matter **13**, 7499 (2001).

[57] J. He and Z. Zhao, Natl. Sci. Rev. **1**, 171 (2014).

[58] A. Balerna and S. Mobilio, in *Synchrotron radiation* (Springer, 2015), pp. 3.

[59] M. Ogawa *et al.*, Rev. Sci. Instrum. **83**, 023109 (2012).

[60] X. Zhu *et al.*, Rev. Sci. Instrum. **86**, 083902 (2015).

[61] Spin- and Angle-Resolved Photoelectron Spectroscopy, (Scienta Omicron) https://scientaomicron.com/en/system-solutions/electron-spectroscopy/ARPES-Lab/technology/Spin-ARPES/37 (Accessed March 1st 2021).

[62] 角度分解光電子分光, (Wikipedia) https://zh.wikipedia.org/wiki/%E8%A7%92%E5%88%86%E8%BE%A8%E5%85%89%E9%9B%BB%E5%AD%90%E8%83%BD%E8%AD%9C%E5%AD%B8 (Accessed March 1st 2021).

[63] S. hufner, *Photoelectron Spectroscopy: Principles and Application* (Springer-Verlag Berlin Heidelberg GmbH, 2003).

[64] R. Comin and A. Damascelli, in *Strongly Correlated Systems* (Springer, 2015), pp. 31.

[65] S. Suga and A. Sekiyama, *Photoelectron spectroscopy: bulk and surface electronic structures. 2014* (Springer-Verlag Berlin Heidelberg, 2014).

[66] https://www.cond-mat.de/events/correl14/talks/sing.pdf.

[67] L. Hedin and J. Lee, J. Electron Spectrosc. Relat. Phenom. **124**, 289 (2002).

[68] J. W. Gadzuk and M. Šunjić, Phys. Rev. B **12**, 524 (1975).

[69] J. Stöhr, R. Jaeger, and J. Rehr, Phys. Rev. Lett. **51**, 821 (1983).

[70] T. A. Carlson and M. O. Krause, Phys. Rev. **140**, A1057 (1965).

[71] A. Reimer *et al.*, Phys. Rev. Lett. **57**, 1707 (1986).

[72] J. Hietarinta, B. Grammaticos, B. a. Dorizzi, and A. Ramani, Phys. Rev. Lett. **53**, 1707 (1984).

[73] J. Schirmer, M. Braunstein, and V. McKoy, Phys. Rev. A **44**, 5762 (1991).

[74] G. Bandarage and R. R. Lucchese, Phys. Rev. A **47**, 1989 (1993).

[75] M. Randeria *et al.*, Phys. Rev. Lett. **74**, 4951 (1995).

[76] J. Koralek, J. Douglas, N. Plumb, J. Griffith, S. Cundiff, H. Kapteyn, M. Murnane, and D. Dessau, Rev. Sci. Instrum. **78**, 053905 (2007).

[77] J. Koralek *et al.*, Phys. Rev. Lett. **96**, 017005 (2006).

[78] M. Seah, Surf. Interface Anal. **1**, 86 (1979).

[79] G. Sawatzky, Nature **342**, 480 (1989).

[80] H. Eskes, A. M. Oleś, M. B. Meinders, and W. Stephan, Phys. Rev. B **50**, 17980 (1994).

[81] A. Damascelli, Z. Hussain, and Z.-X. Shen, Rev. Mod. Phys. **75**, 473 (2003).

[82] A. A. Abrikosov, L. P. Gor′kov, and I. E. Dzi͡aloshinskiĭ, *Quantum field theoretical methods in statistical physics* (Pergamon, 1965), Vol. 4.

[83] H. Ehrenreich, F. Seitz, and D. Turnbull, (1973).

[84] A. L. Fetter and J. D. Walecka, *Quantum theory of many-particle systems* (Courier Corporation, 2012).

[85] G. D. Mahan, *Many-particle physics* (Springer Science & Business Media, 2013).

[86] V. L. Bonch-Bruevich and S. V. Tyablikov, *The Green function method in statistical mechanics* (Courier Dover Publications, 2015).

[87] K. Shimada, in *Very High Resolution Photoelectron Spectroscopy* (Springer, 2007), pp. 85.

[88] J. Hermanson, Solid State Commun. **22**, 9 (1977).

[89] H. Iwasawa *et al.*, J. Synchrotron Rad. **24**, 836 (2017).

[90] L. Chernysheva, G. Gribakin, V. Ivanov, and M. Y. Kuchiev, J. Phys. B: At., Mol. Opt. Phys. **21**, L419 (1988).

[91] R. D. Mattuck, *A guide to Feynman diagrams in the many-body problem* (Courier Corporation, 1992).

[92] R. d. L. Kronig, Josa **12**, 547 (1926).

[93] H. A. Kramers, in *Atti Cong. Intern. Fisica (Transactions of Volta Centenary Congress) Como*1927), pp. 545.

[94] T. Valla, A. Fedorov, P. Johnson, and S. Hulbert, Phys. Rev. Lett. **83**, 2085 (1999).

[95] J. Schäfer, D. Schrupp, E. Rotenberg, K. Rossnagel, H. Koh, P. Blaha, and R. Claessen, Phys. Rev. Lett. **92**, 097205 (2004).

[96] M. Repoux, Surf. Interface Anal. **18**, 567 (1992).

[97] S. Tougaard, Surf. Interface Anal. **11**, 453 (1988).

[98] S. Tougaard and I. Chorkendorff, Phys. Rev. B **35**, 6570 (1987).

[99] H. Froitzheim, Topics in Current Physics **4** (1977).

[100] M. P. Seah and W. A. Dench, Surf. Interface Anal. **1**, 2 (1979).

[101] P. J. Feibelman and D. Eastman, Phys. Rev. B **10**, 4932 (1974).

[102] G. Borstel, Applied Physics A **38**, 193 (1985).

[103] F. Reinert and S. Hüfner, New J. Phys. **7**, 97 (2005).

[104] T. Okuda, J. Phys.: Condens. Matter **29**, 483001 (2017).

[105] T. J. Gay and F. Dunning, Rev. Sci. Instrum. **63**, 1635 (1992).

[106] Sherman Function, (Wikepeida) https://en.wikipedia.org/wiki/Sherman_function (Accessed March. 11th 2021).

[107] A. Takayama, *High-Resolution Spin-Resolved Photoemission Spectrometer and the Rashba Effect in Bismuth Thin Films* (Springer, 2014).

[108] J. Kessler, *Polarized electrons* (Springer Science & Business Media, 2013), Vol. 1.

[109] A. Gellrich and J. Kessler, Phys. Rev. A **43**, 204 (1991).

[110] C. Etz, A. Ernst, S. Ostanin, W. Hergert, and I. Mertig, Verhandlungen der Deutschen Physikalischen Gesellschaft (2010).

[111] K. Legg, F. Jona, D. Jepsen, and P. Marcus, Phys. Rev. B **16**, 5271 (1977).

[112] E. Tamura, R. Feder, J. Krewer, R. E. Kirby, E. Kisker, E. L. Garwin, and F. K. King, Solid State Commun. **55**, 543 (1985).

[113] R. Jungblut, C. Roth, F. Hillebrecht, and E. Kisker, Surf. Sci. **269**, 615 (1992).

[114] T. Okuda, Y. Takeichi, Y. Maeda, A. Harasawa, I. Matsuda, T. Kinoshita, and A. Kakizaki, Rev. Sci. Instrum. **79**, 123117 (2008).

[115] Synchrotron Radiation, (Wikipedia) https://en.wikipedia.org/wiki/Synchrotron_radiation (Accessed March 14th 2021).

[116] Undulator, (Wikepedia) https://en.wikipedia.org/wiki/Undulator (Accessed March 16th 2021).

[117] K. Yoshida *et al.*, in *KEK Proc.* (NATIONAL LABORATORY FOR HIGH ENERGY PHYSICS, 1998), pp. 653.

[118] S. Matsuba, K. Goto, and K. Kawase, in *8th Int. Particle Accelerator Conf.(IPAC'17), Copenhagen, Denmark, 14â 19 May, 2017* (JACOW, Geneva, Switzerland, 2017), pp. 2672.

[119] K. Shimada, in *Institutes in Asia Pacific* (AAPPS BULLETIN, 2020), p. 3.

[120] S. Souma, T. Sato, T. Takahashi, and P. Baltzer, Rev. Sci. Instrum. **78**, 123104 (2007).

[121] G. Liu *et al.*, Rev. Sci. Instrum. **79**, 023105 (2008).

[122] T. Kiss *et al.*, Rev. Sci. Instrum. **79**, 023106 (2008).

[123] J. C. Rivière and S. Myhra, *Handbook of surface and interface analysis: methods for problem-solving* (CRC press, 2009).

[124] E. Plum, X.-X. Liu, V. Fedotov, Y. Chen, D. Tsai, and N. Zheludev, Phys. Rev. Lett. **102**, 113902 (2009).

[125] D. Xiao, W. Yao, and Q. Niu, Phys. Rev. Lett. **99**, 236809 (2007).

[126] K. F. Mak, K. L. McGill, J. Park, and P. L. McEuen, Science **344**, 1489 (2014).

[127] M. Gehlmann *et al.*, Scientific Reports **6**, 26197 (2016).

[128] J. Tu *et al.*, Phys. Rev. B **101**, 035102 (2020).

[129] S.-L. Wu *et al.*, Nat. Commun. **8**, 1919 (2017).

[130] C.-X. Liu, Phys. Rev. Lett. **118**, 087001 (2017).

[131] P. A. M. Dirac, *The principles of quantum mechanics (Fourth Edition)* (Oxford University Press, 1958), The International Series of Monographs on Physics.

[132] S. A. Wolf, D. D. Awschalom, R. A. Buhrman, J. M. Daughton, S. von Molnár, M. L. Roukes, A. Y. Chtchelkanova, and D. M. Treger, Science **294**, 1488 (2001).

[133] I. Žutić, J. Fabian, and S. Das Sarma, Rev. Mod. Phys. **76**, 323 (2004).

[134] B. Partoens, Nat. Phys. **10**, 333 (2014).

[135] X. Wang, Doctoral thesis, Hiroshima University, 2020.

[136] G. D. M. S. Dresselhaus, A. Jorio, *Group theory: application to the physics of condensed matter* (Springer, 2008).

[137] T. Hahn, U. Shmueli, and J. W. Arthur, *International tables for crystallography* (Reidel Dordrecht, 1983), Vol. 1.

[138] Introduction to Computational Materials, https://www.vasp.at/vasp-workshop/comput_mat.pdf (Accessed March 28 2021).

[139] E. K. Gross and R. M. Dreizler, *Density functional theory* (Springer Science & Business Media, 2013), Vol. 337.

[140] J. Callaway and N. March, Solid State Physics **38**, 135 (1984).

[141] J. P. Perdew, K. Burke, and Y. Wang, Phys. Rev. B **54**, 16533 (1996).

[142] J. P. Perdew, S. Kurth, A. Zupan, and P. Blaha, Phys. Rev. Lett. **82**, 2544 (1999).

[143] J. Heyd, G. E. Scuseria, and M. Ernzerhof, J. Chem. Phys. **118**, 8207 (2003).

[144] M. Cococcioni and S. De Gironcoli, Phys. Rev. B **71**, 035105 (2005).

[145] F. Aryasetiawan and O. Gunnarsson, Rep. Prog. Phys. **61**, 237 (1998).

[146] G. Kresse and J. Furthmüller, Phys. Rev. B **54**, 11169 (1996).

[147] P. Hohenberg and W. Kohn, Phys. Rev. **136**, B864 (1964).

[148] W. Kohn and L. J. Sham, Phys. Rev. **140**, A1133 (1965).

[149] G. Kresse and D. Joubert, Phys. Rev. B **59**, 1758 (1999).

[150] X. Zhang, Z. Ai, F. Jia, and L. Zhang, J. Phys. Chem. C **112**, 747 (2008).

[151] J. Jiang, X. Zhang, P. Sun, and L. Zhang, J. Phys. Chem. C **115**, 20555 (2011).

[152] J. C. Slater and G. F. Koster, Phys. Rev. **94**, 1498 (1954).

[153] W. A. Harrison, *Electronic structure and the properties of solids: the physics of the chemical bond* (Courier Corporation, 2012).

[154] C. Kittel, *Quantum theory of solids* (John Wiley & Sons, 1987).

[155] P. Schmidt, M. Binnewies, R. Glaum, and M. Schmidt, *Chemical vapor transport reactions–methods, materials, modeling* (InTech Rijeka, Croatia, 2013).

[156] M. Binnewies, M. Schmidt, and P. Schmidt, Z. Anorg. Allg. Chem. **643**, 1295 (2017).

[157] M. A. Gondal, C. Xiaofeng, and M. A. Dastageer, *Novel bismuth-oxyhalide-based materials and their applications* (Springer, 2017).

[158] B. V. Crist, XPS reports **1** (2007).

[159] J. Rumble Jr, D. Bickham, and C. Powell, Surf. Interface Anal. **19**, 241 (1992).

[160] C. J. Powell, A. Jablonski, I. Tilinin, S. Tanuma, and D. R. Penn, J. Electron Spectrosc. Relat. Phenom. **98**, 1 (1999).

[161] A. M. Jones, H. Yu, J. S. Ross, P. Klement, N. J. Ghimire, J. Yan, D. G. Mandrus, W. Yao, and X. Xu, Nat. Phys. **10**, 130 (2014).

[162] X. Xu, W. Yao, D. Xiao, and T. F. Heinz, Nat. Phys. **10**, 343 (2014).

[163] X. Xi, Z. Wang, W. Zhao, J.-H. Park, K. T. Law, H. Berger, L. Forró, J. Shan, and K. F. Mak, Nat. Phys. **12**, 139 (2016).

[164] A. Damascelli, Z. Hussain, and Z.-X. Shen, Rev. Mod. Phys. **75**, 473 (2003).

[165] Y. Cao *et al.*, Nat. Phys. **9**, 499 (2013).

[166] A. T. Paxton, NIC Series **42**, 145 (2009).

Acknowledgement

The three years of doctoral course study at Hiroshima University is an unforgettable wonderful time in my life. I would like to give special appreciation to my supervisor Prof. Kenya Shimada who provided a valuable opportunity of studying in such a great environment that I can concentrate to progress this project. Three years ago, it was the first time I came to Japan. When I stepped into the Hiroshima synchrotron radiation center, I felt infinite nervous and uneasy. But after getting along with my supervisor Prof. Shimada, I started to calm down, because I my supervisor Prof. Shimada is so approachable and amiable. More importantly, my supervisor Prof. Shimada is so rigorous in academic research, which has given me a very important influence. In my study and research, Prof. Kenya Shimada always patiently explains to me in detail to ensure that I can understand; in my daily life, my supervisor Prof. Shimada also gave me a lot of care and support, which make me feel endless warmth. The rigorous academic research style and profound professional knowledge of my supervisor Prof. Shimada is a role model for me to learn forever.

I would like to express my sincere grateful for the kind, patient, and intellectual guidance from Prof. Taichi Okuda, Prof. Koji Miyamoto, Prof. Shiv Kumar, Prof. Eike F. Schwier, Prof. Masashi Arita, Prof. Munisa, Prof. Akio Kimura, Prof. Hirofumi Namatame for the kind support and professional advice during my Ph.D. study at Hiroshima University. Discussions with they often prompted me to have a deeper understanding of the experimental data.

Also, I would like to thank Dr. Shilong Wu, Dr. Mingtian Zheng, Dr. Xiaoxiao Wang, Mr. Wumiti Mansuer, who give me a lot of encouragement and share the experience and something interesting in their life. I am grateful to Mr. Yamamoto, Miss Namatame, Mr. Miyai, Ms. Hou, Mr Amit, Mr. ishiba with whom I have had the pleasure to work and study together. Besides, I am also very grateful for all the kind support and help from Ms. Shinno and Ms. Shimokubo in Hiroshima Synchrotron Radiation Center and the staffs in student support office and department of physical science office.

Special thanks to our collaborators Prof. Chaoyu Chen, Prof. Qihang Liu, Prof. Chang Liu, Mr. Shixuan Zhao, Dr. Xiaoming Ma, Mr. Zhanyang Hao, Ms. Yujie Hao in the Southern University of Science and Technology, for providing the high-quality single crystal samples and extensive professional theoretical calculations.

I would like to thanks to the generous economic supports from Graduate School of Science, Graduate School of Advanced Science and Engineering in Hiroshima university and Japan Student Services Organization (JASSO).

Nobody has been more important to me in the pursuit of my Ph.D. degree than my family. I wish to thank my beloved parents and my wife for their tremendous spiritual and financial supports.

10 May 2021

Ke Zhang